INFORMATION TO USERS

This manuscript has been reproduced from the microfilm master. UMI films the text directly from the original or copy submitted. Thus, some thesis and dissertation copies are in typewriter face, while others may be from any type of computer printer.

The quality of this reproduction is dependent upon the quality of the copy submitted. Broken or indistinct print, colored or poor quality illustrations and photographs, print bleedthrough, substandard margins, and improper alignment can adversely affect reproduction.

In the unlikely event that the author did not send UMI a complete manuscript and there are missing pages, these will be noted. Also, if unauthorized copyright material had to be removed, a note will indicate the deletion.

Oversize materials (e.g., maps, drawings, charts) are reproduced by sectioning the original, beginning at the upper left-hand corner and continuing from left to right in equal sections with small overlaps. Each original is also photographed in one exposure and is included in reduced form at the back of the book.

Photographs included in the original manuscript have been reproduced xerographically in this copy. Higher quality 6" x 9" black and white photographic prints are available for any photographs or illustrations appearing in this copy for an additional charge. Contact UMI directly to order.

UMI

A Bell & Howell Information Company
300 North Zeeb Road, Ann Arbor MI 48106-1346 USA
313/761-4700 800/521-0600

Measurement of The Parity Nonconserving Spin-Rotation of Transmitted Cold Neutrons Through a Liquid Helium Target

by

Diane M. Markoff

A dissertation submitted in partial fulfillment
of the requirements for the degree of

Doctor of Philosophy

University of Washington

1998

Approved by 

(Chairperson of Supervisory Committee)

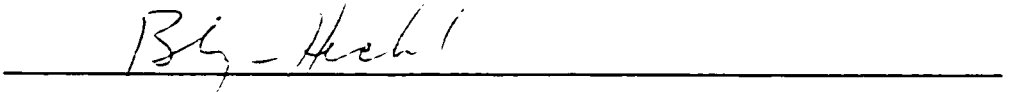

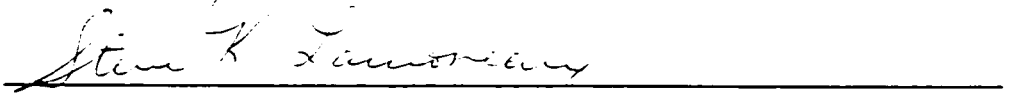

Program Authorized
to Offer Degree Physics

Date 15 December 1997

In presenting this dissertation in partial fulfillment of the requirements for the Doctoral degree at the University of Washington, I agree that the Library shall make its copies freely available for inspection. I further agree that extensive copying of this dissertation is allowable only for scholarly purposes, consistent with "fair use" as prescribed in the U.S. Copyright Law. Requests for copying or reproduction of this dissertation may be referred to University Microfilms, 1490 Eisenhower Place, P.O. Box 975, Ann Arbor, MI 48106, to whom the author has granted "the right to reproduce and sell (a) copies of the manuscript in microfilm and/or (b) printed copies of the manuscript made from microform."

Signature Duane Markoff

Date 19 March 1998

University of Washington

Abstract

Measurement of The Parity Nonconserving Spin-Rotation of Transmitted Cold Neutrons Through a Liquid Helium Target

by Diane M. Markoff

Chairperson of Supervisory Committee: Professor Eric G. Adelberger

Department of Physics

We completed the first measurement of the parity non-conserving neutron spin-rotation in helium, φ_{PNC}. The PNC spin-rotation is sensitive to the isovector pion exchange amplitude, f_π, in the meson exchange model that describes the weak NN interaction. The strength of the pion coupling is of particular interest because it probes the neutral current contribution to the weak NN interaction, and it is not well known.

We measured the PNC spin-rotation of cold neutrons transmitted through a liquid helium target located between a crossed polarizer and analyzer. We obtained the value $\dot{\varphi}_{\mathsf{PNC}} = (3.7 \pm 6.6(stat) \pm 1.0(syst)) \times 10^{-7}$ radians in a 46 cm target. We combined our results for $\varphi_{\mathsf{PNC}}(\vec{n} + \alpha)$ with the longitudinal analyzing power measured in the isospin mirror system, $A_L(\vec{p}+\alpha)$ [LMM+86] to obtain a value for f_π that is insensitive to the contribution from the isoscalar couplings. We obtain a range, $-34 < f_\pi < 23$ in units of the sum rule value, 3.8×10^{-8}, which is consistent with the predicted range of $0 < f_\pi < 30$ and with previous experimental values. Although our results are limited by statistics, this is currently the most sensitive measurement of any PNC neutron spin-rotation.

TABLE OF CONTENTS

LIST OF FIGURES

LIST OF TABLES

ACKNOWLEDGMENTS

I would like to acknowledge the financial support from the Department of Energy through the University of Washington Nuclear Physics Lab grant, the National Science Foundation grant supporting the Neutron Spin-rotation and Electric Dipole Moment projects, and the Department of Commerce through the NIST Neutron Interactions and Dosimetry Group and the Reactor Research and Development group at the Cold Neutron Research Facility in Gaithersburg, Maryland.

I would like to thank my co-advisor Blayne Heckel for introducing me to the cold neutron field, for his time and contributions to this project, and for passing to me many of his tricks and rules of thumb. I acknowledge the insightful design reviews and contributions from my advisor Eric Adelberger, and thank him for his time to carefully review this document. I thank my committee member, Steve Lamoreaux for his advise and ideas received in the early years of the project and for his willingness to continue his associations from a distance. Thanks to Erik Swanson for his many hours developing the data acquisition programs.

As I look back on this thesis project, I am overwhelmed with the generous contributions of many people who made this experiment the success that it became. The list is quite long of technicians, coworkers and friends who came to my support with help, advise and encouragement, giving their extra time and energy sometimes under critical conditions providing the needed part, extra pair of hands, or necessary administrative paperwork.

"Thanks" is small compensation and even with the qualifier, "very", does not begin to express my appreciation to Steve Penn, who spent three long and hard years as

a postdoc on this project. Together we invested many long hours nursing the cryostat, fixing the vacuum leaks and keeping the system going. With his encouragement and patience, we did not give-up and we won: extracting good data from a very delicate apparatus.

Thanks to the Neutron Interactions and Dosimetry group at NIST. Their support with technical assistance, time, spare parts, social diversions (touch football, excursions to DC), espresso, pizza, and more, all went beyond the friendly professional courtesy afforded visiting scientists.

Nearly all of the technical support staff at the NPL contributed in one way or another to the success of this project. Hank Simons and Jim Elms crafted with skill many parts of the target system. Luis Geissel and Steve Zsitvay, constructed a number of small parts for us, often with short notice. All four of these talented men taught me drafting and machining tricks, and offered good suggestions on construction and materials. The Physics shop contributed with the construction of the magnetic shields and the coil cores. We received cryogenic assistance from Derek Storm and Doug Will. Thanks to Doug for his willingness to provide at nearly any time of the day or night, the needed liquid helium (and chocolate) for our NPL tests. John Wootress and Dean Corcoran provided extra pairs of hands when needed and any material, creative vacuum parts, or chemicals that we could request. Tim VanWechel and Allen Meyers in the NPL electronics shop built control boxes for us, and provided parts and assistance with what we put together ourselves. Dick Seymour was always willing to pull me out of the latest computer mess I was in.

The administrative staff meant more to me than merely the people who kept the NPL running. Maria Ramirez, Karin Hendrickson and Barbara Fulton rescued me a number of times, took care of a number of paperwork details while we were at NIST for 6 months, and went out of their way to assist and support me through the years.

Grad school is not an experience one does alone. A number of my friends and classmates lived this project with me. I thank my especially supportive buddy Mark Wilber for being there: we studied for qualifying exams together, we wrote our thesis together, and in-between we kayaked rivers and consumed a lot of chocolate together. I thank my friend and roommate Elizabeth Grygo for sticking by me whether 2 feet or thousands of miles away, helping me through the difficult times and laughing with me in the good times. Thanks to Alison Eisinger for taking care of me, even when I resisted. I thank my classmate Dawn Meekhof for years of lunches and outdoor adventures together and for introducing me to the wonders of whitewater kayaking. I enjoyed many long conversations with fellow physicist Kristi Hendricksen, and I thank her for listening to me through my last years of the project. I have gratefully received the support and friendship of classmate Adam Martin. There were many fellow NPL grad students and postdocs that I shared good laughs with, for which gatherings, lunches, physics chats, and 'going for coffee' all made the path more enjoyable. Thanks to all my friends for sharing with me the wonders, beauty, and adventures in the back-country and on the rivers of the Pacific Northwest.

I gratefully acknowledge the support both emotionally and financially of my parents. They have encouraged me from the early years to excel in math and science and to pursue the education and challenges I sought. My Mother began her long battle with a brain tumor during my first year in graduate school. I regret that she did not live to see this project reach its completion, though of all people, she believed and she knew this document would someday exist. It is to her that I dedicate this work.

Dedicated in loving memory to my mother,
Irene Markoff (1929 - 1995)

...we will do, and (then) we will understand.
(Ex 24:7)

... נעשה ונשמע.
(שמות כד: ז)

Chapter 1

OVERVIEW

Conservation laws and symmetries have been studied by physicists in the quest for the most simple description of the four forces in nature: gravity, electromagnetism, weak and strong nuclear forces. Some of these conservation principles are derived from the belief that interactions should be independent of certain physical descriptors of a system, for example the position in space, the orientation relative to an arbitrary coordinate system, and the initial time of the interaction. Other symmetries are formulated from experimental observation, such as the conservation of baryon number (baryons are strongly interacting heavy particles of half-integer spin) and of lepton number (leptons are light "point particles" unaffected by the strong interaction). These conservation principles allow us to develop mathematical models and descriptions of the fundamental interactions without necessarily understanding the underlying details of the processes.

Symmetries arise mathematically through Noether's theorem, which states that a conserved quantity exists for each invariance of the hamiltonian. [Gol80] For example, momentum conservation arises from the invariance of the hamiltonian under linear translations, and energy conservation arises from the invariance under time translations. For an invariance of the hamiltonian under the discrete transformation of spatial inversion, the corresponding conserved quantity is called parity.

A parity transformation reflects the coordinates of a system through the origin, so that $\mathrm{P}(\hat{r}) \mapsto (-\hat{r})$. In Figure 1.1, the coordinates of a spinning particle are

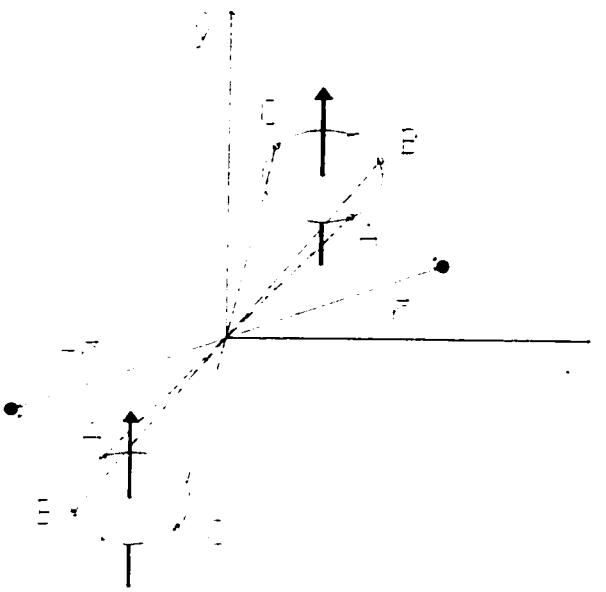

Figure 1.1: Pictorial representation of parity reflection for the decay of a polarized nucleus. The emitted particle is shown with position vector $\vec{r}$. Note that the spin of the nucleus is unchanged in the transformation.

spatially reflected, and while the coordinate vector changes sign under the parity transformation, the spin vector does not. We say that a system is invariant under parity if interaction cross sections and rates involving the reflected system are identical to those involving the original system.

Although previous experimental evidence in nuclear systems upheld the concept of parity conservation, in 1956, Lee and Yang, [LY56] presented a theoretical argument that parity violation was possible in nuclear β-decay and other processes governed by the weak interaction. Figure 1.1 shows a polarized nucleus emitting a particle. If this weak decay conserves parity, then the process does not distinguish between the two configurations and the number of particles emitted in the direction of the nuclear spin should be the same as the number emitted opposite to the nuclear spin.

Wu *et al.* measured a non-zero asymmetry of electrons emitted in the β-decay of polarized ^{60}Co nuclei.[WAH$^+$57] For a fixed β-particle detector, flipping the nuclear

polarization direction and comparing the rates is equivalent to the test depicted in Figure 1.1. This measurement was the first definitive evidence that the weak interaction could discern between two mirror reflected states of a system. The weak interaction is the only force known to exhibit parity violation.

Since the monumental work by Lee, Yang and Wu *et al.*, experiments have shown that the weak interaction also violates flavor conservation, another discrete symmetry. Flavor is the quantum number that identifies the 6 types of quarks: *u, d, c, s, b, t* for up, down, charm, strange, bottom, and top. The strong and electromagnetic interactions conserve the total number of quarks of each flavor, while weak decays can violate flavor conservation, for example by changing the amount of charm or strangeness of the reaction products compared to the initial system.

The weak interaction is well understood in leptonic systems that involve only point particles, for example, the electron, the muon, and the neutrinos. For these systems, only the electromagnetic and weak interactions are involved. However, for systems that include hadrons, composite particles constructed from quarks, weak interaction processes are very difficult to compute because of the complicating presence of the strong interaction.

Since the strength of the weak interaction is approximately a factor of 10^7 smaller than the strong nuclear force, we must use the symmetry violating properties of the weak interaction to isolate and study the weak force between hadrons. In high-energy physics experiments, the weak interaction in hadronic systems is studied by observing flavor-violating weak decays. In low-energy experiments where flavor is conserved, we measure parity-violating observables in strongly interacting systems to study the hadronic weak interaction.

One example of a parity-nonconserving observable in a hadronic system is the rotation of the transverse spin polarization vector of very low energy neutrons (on the order of 10^{-3} eV) as they travel through a spin-zero material. This small, parity-violating rotation (on the order of 10^{-5} radians), was first observed in heavy isotopes

of tin (Sn) and lanthanum (La). [HRG+82],[HFS+84] Nuclear structure calculations in heavy elements can be difficult and inhibit the ability to extract direct nucleon-nucleon weak interaction information from these systems. Therefore, there is great interest in applying this proven technique to light nuclear systems, where the nuclear structure is more tractable theoretically. Unfortunately, this theoretical simplicity is accomplished by an experimental disadvantage, namely the neutron spin-rotation signal is smaller than that in the heavier systems.

This thesis describes the first measurement of the parity-violating neutron spin-rotation observable in the $n + \alpha$ system. We describe the theoretical motivation for the measurement and present the relationship between the spin-rotation observable and the low energy nucleon-nucleon weak interaction model. We describe the apparatus and the data acquisition methodology. We quote a result for the spin-rotation measurement with a discussion of the systematic and statistical errors, and the implications for the hadronic weak interaction.

Chapter 2

WEAK INTERACTION IN NUCLEON-NUCLEON SYSTEMS

The flavor conserving hadronic weak interaction is accessible only through the nucleon-nucleon interaction. Here, the precise quark structure of the weak interaction becomes important [HH95] and complicates our understanding of the interaction. The experiments in this sector are difficult, sometimes not achieving the sensitivity necessary to extract information on the weak interaction. In complex nuclear systems where signals are often enhanced, uncertainties in the nuclear structure calculations limit the accuracy of the results.

By studying the low-energy, flavor-conserving, nucleon-nucleon processes, we can probe the neutral-current contribution to the weak interaction between quarks. Flavor violating (strangeness or charm changing) hadronic interactions proceed only through the charged weak current. In the Glashow-Iliopoulos-Maiani (GIM) model, the neutral-current part of the hadronic weak interaction does not contain strangeness changing cross terms of the type $d \leftrightarrow s$ (ΔS=1) and charm changing cross terms $u \leftrightarrow c$ (ΔC=1) [CB83]. (Refer to Equation 2.3 below.)

The subject of parity-violation (PV) in the nucleon-nucleon system has been discussed in two comprehensive review papers. The first, written by Adelberger and Haxton covers the topic until 1985 [AH85]. Recent progress is presented in a book chapter by Haeberli and Holstein [HH95]. The following discussion is based in part on their work.

2.1 *Weak current-current lagrangian*

For the low energy regime, the current-current weak interaction lagrangian on the quark level, can be written as

$$\mathcal{H}_{\mathrm{wk}} = \frac{G}{\sqrt{2}}(J_{\mathrm{W}}^{\dagger} J_{\mathrm{W}} + J_{\mathrm{Z}}^{\dagger} J_{\mathrm{Z}}) \tag{2.1}$$

where the Fermi constant $G \approx 10^{-5}\mathrm{M}_N^{-2}$. The charged current, J_{W}, mediated by the W boson and the neutral current, J_{Z}, mediated by the Z boson are given for the light quarks, u, d, and s by

$$J_{\mathrm{W}} = \bar{u}\gamma_{\mu}(1+\gamma_5)[\cos\theta_c d + \sin\theta_c s] \tag{2.2}$$

$$J_{\mathrm{Z}} = \bar{u}\gamma_{\mu}(1+\gamma_5)u - \bar{d}\gamma_{\mu}(1+\gamma_5)d - \bar{s}\gamma_{\mu}(1+\gamma_5)s - 4\sin^2\theta_w J_{\mu}^{\mathsf{EM}} \tag{2.3}$$

where γ_{μ} and γ_5 are the Dirac matrices, θ_c and θ_w are the Cabibbo and Weinberg angles respectively and J_{μ}^{EM} is the electromagnetic current. As seen in Equation 2.2, the charged current is a combination of ΔI=1, ΔS=0, and ΔI=$\frac{1}{2}$, ΔS=-1 terms, where "S" denotes the strangeness quantum number and "I" denotes strong isospin. The neutral current transforms as ΔS=0, and contains ΔI=0 and ΔI=1 contributions. We can write the charged and neutral currents in terms of their strong isospin dependence.

$$J_{\mathrm{W}} = \cos\theta_c J_{\mathrm{W}}^{1} + \sin\theta_c J_{\mathrm{W}}^{\frac{1}{2}} \tag{2.4}$$

$$J_{\mathrm{Z}} = J_{\mathrm{Z}}^{0} + J_{\mathrm{Z}}^{1} \tag{2.5}$$

where the superscripts denote the isospin transition, $|\Delta\mathrm{I}|$.

To obtain the weak hamiltonian, we form the product of the J_{W} and J_{Z} currents with their respective complex conjugates. The isospin dependence of the current-current terms contributing to the parity-violating weak Hamiltonian can be summarized as follows: [CB83]

$$(J_{\mathrm{W}}^{\frac{1}{2}})^{\dagger} J_{\mathrm{W}}^{\frac{1}{2}} + J_{\mathrm{W}}^{\frac{1}{2}} (J_{\mathrm{W}}^{\frac{1}{2}})^{\dagger} \qquad |\Delta\mathrm{I}| = 1 \tag{2.6}$$

$$(J^1_W)^\dagger J^1_W + J^1_W (J^1_W)^\dagger \qquad |\Delta I| = 0, 2 \qquad (2.7)$$

$$(J^0_Z + J^1_Z)^\dagger (J^0_Z + J^1_Z) + (J^0_Z + J^1_Z)(J^0_Z + J^1_Z)^\dagger \qquad |\Delta I| = 0, 1, 2 \qquad (2.8)$$

This hamiltonian can be described as a sum of effective hamiltonians for the parity-violating weak transition with isospin changes of 0, 1 or 2. The ΔI=2 effective hamiltonian has contributions from the product of two isovector (I=1) charged currents and from two isovector neutral currents. Similarly, the ΔI=0 effective hamiltonian has contributions from both the charged and neutral current. The ΔI=1 effective hamiltonian has contributions from the product of two I=$\frac{1}{2}$ charged currents as well as from the product of the isoscalar (I=0) and isovector terms of the neutral current. Since the I=$\frac{1}{2}$ charged current product is proportional to $\sin^2\theta_c \sim \frac{1}{25}$, the contribution to the ΔI=1 hamiltonian should be dominated by the neutral current.

2.2 Parity-violating nucleon-nucleon weak interaction potential

The direct exchange of the short-ranged, weak vector bosons (W,Z) between low energy nucleons is suppressed by the repulsive core of the strong interaction. An improved representation of the nucleon-nucleon (NN) weak interaction uses the meson exchange model which successfully describes the low energy strong interaction between nucleons. The parity-conserving strong N-N interaction is described by the sum of meson exchange diagrams in which the $\pi, \eta, \rho, \omega, \sigma, ...$ mesons couple strongly to the $\bar{\text{N}}$N vertices. Similarly, the weak N-N interaction can be modeled as an exchange of light mesons (π, ρ, ω) where the diagram has one weak interaction vertex and one strong vertex, as shown in Figure 2.1 [Hol89].

As a result of the repulsive, strong NN interaction, the light mesons of mass less than about 800 MeV dominate the exchange terms. The meson exchanges that contribute to the parity violating NN interaction include the spin zero (J=0), isospin one (I=1), $\pi^\pm$-meson, the J=1, I=1 ρ-meson, and the J=1, I=0 ω-meson. According to Barton's Theorem [Bar61], the exchange of a neutral spinless boson between on-

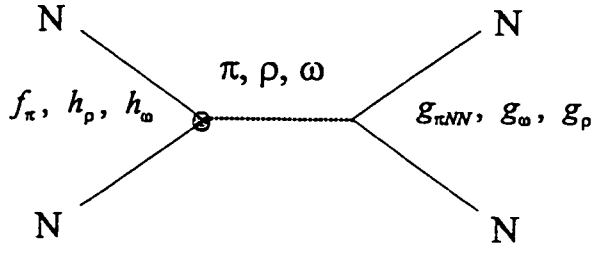

Figure 2.1: Weak interaction meson exchange diagram. The strong vertex is described by the well known strong coupling constants, $g_{\pi NN}$, g_ω, g_ρ. The weak vertex is characterized by the lesser known weak couplings, f_π, h_ρ, h_ω, described in Table 2.1.

shell nucleons is forbidden by CP invariance (C is the charge conjugation operator and P is the parity operator). With the assumption that CP conservation holds, π^0 exchange is omitted.

Multiple exchange from mesons heavier than the pion is negligible. The $\ell = 1$ component of 2π exchange is dominated by the single ρ exchange. The $\ell = 0$ part is dominated by σ exchange which does not participate in the parity-violating NN interaction by Barton's Theorem and CP conservation.

The weak interaction physics is contained in the weak vertex, and is expressed in the values of the parity-violating nucleon-nucleon-meson (NNM) coupling constants. The weak NNM matrix elements, $<$M N$|\mathcal{H}_{wk}|$N$>$, for both the charged and neutral current contributions were calculated by Desplanques, Donoghue, and Holstein (DDH) in 1980 [DDH80].

It is important to note that π-meson exchange is purely isovector and the contribution from the charged current is proportional to $\sin^2(\theta_c)$, so is strongly suppressed. Therefore, the neutral-current contribution dominates the π-meson amplitude, and its coupling strength should be a direct measure of the neutral current contribution to the NN weak interaction.

Table 2.1: Exchange mesons in the NN system [AH85]

Isospin	N-N System			Meson	Coupling
ΔI	nn	np	pp	Exchanged	Coefficient
0	X	X	X	ρ, ω	h_ρ^0, h_ω^0
1	X		X	ρ, ω	h_ρ^1, h_ω^1
1		X		$\pi^\pm$, ρ, ω	f_π, h_ρ^1, h_ω^1
2	X	X	X	ρ	h_ρ^2

Thus, the leading mesons exchanged are the $\pi^\pm$ with ΔI=1 transitions only, the ρ with ΔI=0,1,2 transitions, and the ω with ΔI=0,1 transitions. Table 2.1 lists the 6 non-negligible meson exchange coefficients and their associated transition properties.

A number of uncertainties are associated with the DDH calculations, including those arising from uncertainties in the current-masses of the u and d quarks, the use of a relativistic vs. nonrelativistic quark model, and the effects of SU(6) symmetry breaking on sum-rule contributions and emission amplitudes. These uncertainties led DDH to present the NNM coupling predictions as a range of "acceptable values". A "best value" is also presented, which represents the theorists' best "educated guess" of the true values. These results are presented in Table 2.2.

Since the DDH analysis, two other calculations have been reported and those results are also presented in the table [DZ86], [FCDH91]. These more recent calculations indicate a value for the pion exchange coefficient, f_π, that is smaller than the DDH best value.

Table 2.2: Predicted PNC meson exchange coupling constants. Strengths are in units of the sum-rule value 3.8×10^{-8}.

Coupling	DDH Reasonable Range	DDH Best Value	DZ	FCDH
f_π	0 → 30	12	3	7
h_ρ^0	30 → -81	-30	-22	-10
h_ρ^1	-1 → 0	-0.5	+1	-1
h_ρ^2	-20 → -29	-25	-18	-18
h_ω^0	15 → -27	-5	-10	-13
h_ω^1	-5 → -2	-3	-6	-6

2.3 Experimental studies of the meson exchange coefficients

In the low energy nucleon-nucleon (NN) system, the parity nonconserving (PNC) observables are expected to be rather small, as indicated by the ratio of the weak to strong coupling parameters: $4\pi G_F m_\pi^2 / g_{\pi NN}^2 \approx 10^{-7}$. This points out the difficulty of carrying out measurements with enough sensitivity to extract information on the weak meson exchange amplitudes.

2.3.1 Parity-violating observables

The majority of the weak NN experiments involve the detection of pseudoscalar observables which are odd under spatial inversion. Observables related to $\vec{\sigma} \cdot \vec{p}$ are parity-violating, because momentum changes sign upon spatial inversion and spin does not. One example is the circular polarization of gamma-rays, $P_\gamma = <\vec{\sigma}_\gamma \cdot \hat{p}_\gamma>$, emitted by an unpolarized, parity-mixed nuclear state. Circular polarization experiments are restricted by the low efficiency, typically 4%, of circular polarization analyzers. A related parity-violating observable is A_γ, the asymmetry of photons emitted with re-

spect to the polarization direction of the parent nuclei, for example from deuterium polarized in the reaction, $\vec{n} + p$. This observable is related to $<\vec{J} \cdot \vec{p}_\gamma>$, where $\vec{J}$ is the nuclear polarization.

Another common parity-violating observable is the longitudinal analyzing power, A_L, of reactions initiated by nucleons polarized parallel and anti-parallel to the beam momentum axis. This analyzing power is proportional to the asymmetry of cross sections for the incident nucleon in the $+1$ and -1 helicity states and is thus dependent upon $<\vec{\sigma} \cdot \vec{p}>$ where σ and p refer to the incident nucleon. Experiments measuring this observable require the difficult task of quickly and completely reversing the beam helicity. This requirement is the limiting systematic uncertainty in these measurements.

The parity-violating rotation of the spin of a transversely polarized slow neutron as it propagates through a medium will be discussed in detail in Chapter 3, and the motivation to pursue these experiments is discussed in Section 2.4.

In nuclear systems with A>5, parity-mixed doublet states are studied by detecting pseudoscalar observables, for example, A_L in ^{14}N, P_γ in ^{18}F, and A_γ in ^{19}F. The resulting signal from the parity mixing of two well-known states of identical spins, small energy separation, and opposite parity is enhanced by the small denominator proportional to the difference in energies. Further enhancement occurs for doublets with very different decay amplitudes. These enhancements can lead to signals on the order of 10^{-4} or 10^{-5}, a distinct experimental advantage.

PNC observables in heavy nuclear systems are often enhanced allowing for more accurate measurements of larger signals. For example, low energy neutron scattering on compound nuclear states (specifically p-wave resonances in the isotopes of thorium and uranium) see enhancements on the order of 10^6 producing parity-violating cross section asymmetries on the order of 1% [BGJM93]. However, in these large systems, the nuclear structure is not sufficiently understood to extract specific information on the underlying PNC nucleon-nucleon weak interaction. Two experiments that

measured parity-violating observables in heavy nuclei have historical significance. The first reliable detection of parity-violation in the NN system was from a γ-ray circular polarization measurement in ^{181}Ta [L$^+$67]. The first neutron spin-rotation measurements were performed in the isotopes of tin [FHR$^+$80],[Hec81] and later in lead [HRG$^+$82] and lanthanum [HFS$^+$84].

The parity-violating NN interaction has also been studied by measuring the rates of parity-violating processes. Measurements of parity-forbidden alpha decays have been done in ^{16}O and ^{20}Ne. However, uncertainties associated with the contribution of more than one interfering state of the same spin and opposite parity, complicate the interpretation of the results.

In addition to nuclear processes, measurements of atomic PNC observables probe the hadronic weak interaction. The anapole moment observable arises from the electron-nucleus interaction in which the exchange photon is absorbed by parity-violating components of the nuclear wave function. Substantial improvements to atomic PNC measurements in cesium have recently lead to the first definitive measurement of the anapole moment [WBC$^+$97].

2.3.2 Review of previous measurements

In Table 2.3, we present experimental work related to the extraction of the meson coupling constants. The table is divided into sections in which the experiments are presented according to their sensitivity to the dominant isovector and isoscalar coupling constants, f_π and h^0_ρ. The reaction or nucleus studied is given along with the DDH prediction for the measured PV observable.

As indicated in Table 2.1, ΔI=0 transitions in all NN systems are only sensitive to the isoscalar coupling constants. In addition, ΔI=1 interactions in the p-p and n-n systems are independent of the pion exchange term. Experiments in these systems, insensitive to f_π, are listed in the first section of Table 2.3.

Table 2.3: Experiments that measure the NN weak interaction. The nuclear states are described as $(J^\pi;T)$, where T is the nuclear level isospin. Values are taken from reference [HH95], except the ^{133}Cs numbers from [FM97].

Coupling Dependence	NN System	PV Observable	$\times 10^{-7}$ DDH Prediction	$\times 10^{-7}$ Experiment
h_ρ^0	p-p	$A_L(\vec{p}+p)$[45MeV]	-1.44	-1.57 ± 0.23
		$A_L(\vec{p}+p)$[221MeV]	~ 1	$1.1 \pm 0.4 \pm 0.4$
	^{14}N	$A_L(^{13}C(p,p)^{13}C)$ Mixing $(0^-;1);(0^+;1)$	-280	$+90 \pm 60$
	n-p	$P_\gamma(\vec{n}(p,d)\gamma)$	0.57	1.8 ± 1.8
$h_\rho^0+f_\pi$	p-α ^{19}F	$A_L(\vec{p}+\alpha)$	-3.33	3.3 ± 0.9
		A_γ(decay)	-890	-740 ± 190
		$(\frac{1}{2}^-;\frac{1}{2}) \rightarrow (\frac{1}{2}^+;\frac{1}{2})$		
	n-d	$A_\gamma(\vec{n}+d)$	9.68	42 ± 39
	^{21}Ne	P_γ(decay)	6600	8000 ± 14000
		Mixing $(\frac{1}{2}^+;\frac{1}{2}),(\frac{1}{2}^-;\frac{1}{2})$	0.27	0.364 ± 0.062
	^{133}Cs	Anapole Moment, κ_a from $E1_{PNC}$ (6S$\leftrightarrow$7S)	0.27	0.364 ± 0.062
f_π	n-p	$A_\gamma(\vec{n}(p,d)\gamma)$	-0.49	-0.15 ± 0.47
	^{18}F	P_γ(decay) Mixing $(0^-;0);(0^+;1)$	20,800	1200 ± 3860

In the p-p system, the isoscalar (and isotensor) longitudinal analyzing power ($A_{\rm L}$) of polarized protons on a proton target has been measured. The simplicity of the $(\vec{p}+p)$ system provides a theoretical advantage, though great effort was required by a number of groups to reduce systematic uncertainties in the experimental measurements. The final result (published in 1987) of $A_{\rm L}(45{\rm MeV}) = -(1.57 \pm 0.23) \times 10^{-7}$ represents one of the most accurate measurements of parity-violation in hadronic interactions and is consistent with the DDH theoretical prediction [KLL+87]. An experiment is currently underway at TRIUMF, Canada, to measure this longitudinal analyzing power at 221 MeV to an error of $\pm 2 \times 10^{-8}$. Preliminary results indicate a value of $A_{\rm L}(221{\rm MeV}) = (1.1 \pm 0.4(syst) \pm 0.4(stat)) \times 10^{-7}$ [Pag97] Note that the change in sign is consistent with the measurement at higher energies.

The theoretical calculations and the measurement of the analyzing power of emitted protons from parity mixed doublet states in ^{14}N currently disagree in sign. The large shell model basis required to include levels up to $2\hbar\omega$ renders the calculations difficult in this system. The measurement of the circular polarization of the emitted γ-ray in the scattering of neutrons on protons is consistent with DDH best value predictions and with zero. The accuracy required to constrain the isoscalar (h_ρ^0) and isotensor (h_ρ^2) couplings is approximately an order of magnitude smaller than the current limit set in 1984.

Experiments in systems that are sensitive to both the isoscalar and isovector couplings are presented in the next section of Table 2.3. The gamma-ray asymmetry (A_γ) has been measured in the decay of ^{19}F from the spin $\frac{1}{2}$ first excited state to the ground state. Calculations in this system rely on the ability to calibrate the contributions to the weak matrix elements using β-decay measurements in ^{19}Ne and shell model calculations. The theoretical prediction based on DDH best values is in agreement with the experimental results. Predictions based on smaller values of f_π and h_ρ^0 indicated by newer calculations (Table 2.2), lie outside the experimental range.

The longitudinal asymmetry (A_L) of polarized protons scattered from alpha particles $\vec{p}+\alpha$, is sensitive to the isoscalar and isovector contributions to the hadronic weak interaction. The systematic uncertainties in the $\vec{p}+\alpha$ system (similar to those which limit the $\vec{p}+p$ measurements) were reduced in improved experiments. The result, $A_L = (-3.3 \pm 0.9) \times 10^{-7}$, like in ^{19}F, agrees well with DDH theoretical predictions, though is out of the range for predictions based on the newer calculations [LMM+86].

The gamma-ray asymmetry (A_γ) from the capture of polarized neutrons on deuterium ($\vec{n}+d \rightarrow t+\gamma$) was measured. Although the PNC effect in $\vec{n}+d$ is larger than in the $\vec{n}+p$ capture process, this experiment is limited by statistical uncertainties.

Interpretation of the results from the parity mixed doublet decay in ^{21}Ne is very sensitive to theoretical uncertainties as a result of the large, opposing contributions of f_π and h^0_ρ. In addition, a β-decay calibration of the matrix elements is not possible, and substantial changes to the results can be made with reasonable changes in the nuclear structure calculations. Initial calculations indicated an inconsistent set of coupling values when compared to other experimental results. Newer calculations suggest a more consistent set of values for f_π and h^0_ρ [HB95].

The ^{133}Cs anapole moment depends on both the isovector pion exchange term and the isoscalar terms. Wood *et al.* determined the nuclear spin-dependent contribution (the effect of the anapole moment) to the amplitude of the parity-violating transition between the 6S and 7S states of cesium. Theoretical calculations using this result indicate a pion coupling constant in the upper range of the acceptable values, in contrast to other experimental results [Hax97], [FM97].

From Table 2.1, we see that ΔI=1 transitions in the n-p system are dominated by the isovector coupling constant f_π. Experiments in these systems sensitive to only the isovector couplings are presented in the third section of Table 2.3. The measurement of A_γ in the $\vec{n}+p$ system with its large statistical errors is consistent with zero as well as with the DDH best guess predictions for f_π.

In the ^{18}F system, the P_γ signal from the decay of the J=0$^-$ (isospin 0) state receives a large enhancement factor from parity mixing with the nearby J=0$^+$ (isospin 1) state. This enhancement arises from the large ratio of the decay times of an isospin forbidden transition and an isospin allowed decay. Although a large nucleon system, the theoretical calculations stand on firm ground resulting from the experimental calibration of the weak matrix elements with ^{18}Ne *beta*-decay amplitudes. Measurements in ^{18}F done by several different collaborations are all self-consistent (mean value $P_\gamma = (12 \pm 38) \times 10^{-5}$) and currently constrains the pion coupling constant, f_π, to a value that is considerably smaller than the theoretical best value, though it is within the reasonable range.

2.4 Constraints on weak meson couplings, f_π and h^0_ρ

At the present level of experimental accuracy, the isotensor coupling contribution is significant in only the *p-p* system, and even there it is small compared to the isoscalar contribution. Thus, it is reasonable to present the results with only the dominant isovector contribution from the f_π coupling constant and an effective isoscalar coupling constant, $(h^0_\rho + 0.6h^0_\omega)$. A summary of results from the previously discussed experiments is given in Figure 2.2. The reasonable range values are indicated, and the result of a least squares fit to the data (excluding the ^{133}Cs and revised ^{21}Ne data) for both the isoscalar and isovector couplings is shown.

Theoretical uncertainties in extracting the MNN couplings from systems more complicated than the bare nucleon-nucleon system may be significant, but are not included in the error bands presented. For example, in the study of parity doublet decays in ^{21}Ne for which a β-decay calibration of the matrix elements is not possible, substantial changes to the results can be made with reasonable changes in the nuclear structure calculations [HH95]. A revised analysis for ^{21}Ne is presented, again showing only the experimental errors.[HB95].

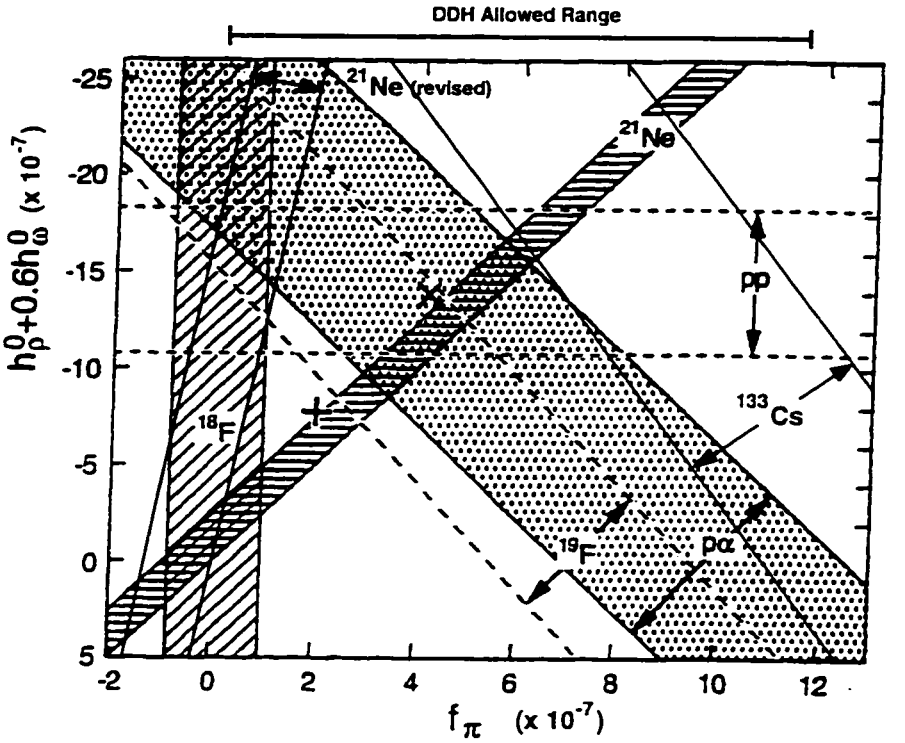

Figure 2.2: Experimental constraints on the isoscalar and isovector coupling constants. The DDH allowed range for f_π is indicated, while the allowed range for h_ρ^0 includes the entire range shown. The "+" sign indicates the best fit to the data (excluding the revised ^{21}Ne data and the new ^{133}Cs data) and the "X" marks the DDH theoretical best values. Adapted from [HH95].

Presented in Figure 2.2, is the range of the couplings derived from the recent analysis by Flambaum and Murray of the cesium anapole moment measurement. Their calculations are consistent with the ^{18}F results for large, negative values for the isoscalar couplings. The error band includes only the experimental error. Using DDH best values for all of the other couplings, they obtained $f_\pi = (9.5 \pm 2.1(\text{exp}) \pm 3.5(\text{theo})) \times 10^{-7}$. With the inclusion of the theoretical error, this result becomes consistent with the DDH prediction.[FM97]

As seen in Figure 2.2, there is currently no consistent set of coupling values that fits the experimental data. The ^{18}F measurement provides the most reliable constraint on f_π, restricting it to the small range of $|f_\pi| \leq 1.3 \times 10^{-7}$. Both the DDH "best value" and the "best fit" are outside of this range. In addition, theoretical calculations of the couplings based on different models and assumptions do not agree.

There is no clear determination of the weak NN coupling constants. Improved experiments in the bare NN system would greatly improve this situation by introducing results with a minimum of theoretical uncertainties. The measurement of the neutron spin-rotation in a hydrogen target would provide such an opportunity.

Spin-rotation experiments in heavy nuclei [HRG$^+$82],[HFR$^+$84] have shown the ability of neutron polarimeters to measure small spin-rotation observables. A sensitive measurement of the isovector, neutron spin-rotation in a liquid parahydrogen (spin zero) target ($\vec{n}+p$ system) would provide a direct determination of the pion coupling constant. However, the experimental drawbacks of the $\vec{n}+p$ system include working with an explosive substance (hydrogen gas), maintaining a 22K target reservoir, and reducing systematic uncertainties from scattering.

The spin-rotation in a liquid helium target ($\vec{n}+\alpha$ system) is experimentally more feasible. This system is sensitive to both the isovector and isoscalar coupling constants and is the isospin analog of the $\vec{p}+\alpha$ system studied by Lang *et al.* The experimental difficulties are greatly reduced for a helium target system because the helium gas does not impose additional safety hazards, a 4K cryogenic reservoir is

easier to maintain and the scattering effects are significantly less. In addition, the apparatus and experience gained in the execution of the $\vec{n} + \alpha$ experiment will be directly applicable to future experiments in the $\vec{n} + p$ system.

Although interpreting the results in the helium system requires some nuclear structure calculations, the spin-rotation measurement in the helium system is of considerable theoretical interest. The $(\vec{n} + \alpha)$ 5-body system can be calculated with less uncertainty than in heavier nuclear systems. Currently the controversial ^{21}Ne experiment provides the only measurement for the neutron-nucleus part of the weak interaction. A definitive spin-rotation measurement in the $\vec{n} + \alpha$ system would provide direct information to determine the strength of the PNC neutron-nucleus force. [Des97], [Des98] In addition, this measurement would provide the first opportunity to directly compare two isospin mirror systems: $\vec{n} + \alpha$ and $\vec{p} + \alpha$. Combining the results from the $A_{\mathrm{L}}(\vec{p}, \alpha)$ and $\varphi_{PNC}(\vec{n}, \alpha)$ experiments will provide a new way to constrain both f_π and h^0_ρ.

Chapter 3

NEUTRON SPIN-ROTATION THEORY

In 1964, Michel first proposed that the weak interaction could produce an observable effect with neutrons that is analogous to the observed optical rotation of polarized photons propagating through a "handed" medium [Mic64]. Sub-thermal neutrons that propagate through a crystal of spin-zero nuclei experience a parity-violating rotation of the spin polarization vector. Under these conditions the Coulomb, magnetic, and spin-dependent nuclear interactions are absent. This effective neutron "optical rotation" was confirmed in the first spin-rotation experiments carried out in the tin isotopes [FHR$^+$80].

For thermal energies and below, E$\leq$0.025 eV, the de Broglie wavelength of neutrons ($\lambda = h/p$) is on the order of, or greater than, the interatomic spacing in materials. At these wavelengths ($\lambda > 1$ Å), the wave properties of neutrons predominate over their particle characteristics, and the theory of neutron optics is applicable.

In analogy with light, we apply the wave theory to the treatment of neutron scattering. For a single scattering center, the neutron wavefunction outside of the potential well is given by the sum of the incident plane wave and the scattered wave as

$$\psi_n = e^{i\vec{k}\cdot\vec{r}} + f(\theta)\frac{e^{ikr}}{r} \tag{3.1}$$

where $f(\theta)$ is the scattering amplitude, and $|\vec{k}|$ is the neutron wave vector given by

$$|\vec{k}| = (2\pi)/\lambda = |\vec{p}|/\hbar \tag{3.2}$$

In general, the scattered wave amplitude is a function of scattering angle, θ, with respect to the incident wave direction, $\vec{k}$.

The effective square well potential for a neutron scattering from a nucleus by the strong interaction can be described by a depth of $V_o \approx 40$ MeV and radius $R = R_o A^{\frac{1}{3}}$ where $R_o = 1.2$ fm and A is the nuclear mass ($R \sim 2$ fm for helium) [RGL91]. In this case, we have

$$kR = \frac{2\pi R}{\lambda} \ll 1 \tag{3.3}$$

Scattering with non-zero angular momentum ($mvr = n\hbar$) implies an incident impact parameter of $b \sim \lambda/2\pi$ which for our condition of $\lambda > 1$ Å, is greater than the short range of the strong nuclear force. Thus, long-wavelength neutron scattering is predominantly s-wave, (zero angular momentum) and isotropic. As a result, the scattered wave amplitude must be independent of angle [KS77a].

$$f(\theta) = f(0) = -a \tag{3.4}$$

where a is the scattering length.

3.1 Index of refraction for a neutron wave

In analogy with geometric optics for light, an incident neutron plane wave is refracted in a medium. In this section, we derive an expression relating the effective index of refraction to the coherent forward scattering amplitude, $f(0)$.

For a collection of nuclei, the quantum mechanical wave equation satisfied by a neutron can be written as follows.

$$[\nabla^2 + k^2]<\psi_n> = 0 \tag{3.5}$$

$$\begin{aligned} \text{where} \quad k^2 &= k_o^2 = \frac{2mE}{\hbar^2} && \text{outside the medium,} \\ k^2 &= k_i^2 = \frac{2m}{\hbar^2}(E - (V + iW)) && \text{inside the medium,} \end{aligned}$$

$<\psi_n>$ is the energy averaged wavefunction for the neutron, and V and W are the real and imaginary parts of the effective scattering potential for the medium. We assume that for slow neutrons, $E < 1$ eV, the scattering potential is independent of wavelength of the incident neutron. In geometric optics, the effective index of refraction is given by the ratio of velocities inside and outside the medium. Similarly, the effective index of refraction is simply the ratio of the wavenumbers.

$$\mathsf{n}^2 = \frac{k_i^2}{k_o^2} = \left(1 - \frac{V + iW}{E}\right) \tag{3.6}$$

Using the above relations between the index of refraction, n, and the wavenumber, k, we can express the wave equation inside the medium as

$$[\nabla^2 + k_o^2 \mathsf{n}^2] <\psi_n> = 0 \tag{3.7}$$

The familiar plane-wave form of the wavefunction that satisfies this equation is given by

$$<\psi_n> \sim e^{i\vec{k}\cdot\vec{r}} \sim e^{i\mathsf{n}\vec{k}_o\cdot\vec{z}} \sim e^{-\mathrm{Im}(\mathsf{n})\vec{k}_o\cdot\vec{z}} e^{i\mathrm{Re}(\mathsf{n})\vec{k}_o\cdot\vec{z}} \tag{3.8}$$

If the imaginary part of the potential (associated with absorption) is nonzero ($W \neq 0$), then the wave is attenuated as it propagates through the medium. The real part of the potential (associated with elastic scattering) contributes a phase to the neutron wave as it travels through the medium. This phase is given by

$$\phi = \mathrm{Re}(\mathsf{n}) k_o z \qquad \text{for} \qquad \vec{k}_o = k_o \hat{z} \tag{3.9}$$

where $\hat{z}$ is defined as the incident neutron (beam) direction.

In the classical description of the refraction of light, the secondary scattered waves are coherent (for a non-absorptive medium) and the amplitudes add to a nonzero value only in the forward direction. In this case, the index of refraction is related to the phase shift between the refracted wave and the original wave which are summed at 0°. The index of refraction can therefore be expressed in relation to the coherent forward scattering amplitude of the medium.

The refraction of a neutron wave in a medium resembles the behavior of the refraction of light in a gas where the average coherent scattering contributes to the index of refraction and the variation in amplitude over individual scatterers (nuclei in the neutron case) contributes to the incoherent scattering [Hug54].

In the quantum mechanical treatment of the neutron wave, the phase shift of the wavefunction at the medium boundary can be related to the depth of the scattering potential well for an individual nucleus. The average of this potential over the nuclei in the medium gives the average scattering potential [Hug54], [GW64]

$$V \approx \bar{V} = \left(\frac{2\pi\rho\hbar^2}{m}\right) a \tag{3.10}$$

where ρ is the material number density and a is the scattering length defined in Equation 3.4, which is directly proportional to the phase shift. This expression can also be obtained by integrating the effective Fermi potential (a non-physical step potential) over an isotropic distribution of scatterers [RGL91].

We consider here only non absorptive media, for which $W = 0$. Substituting Equation 3.10 into Equation 3.6, and using the low-energy relation between the neutron energy and momentum, $(E = p^2/2m)$, gives the following relationship between the index of refraction and the scattering length:

$$\mathsf{n}^2 = \left(1 - \frac{4\pi\rho\hbar^2 a}{p^2}\right) \tag{3.11}$$

Taking the square root, and using Equation 3.4 and the de Broglie relation $p = \hbar k$, the index of refraction can be written in terms of the forward scattering amplitude as

$$\mathsf{n} = 1 - \frac{2\pi\rho\hbar^2 a}{p^2} = 1 + \left(\frac{2\pi}{k^2}\right)\rho f(0) \tag{3.12}$$

where k is assumed to be the incident wave vector outside the medium and the subscript has been dropped. This relation between the index of refraction for a neutron wave in a medium and the forward scattering amplitude is analogous to the Lorentz relation for light traveling through a medium. For most nuclei, the

scattering length is positive, and the index of refraction is less than 1 by a very small amount. To illustrate this, for an incident neutron of 5 Å (E=.003 eV) on liquid helium with density $\rho = 0.19 \times 10^{23}/\text{cm}^3$ and scattering length +3 fm [KS77b], we obtain $1 - n = 2 \times 10^{-6}$.

3.2 Rotation of the spin polarization vector by the weak interaction

For low energy neutrons, the coherent forward scattering amplitude is given by:

$$f(0) = A + B\vec{\sigma}_n \cdot \vec{S}_N + C\vec{\sigma}_n \cdot \vec{k}_n + D\vec{S}_N \cdot \vec{k}_n + E\vec{\sigma}_n \cdot (\vec{k}_n \times \vec{S}_N) \tag{3.13}$$

where $\vec{\sigma}_n$ and $\vec{k}_n$ are the neutron spin and wave vector (momentum), $\vec{S}_N$ is the spin of the target nuclei, and higher order terms in the neutron momentum have been neglected. We will consider systems with zero nuclear spin ($<\vec{S}_N> = 0$) so that the forward scattering amplitude is reduced to two terms. The first surviving term is the parity conserving term, A, containing contributions from the strong, weak and electromagnetic interactions. The second term, proportional to $\vec{\sigma}_n \cdot \vec{k}_n$, is odd under parity transformations and thus contains only contributions from the weak interaction.

We express Equation 3.13 in parity-conserving and parity-nonconserving terms as

$$f(0) = f_{PC} + f_{PNC}(\vec{\sigma}_n \cdot \vec{k}_n) \tag{3.14}$$

The PNC part of the scattering amplitude is proportional to the weak interaction matrix element as given by [DFST83]

$$f_{PNC} = \frac{-M}{2\pi}\text{Re}<^4\text{He}, \psi_i|\mathcal{H}_{wk}|\psi_o{}^4\text{He}> \tag{3.15}$$

where M is the mass of the neutron and ψ_o and ψ_i are the outgoing and incoming neutron wavefunctions. The weak interaction matrix element is given for the neutron interacting with the nucleus of the medium (here explicitly expressed for helium).

Since the weak interaction violates parity, there is a different forward scattering amplitude, $f_{\pm}$, for $\vec{\sigma}_n \cdot \vec{k}_n = \pm k$. As a result, the indices of refraction, n_+ and n_-, are different for the two helicity states. Therefore, as a neutron wave propagates in a medium, the two helicity states accumulate a different phase. We combine Equations 3.9, 3.12, and 3.14 to obtain an expression for the two phases and identify the parity-conserving and parity-violating terms.

$$\phi = kz\left(1 + \frac{2\pi\rho}{k^2}(f_{PC} + f_{PNC}(\vec{\sigma}_n \cdot \vec{k}_n))\right) \tag{3.16}$$

$$\phi_{\pm} = \phi_{PC} \pm \phi_{PNC} \tag{3.17}$$

where

$$\phi_{PC} = kz\left(1 + \frac{2\pi\rho}{k^2} f_{PC}\right) \tag{3.18}$$

$$\phi_{PNC} = 2\pi\rho z f_{PNC} \tag{3.19}$$

The parity-nonconserving contribution to the phase is independent of neutron energy and directly proportional to the weak interaction matrix elements through the parity violating part of the forward scattering amplitude.

Transverse polarization is a linear combination of equal contributions from the two helicity states. For example, we write for the spin "up" state,

$$|up> = \frac{1}{\sqrt{2}}(|+> + |->) \rightarrow \frac{1}{\sqrt{2}}((e^{i\phi_+})|+> + (e^{i\phi_-})|->) \tag{3.20}$$

As a transversely polarized neutron travels through a medium, the accumulated phase difference between the two helicity states alters the polarization state. Using the above expression for the phase, we can write the transverse polarization state in terms of the PC and PNC contributions to the phase.

$$\frac{1}{\sqrt{2}}((e^{i\phi_{PC}}e^{i\phi_{PNC}})|+> + (e^{i\phi_{PC}}e^{-i\phi_{PNC}})|->) \tag{3.21}$$

The PC phase, ϕ_{PC}, contributes an overall phase factor dependent upon the PC scattering amplitude. The PNC phase produces a rotation about the propagation

axis. (Refer to Equation 4.3 for the expression of the rotation matrix $\mathcal{R}_z(\theta)$, where z is the propagation axis.) The result is a rotation of the transverse polarization vector by an amount $2\phi_{PNC}$ as the neutron propagates through the medium.

The parity-violating rotation angle of the transverse spin, φ_{PNC} is therefore the accumulated difference in phase between the two helicity states.

$$\varphi_{PNC} = \phi_+ - \phi_- = 2\phi_{PNC} = 4\pi\rho z f_{PNC} \tag{3.22}$$

A positive phase difference (when $f_{PNC}(+\text{helicity}) > f_{PNC}(-\text{helicity})$) induces a rotation about the neutron momentum that follows the sense of a right handed screw.

The discussion above included only the real part of the scattering amplitude. The weak interaction contribution to the imaginary part of the scattering amplitude causes a very small difference in scattering cross section for the two helicity states. This produces a non-zero longitudinal analyzing power and a rotation of the spin in the plane defined by the transverse polarization vector and the momentum direction. For elastic scattering, these effects are directly proportional to the momentum, and therefore can be neglected for the case of very low energy neutrons, ($\frac{\delta\sigma}{\sigma} \approx 10^{-10}$ for thermal neutrons) [Sto74].

In summary, as a result of the parity-violating weak interaction, positive and negative helicity neutrons travel through a medium with different effective indices of refraction. We observe the resulting phase difference between helicity states as a rotation about the momentum direction of the transverse spin polarization vector by an amount proportional to the weak interaction matrix element.

3.3 Theoretical predictions for the parity-violating spin-rotation in ^{4}He

In 1982, Avishai predicted the $\vec{n}+\alpha$ spin-rotation angle using a non-relativistic PNC hamiltonian and a simplified dependence of the scattering amplitude on the weak interaction coupling strength as developed by Michel. Correction factors developed

by Stodolsky were used to incorporate the effects of the strong interaction. Avishai obtained a result of $\varphi \approx 7.3 \times 10^{-7}$ rad/m [Avi82].

It is interesting to note that this value is much larger than that obtained from taking the results of a partial-wave-born-approximation calculation for tin, and simply scaling the result for a target of 2 protons and atomic mass 4. The enhancement comes from the distortion of the neutron wavefunction by the strong interaction potential. In addition, Avishai estimated the contribution to the $\vec{n} + \alpha$ spin-rotation from the neutron-electron weak interaction as 6×10^{-8} rad/m, which is certainly too small to discern from the nuclear contribution [Avi82].

Dmitriev *et al.* calculated the $n + \alpha$ nuclear matrix element using the weak interaction hamiltonian in the one-boson exchange approximation as derived by Desplanques, Donoghue, and Holstein [DDH80]. They obtained an expression for the neutron spin-rotation in helium in terms of the nucleon-nucleon weak interaction meson exchange couplings [DFST83].

$$\varphi = -(0.97 f_\pi + 0.22 h_\omega^0 - 0.22 h_\omega^1 + 0.32 h_\rho^0 - 0.11 h_\rho^1 - 0.02 h_\rho^{'1}) \text{rad/m} \qquad (3.23)$$

Dmitriev *et al.* present a result "for reasonable parameters of the interaction", using the DDH "best values", of $\varphi = (-0.1 \pm 1.5) \times 10^{-6}$ rad/m.

Substituting the exchange coefficients that best fit the existing nucleon PNC data [HH95] into Equation 3.23, we predict a rotation of -0.7×10^{-7} rad/m. Both the Avishai result and the "best fit" result are consistent with the "reasonable range" rotation given above. The linear relation between the expected spin-rotation and the coupling constant, f_π is presented in Figure 3.1.

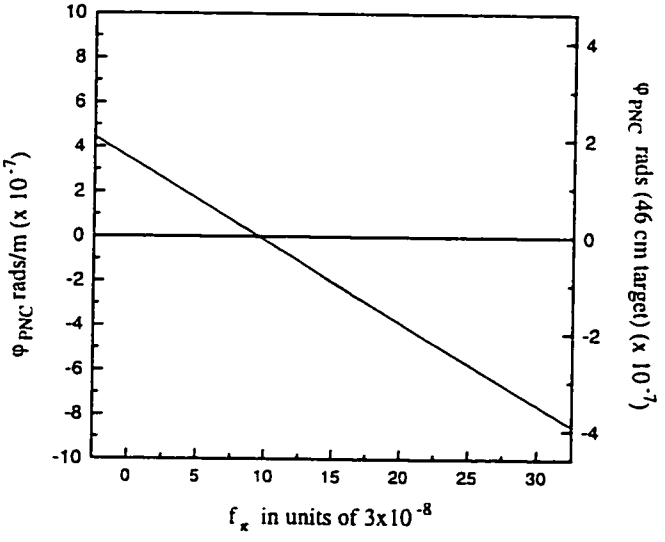

Figure 3.1: Relation between the expected spin-rotation in the $(\vec{n}+\alpha)$ system, φ_{PNC} and the isovector coupling constant, f_π presented in units of the sum-rule value 3.8×10^{-8}. The left axis gives the rotation in radians per meter, while the right axis gives the spin-rotation in radians for our target length of 46 cm.

Chapter 4

DESIGN OF THE SPIN-ROTATION APPARATUS

In this chapter, we discuss the design of the apparatus to measure the neutron spin-rotation in a helium target. The major challenge of this spin-rotation experiment lies in reducing systematic errors induced by magnetic field rotations and from neutron scattering effects. Achieving the systematic limits necessary to reach a measurement sensitivity of 5×10^{-8} radians dominates the design criteria.

4.1 Measurement of the neutron spin-rotation, φ

The experiment uses a beam of transversely polarized, cold neutrons, with energies in the 10^{-3} eV range. As derived in Section 3.2, the parity-violating spin-rotation, is linearly dependent upon the target length, ℓ, and the density, ρ. Equation 3.22 is repeated here for clarification.

$$\varphi_{PNC} = 4\pi\rho\ell f_{PNC} \tag{4.1}$$

To maximize the signal in the $(n+\alpha)$ system, a liquid helium target is used.

By the same reasoning, a long target length would be desirable. However, increasing the target length increases the beam losses from divergence and scattering in the targets. If statistical precision were the dominant consideration, then the optimum target length for a divergenceless beam would be 2 mean free paths. The mean free path of 5Å neutrons in liquid helium at 4.25 K is 1 meter, and for 7Å neutrons it is 2 meters. [SDG55] We chose a length of 18 inches (46 cm) for the target chambers to reduce the scattering losses and for convenience of construction.

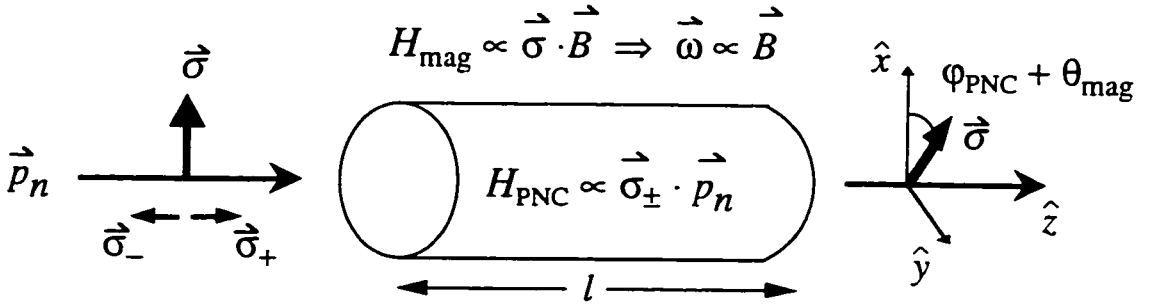

Figure 4.1: Simplified representation of an experiment for measuring φ_{PNC}.

In analogy with optical rotation experiments, the neutron spin-rotation is measured by passing the transmitted neutrons through an analyzer whose polarization direction is rotated 90 degrees with respect to the initial polarization axis. Note that this corresponds to optical polarizers with a 45 degree offset. We position the polarizers with a 90 degree offset to be linearly sensitive to the neutron spin-rotation angle.

A schematic representation of the spin-rotation experiment is given in Figure 4.1.

A neutron initially transversely polarized in the spin-up state along $\hat{x}$ is described by a linear combination of helicity states along the beam direction, $\hat{z}$, as given by Equation 3.20.

$$|+\hat{x}> = \frac{1}{\sqrt{2}}(|+> + |->) \tag{4.2}$$

Employing the following rotation matrices,[FLS63]

$$\mathcal{R}_z(\theta) = \begin{pmatrix} e^{\frac{i\theta}{2}} & 0 \\ 0 & e^{\frac{-i\theta}{2}} \end{pmatrix}; \qquad \mathcal{R}_x(\theta) = \begin{pmatrix} \cos\frac{\theta}{2} & i\sin\frac{\theta}{2} \\ i\sin\frac{\theta}{2} & \cos\frac{\theta}{2} \end{pmatrix} \tag{4.3}$$

$$\mathcal{R}_y(\theta) = \begin{pmatrix} \cos\frac{\theta}{2} & -\sin\frac{\theta}{2} \\ \sin\frac{\theta}{2} & \cos\frac{\theta}{2} \end{pmatrix}$$

for a rotation of θ about the specified axis, we derive an expression for the rotated polarization state. After a distance, z, the polarization vector has rotated an amount, φ, about the momentum axis, $\hat{z}$, and the new state is given by

$$|\varphi> = \mathcal{R}_z(\varphi)|\hat{x}> = \frac{1}{\sqrt{2}}((e^{\frac{i\varphi}{2}})|+> + (e^{\frac{-i\varphi}{2}})|->) \tag{4.4}$$

(Note that this expression agrees with Equation 3.21 derived for the PNC rotation about the momentum axis.)

The expression for the "up" state in the analyzer direction, $+\hat{y}$, (which is transverse to both the momentum and the initial polarization), is found from a 90 degree rotation of the $\hat{x}$ state about the z axis. We obtain,

$$|+\hat{y}> = \frac{1}{2}[(1+i)|+> + (1-i)|->)] \tag{4.5}$$

The count-rate is the square of the amplitude for the rotated state, $|\varphi>$, to be in the $+\hat{y}$ configuration and is given by the square of the vector product of the two states as follows:

$$\begin{aligned} N_+ = |<\hat{y}|\varphi>|^2 &= \frac{1}{8}|(1-i)e^{\frac{i\varphi}{2}} + (1+i)e^{\frac{-i\varphi}{2}}|^2 \\ &= \frac{1}{2}(1+\sin\varphi) \end{aligned} \tag{4.6}$$

Similarly, the expression for the count-rate for the $-\hat{y}$ state is given by

$$N_- = \frac{1}{2}(1+\sin\varphi) \tag{4.7}$$

Thus, the rotation angle, φ, of the spin about the momentum axis in the ideal case is given by

$$\sin\varphi = \frac{(N_+ - N_-)}{(N_+ + N_-)} \tag{4.8}$$

where a positive rotation, φ, is given by a right-hand rotation about the neutron momentum direction, $\vec{p}_n = p_n\hat{z}$. To measure the neutron spin-rotation, the experiment involves counting neutrons from a crossed polarizer ($\hat{x}$), and analyzer ($\hat{y}$) system, in which the final analyzer direction alternates, between $+\hat{y}$ and $-\hat{y}$.

4.2 *Spin-rotation polarimeter*

A polarimeter for measuring the spin-rotation of transversely polarized neutrons through solid targets was developed by Heckel *et al.*[Hec81] This polarimeter consisted of a target region located between a crossed polarizer and analyzer pair. The target region is divided into two target positions separated by the "π-coil". The π-coil magnetic field axis is aligned along $\hat{x}$, the direction of the initial neutron polarization, and the field strength is set so that the neutron spin precesses about $\hat{x}$ by 180 degrees as it passes through the coil. The π-coil thereby reverses the sign of the upstream spin-rotations in the xy plane relative to rotations downstream of the coil.

A progression of the neutron spin through the polarimeter is illustrated in Figure 4.2. When the target was shuttled between positions upstream and downstream of the π-coil, the PNC signal alternates in sign while any constant residual magnetic fields (θ_M) produce a steady background rotation. Subtracting the measurements in the two target positions eliminates the background rotation, leaving twice the value of the PNC rotation. This subtraction technique assumes that the background rotations are target independent.

The first experiments in tin isotopes and later with lanthanum (all solid targets) proved that the polarimeter can successfully measure the neutron spin-rotation to a sensitivity of 10^{-4} radians/meter [FHR$^+$80], [HFR$^+$84]. The spin-rotation measurement in the $n + \alpha$ system required nearly 2 orders of magnitude better sensitivity, and necessitated improvements to the apparatus design.

The reactor power fluctuates on the order of 1%, which appears as random noise in the count-rates. This fluctuation must be eliminated from the data in order to achieve a measurement sensitivity that is limited by the Poisson statistics of the detected neutrons.

Reactor power fluctuations do not alter the neutron beam profile which is determined by the long guide tubes located upstream between the reactor cold source

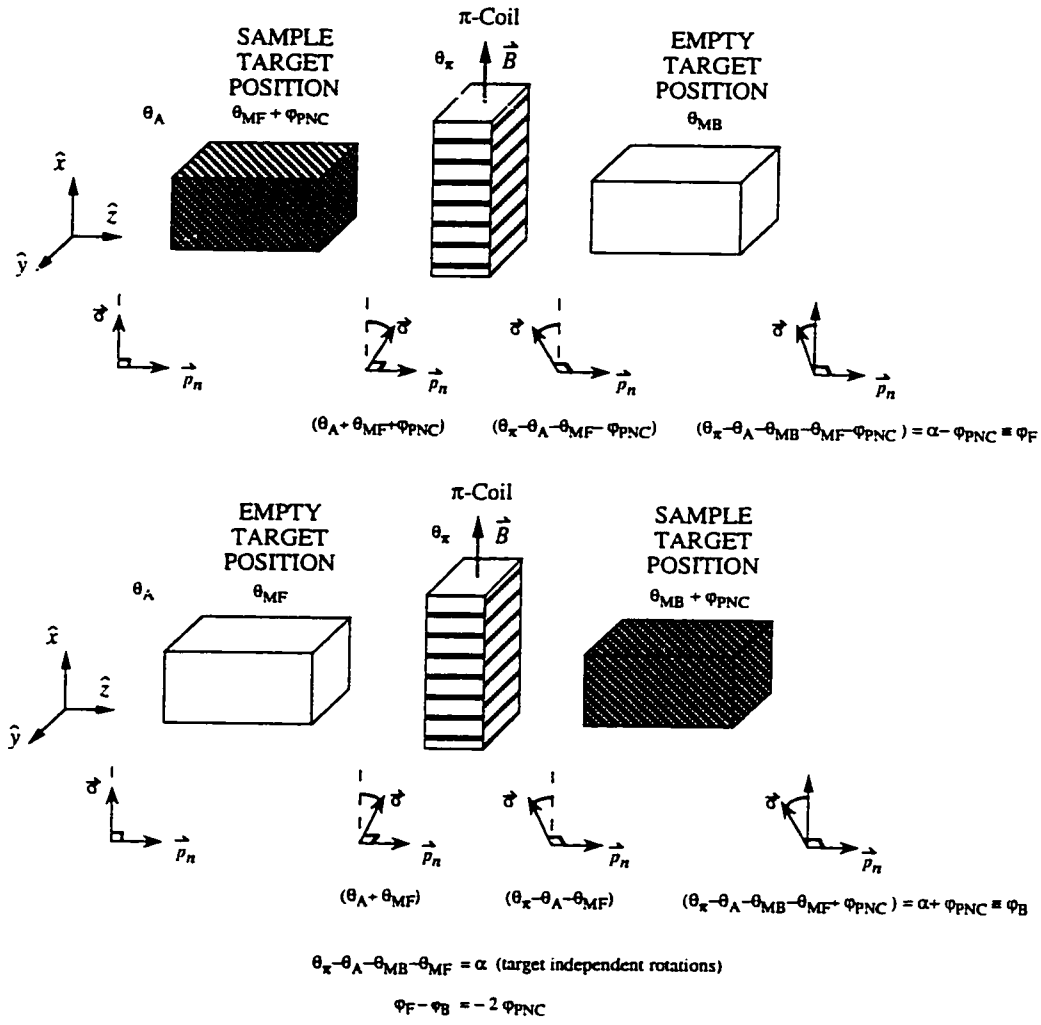

Figure 4.2: Progression of the neutron spin through the polarimeter. Rotations from magnetic fields are indicated with a subscript, "M", rotations from misalignment of the polarimeter are denoted with the subscript, "A", and "F" and "B" denote the front and back target regions respectively. Rotations from the leakage fields of the π-coil are indicated by θ_π.

and the apparatus. Therefore, reactor fluctuations cause equivalent changes in the neutron flux in the right and left halves of the apparatus. A comparison of the counts measured in the two sides decreased our signal's sensitivity to the noise caused by reactor fluctuations in the neutron count-rates.

We modified the polarimeter to measure the PNC signal from both the front and back target positions simultaneously. We divided the apparatus into two side-by-side sections in which each half effectively constitutes a separate experiment run under the same conditions. This is shown schematically in Figure 4.3.

The targets were alternately filled in a diagonal pattern, so that the PNC rotation always had opposite signs on the two sides of the apparatus. While the front target chamber contained liquid helium on one side, the other beam side had the back target chamber filled, where front and back is with respect to the π-coil. This target state then alternated with the flipped state in which the previously empty diagonally positioned target chambers were then filled. The beam line, the target chambers, the π-coil, and the detector were all divided into two side-by-side regions, designed to prevent neutrons from crossing over from one side to the other.

The benefit of modulating the PNC signal against the constant PC signal in the two halves of the system is shown in Figure 4.3. We initially ratio the counts in the right and left sides, forming an expression that is equivalent to subracting the two asymmetries. We then subtracted the results for the two target states, leaving the PNC signal and residual magnetic field contributions. As can be seen in the figure, this comparison technique is limited by the assumption that the background rotations are the same for both target states and to a lesser degree, are the same on the left and right sides. The design of the apparatus was dominated by the challenge of reducing to the level of 5×10^{-8} radians, the difference in background rotations measured for the two target positions.

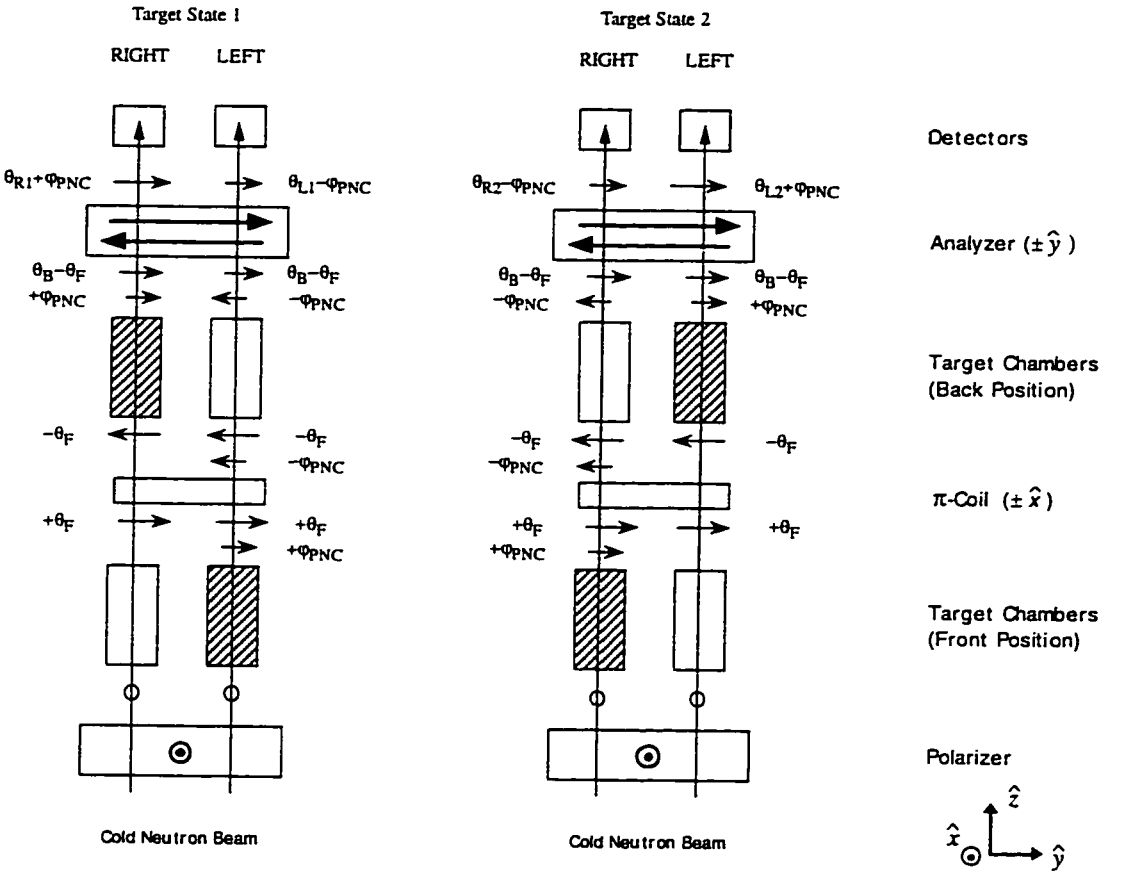

Figure 4.3: Schematic diagram of the neutron spin through the new polarimeter. The projection of the rotation angle onto the $\hat{y}$-axis is shown at various positions along the apparatus. θ is the magnetic rotation angle, where subscripts F and B refer to the front and back target regions, and R1, for example refers to the detector position (right or left side) and target state (1 or 2).

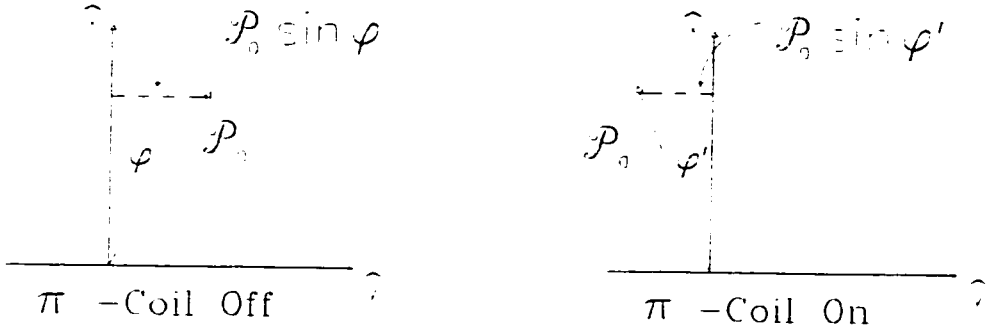

Figure 4.4: Schematic representation of the polarization product factors.

4.3 Measurement of φ in a non-ideal polarimeter

In an ideal polarimeter, a 100% efficient polarizer and analyzer are perfectly aligned 90° from each other and the neutrons remain polarized as they traverse the system. However, in our apparatus, the polarizers were imperfect, and the π-coil caused a spread in the polarization of the neutron beam. We introduce the polarization product factor, defined to be 1 in the ideal system, that takes into account the reduction in neutron beam polarization.

The diagrams in Figure 4.4 give a visual explanation of the polarization product factor. We define $\mathcal{P}_0$ as the length of the polarization vector, and for perfectly polarizing supermirrors, is equal to 1. $\mathcal{P}_0$ becomes less than one to account for the admixture of the other spin state.

To first order, the π-coil did not change the length of the neutron polarization vector, $\mathcal{P}_0$. The π-coil does, however, alter the transverse projection of the angle for rotations other than 180°. Our signal was proportional to this transverse projection, and we define a π-coil dependent polarization product, $\mathcal{P}_\pi$, to account for the effect on the measured rotation angle. For the case of rotations upstream of the π-coil, we

have from Figure 4.4

$$\mathcal{P}_0 \sin\varphi' = \mathcal{P}_0 r_\pi \sin\varphi = \mathcal{P}_\pi \sin\varphi \tag{4.9}$$

where

$$\mathcal{P}_\pi \equiv \mathcal{P}_0 r_\pi \tag{4.10}$$

and r_π is the transverse spin reduction factor (nominally between 0.4 and 0.7).

The measured count-rate asymmetry in a non-ideal polarimeter is no longer equal to the spin-rotation angle and Equation 4.8 must be modified:

$$\mathcal{P} \sin\varphi = \frac{(N_+ - N_-)}{(N_+ + N_-)} \tag{4.11}$$

where φ is the total rotation angle from all sources and $\mathcal{P}$ is the polarization product factor, and $0 \leq \mathcal{P} \leq 1$. For an ideal system, $\mathcal{P} = 1$, and we recover Equation 4.8.

With a polychromatic neutron beam, the π-coil smears the polarization of the neutrons. A neutron precesses about the π-coil magnetic field by an amount proportional to the time spent in the field, therefore the precession angle was inversely proportional to the neutron velocity, or linearly dependent upon the wavelength. With a monochromatic beam, the π-coil current can be set to rotate all the neutrons the desired 180 degrees. However in our case, for a polychromatic beam, the π-coil current was optimized to rotate the majority of the neutrons by an angle close to 180 degrees as possible, while some neutrons are necessarily over-rotated and others are under-rotated. The measured angle was an energy averaged value of the spread in transverse components of the polarization vector. A measurement of the polarization products gives the effective reduction in the angle.

Running the experiment on a polychromatic beam line reduces the measured rotation angles by the effective transverse spin reduction factor which is about two for rotations produced upstream of the π-coil. The increase in neutron counts by a factor of about 300 for a polychromatic beam compared to a monochromatic beam allows for much better statistics and outweighs the increase in error introduced with the polarization products.

The procedure to optimize the π-coil current setting is discussed in Section 6.2.2 and the measurement of the polarization products is discussed in Section 6.2.3.

4.4 Expected sensitivity and design goals

In order to measure a spin-rotation angle on the order of 1×10^{-7}, we seek an experimental sensitivity on the order of 5×10^{-8}. The apparatus was designed to achieve this systematic limit.

To estimate the error in $\sin\varphi$, we start with Equation 4.11, and sum the errors in quadrature for uncorrelated measurements N_+, N_-, and polarization product, $\mathcal{P}$.

$$(\sigma_{\sin\varphi})^2 = \left(\frac{\partial(\sin\varphi)}{\partial N_+}\right)^2 \sigma_{N_+}^2 + \left(\frac{\partial(\sin\varphi)}{\partial N_-}\right)^2 \sigma_{N_-}^2 + \left(\frac{\partial(\sin\varphi)}{\partial \mathcal{P}}\right)^2 \sigma_{\mathcal{P}}^2 \quad (4.12)$$

$$= \frac{4N_+N_-}{\mathcal{P}^2(N_+ + N_-)^3} + \left[\frac{1}{\mathcal{P}}\left(\frac{(N_+ - N_-)}{(N_+ + N_-)}\right)\right]^2 \left(\frac{\sigma_{\mathcal{P}}}{\mathcal{P}}\right)^2 \quad (4.13)$$

where we have used the statistical error on a large number of counts given by the Poisson distribution standard deviation, $\sigma(N_\pm) = \sqrt{N_\pm}$. We define a "total" count-rate of $\mathcal{N} = N_+ + N_-$, where $N_+ \approx N_- \approx \frac{1}{2}\mathcal{N}$, and calculate the error in φ in terms of the total counts and the error in $\mathcal{P}$ as

$$\sigma_{\sin\varphi} = \frac{1}{\mathcal{P}}\sqrt{\left[\frac{1}{\mathcal{N}} + \sin^2\varphi\,(\sigma_{\mathcal{P}})^2\right]} \quad (4.14)$$

From the second term in Equation 4.14, we obtain a limit on the fractional error of $\mathcal{P}$ of less than 10^{-4} given an average rotation of 1 mrad and an overall error of less than 10^{-7}. If we consider the statistical contribution, the first term in Equation 4.14, and neglect the error in the polarization product factor, we obtain

$$\sigma_{\sin\varphi} = \frac{1}{\mathcal{P}}\frac{1}{\sqrt{\mathcal{N}}} \quad (4.15)$$

With a statistical limit of 5×10^{-8}, and a count-rate of 10^8 neutrons per second, we can achieve this limit in about 46 days of continuous 24 hour data accumulation time. A more practical statistical limit for the initial run of the spin-rotation apparatus was

1×10^{-7} which could be attained in about 2 weeks of continuous data accumulation. The actual statistical limits achieved during the first data run of the spin-rotation experiment are discussed in Chapter 7. The reduction of systematic contributions to $\sigma_{\sin\varphi}$, is discussed in the remainder of this Chapter.

4.5 *Reduction of parity-conserving background rotations*

We wish to measure the small parity-violating spin-rotation. However, relatively large parity-conserving rotations, predominately from the precession of the spin about a magnetic field, contribute to the measured count-rate asymmetry defined in Equation 4.11. Although the split-beam polarimeter with a two target system was designed to separate constant background rotations from the modulated PNC signal, the method was limited to the extent that the two target states produced the same background rotations. Parity-conserving changes in the spin-rotation that are dependent upon the target position, will mimic the PNC signal. We consider here the sources of PC spin-rotations and discuss ways to minimize their contribution to our PNC signal. For clarity of the discussion, we consider the ideal case where the polarization products are equal to 1.

The measured spin-rotation angle, φ, (defined in Equation 4.11) is a combination of the PC and PNC contributions as follows,

$$\varphi = \phi_{targ} + \alpha \tag{4.16}$$

where

$$\phi_{targ} = \varphi_{\mathrm{PNC}} + \varphi_{\mathrm{PC}targ} \tag{4.17}$$

$$\alpha = \text{target independent rotations} \tag{4.18}$$

A distinction is made between the contributions from parity conserving target dependent rotations, $\varphi_{\mathrm{PC}targ}$, and those parity conserving rotations that are independent of

target position, α. Contributions to each of these terms are discussed in the following subsections.

4.5.1 Magnetic field rotations

The neutron spin will precess about residual magnetic fields in the target region with a frequency ω, that is proportional to the magnetic field B. The spin precession angle for a neutron traveling a time t, with velocity v, and distance d, is given by

$$\omega = -\gamma B \tag{4.19}$$

$$\theta_{mag} = -\gamma B t = \left(\frac{6\pi}{v}\text{rad/m/mG}\right)(B[\text{mG}])(d[\text{m}]) \tag{4.20}$$

$$\text{where} \qquad \gamma = -3\,\text{Hz/mG} \tag{4.21}$$

is the gyromagnetic ratio for the neutron. (See Appendix A for details.) For 7 Å neutrons traveling 1 meter in a 1 mGauss field, $\theta_{mag} = 35$ mradians.

An axial field (parallel to the momentum) rotates neutrons in the same plane as the PNC effect, producing relatively large spin-rotation asymmetry signals that can limit our ability to see a PNC rotation on the order of 10^{-7} radians. Therefore, the targets are housed in a low-field region (less than 0.1 mG) created by μ-metal magnetic shielding. (The shielding configuration is discussed in Section 5.7.) The magnetic field constraint is determined by the most stringent requirement from the effect of the slowing down of neutrons in the liquid helium. This is discussed in Section 4.5.3.

A residual axial magnetic field of 100 μGauss in the target region of length 1 meter rotates 5Å neutrons approximately 2.5 mrads. This is the magnitude of the residual background PC rotations, α, in Equation 4.16 and in Figure 4.2.

A symmetric field distribution with nearly identical fields in the two target positions as well as in the two sides of the beam will produce background rotations that tend to cancel in the subtraction scheme. Therefore, variations in the magnetic

fields must also be small, and occur on time scales long compared to the data acquisition time for one target state. To minimize local field gradients within the target region, we used only non-magnetic materials. Fringing fields from nearby magnets (in particular from those coils which change polarity) must also satisfy the low field requirement.

We exploit the condition that the magnetic field rotations are velocity dependent while the PNC effect is independent of velocity. We designed the detector to measure neutron counts as a function of velocity which allowed us to monitor the magnetic field rotations. The segmented ^{3}He ionization chamber has 4 collection regions along the beam axis. Since the neutron absorption cross section is inversely proportional to velocity, the average energy of the captured neutrons increases with each collection region along the axis. We minimized the background magnetic field rotations by adjusting external field coils until the asymmetries were equal in all detector regions. This procedure is described in detail in Section 6.2.4. This detector design enabled the continuous monitoring of magnetic field drifts and sudden changes in ambient magnetic fields.

In addition, each of the detector regions were divided into quadrants to separately measure the count-rate asymmetries in the two halves of the apparatus, and to monitor the upper and lower regions independently. The spatial separation provides a means to test for up/down asymmetric fringing fields. The detector is discussed in detail in Section 5.8.

4.5.2 Effects of strong interaction neutron scattering

The dominant strong interaction of cold neutrons in a liquid helium target is coherent scattering. The absorption cross section for ^{4}He is negligibly small, and the incoherent scattering cross section is zero. The ^{3}He absorption cross section is 5333 barns, the scattering cross section is 5.6 barns, and the natural relative abundance is a factor of 10^{-6} compared to ^{4}He. The ^{3}He contamination is not a problem, because it produces

a small neutron loss mechanism and does not contribute to a false asymmetry.

The free atom scattering cross section for ^{4}He is approximately 0.76 barns, and the bound atom coherent scattering cross section is 1.2 b. However, as will be discussed below, neither of these cross sections adequately describes the scattering of cold neutrons in a liquid helium target.

The transmission of cold neutrons in a liquid helium target was measured and the scattering cross sections were calculated in two separate studies.[SDG55],[EL57]. The first study by Sommers, Dash and Goldstein in 1954, showed that the total scattering cross section decreased as a function of increasing wavelength and for a given neutron wavelength, decreased as a function of decreasing liquid helium temperature. The total cross section as a function of neutron wavelength and helium temperature is shown in Figure 4.5.

Qualitatively, the cross sections exhibit the same behavior observed for solid targets. Destructive interference from Bragg scattering accounts for the rapid drop in cross section between 3 and 10 angstroms. In the case of a liquid, the Bragg edge is less well defined as there is no ordered lattice spacing, but rather an effective distance from the average over nearest neighbor spacings. The cross section increases for increasing temperatures due to the larger density fluctuations which reduce the destructive interference. It is interesting to note that the cross section does not behave like that of an ideal Boltzmann gas nor that of an ideal Bose-Einstein fluid.

The curves in Figure 4.5 clearly show the advantage of taking data at as low a temperature as is practical to reduce neutron scattering. For 7 Å neutrons, the fractional change in transmission estimated from the data [SDG55] is 1.4×10^{-2} for a 0.1 K change in temperature near 4.2 K. Using liquid helium vapor pressure tables, we calculated the fluctuation in transmission corresponding to changes in pressure assuming an approximate conversion of 80 torr per 0.1 K change in temperature near 4.2 K. [Sco59] We estimated that a fractional change in neutron transmission of 1.7×10^{-4} occurs per 1 torr of pressure change. This implies that overall fluctuations

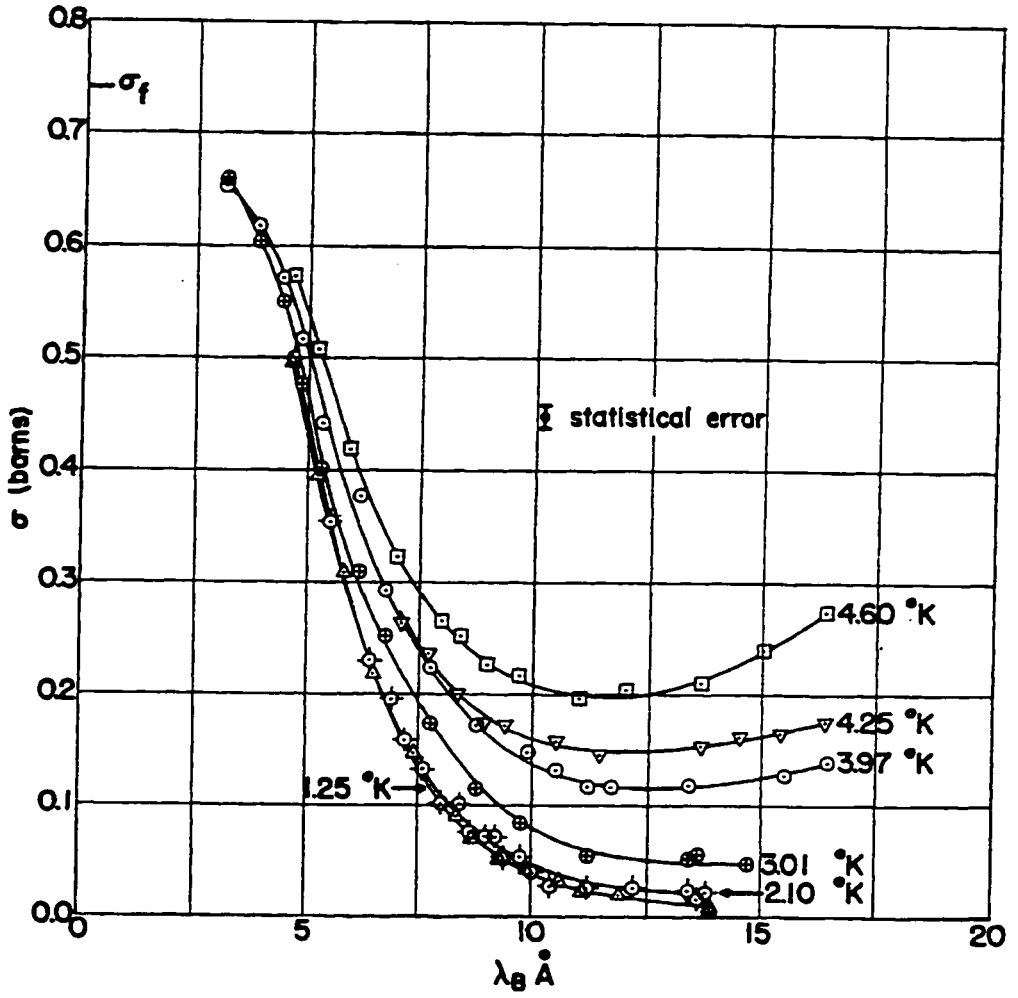

Figure 4.5: Measured neutron scattering cross sections in liquid helium as a function of neutron wavelength and helium temperature.[SDG55]

in pressure on the order of 1 torr over time periods comparable to the flipping rate (approximately 1 second) of the analyzing coil field direction (measurement of N_+ and N_-), will contribute to an asymmetry on the order of 0.2 mrads. Note that this is a factor of 10 less than the background contribution from the magnetic field rotations.

Fluctuations in count-rate resulting from overall temperature changes have the same effect on the measured asymmetries as reactor fluctuations. Uniform temperature changes (as measured by pressure changes in the target region) will affect both beam halves equally, and will be separated in the analysis scheme. Local temperature gradients in which two target chambers differ, front to back or side to side, may contribute to a false asymmetry in count-rate. This same argument applies to local density fluctuations (or bubbles) in the liquid helium. Correlations of local pressure and density gradients with the target positions are target dependent false contributions to the PNC signal. Random fluctuations will contribute to the statistical noise of the PNC signal.

The study on n+^{4}He scattering by Egelstaf and London,[EL57] measured the the small-angle scattering, the back-angle scattering, and the total cross sections for incident reactor neutrons with a beryllium cut off, and mean wavelength of 4.6 Å. The measured total cross section of 0.58 barns agrees with the Sommers, Dash and Goldstein results presented in Figure 4.5. This study showed that the forward scattering at liquid helium temperatures around the transition temperature of 4.2K, is nearly elastic with a differential cross section of approximately 35 mb/steradian. The back-angle scattering is inelastic with an energy loss close to that of the free atom model, and a differential cross section of 35 mb/steradian. The forward angle differential cross section for liquid helium at 4.76K and saturated pressure, ranges from 50 mb/steradian to 100 mb/steradian for scattering angles of 12 to 0 degrees respectively. The scattering in helium gas at 4.2K was measured as 140 mb/steradian in the forward angles (larger than the calculated free atom forward cross section of 93

mb/steradian) and close to the free atom value of 35 mb/steradian in the backward angles.

The results of these studies agree with the liquid helium model developed by Goldstein and Sommers. Scattering from density fluctuations, can reproduce the observed forward scattering cross section behavior. The backward angle cross sections are consistent with a crystal model with phonon excitations.

4.5.3 Target dependent effects

Target dependent rotations, contributions to ϕ_{targ} in Equation 4.16, necessarily alternate in sign with the target state, and therefore will mimic the PNC signal. In our measurement scheme, target-dependent false signals are not separated from the PNC signal. We therefore determine $\varphi_{targ} = \varphi_{PNC} + \varphi_{PCtarg}$ and not φ_{PNC} alone. Since φ_{PCtarg} is a direct contribution to the systematic error, we must reduce this contribution to less than 5×10^{-8}.

The diamagnetism of the liquid helium target is one source of a target-dependent false signal. For a material with zero net angular momentum in an external magnetic field, the electron orbits will change in such a way as to oppose the applied field, as dictated by Lenz' Law. The response to the external field is given by the magnetic susceptibility factor for the medium, which for liquid helium is $\kappa_m = -6 \times 10^{-8}$. Thus, the magnetic field is altered by the induced magnetism, an additive term proportional to the applied field, given by $4\pi M = 4\pi\kappa_m B \sim -10^{-6} B$ when the liquid helium is in the target region. The diamagnetic effect reduces the local field, and therefore the spin precession of the neutron in the target region. We want this effect to cause at most a change in the spin-rotation of 10^{-8} radians integrated over the target length. A magnetic field of 10^{-6} mGauss will rotate 7 Å neutrons a total of 3×10^{-8} radians over 1 meter. Therefore, the diamagnetic contribution will be smaller than our design error as long as the residual field is less than 1 mGauss.

Another target-dependent effect arises because the index of refraction for liquid

helium is different than that for helium gas, which is well approximated by the vacuum index of exactly 1. The index of refraction is equal to the ratio of the particle (or group velocities) inside and outside the medium,

$$\mathsf{n} = \frac{(v_{\text{inside}})}{(v_{\text{outside}})} \tag{4.22}$$

The lower index of refraction of liquid helium as compared to gaseous helium, reduces the velocity of the neutrons in the target. This implies the neutron spends more time in the target region when it contains liquid helium than when it is 'empty' with residual helium gas. This will alter the total rotation angle from spin precession about the axial B field. A maximum axial magnetic field of 0.1 mG will assure that the change in spin-rotation due to the slowing down of the neutrons is less than 2×10^{-8} radians, a factor of 3 below the desired systematic limit. This target-dependent effect produces the most stringent criterion for the axial magnetic fields.

Fortunately, these two effects (reduction of the index of refraction and the diamagnetic reduction of the local magnetic field), have opposite consequences. The slowing down of the neutrons increases the magnetic field induced rotation while the diamagnetic effect decreases the magnetic field producing the precession. The slowing down of the neutrons is a larger effect by a factor of about 4, so the cancelation is not complete, and it is worthwhile to minimize both effects.

The critical angle for reflection (θ_c = the maximum angle at which an incident neutron will totally reflect from a given surface) depends upon the change in index of refraction at the surface.

$$1 - \mathsf{n} = \frac{\theta_c^2}{2} \qquad \text{where} \qquad \theta_c = \frac{V_{eff}}{E} = \lambda\sqrt{\frac{\rho a}{\pi}} \tag{4.23}$$

where, V_{eff} is the effective Fermi potential of the surface, E and λ are the energy and wavelength of the incident neutron, ρ is the material density and a is the coherent scattering length. The index of refraction is dependent upon both media at the reflection surface. Hence, the critical angle for reflection at the aluminum target

walls will be different for liquid helium in the target region compared to that for helium gas when the target is considered empty.

The effective potential of the surface and therefore the index of refraction is reduced when the initial medium is not a vacuum (when $n \neq 1$).

$$n_{21} = \frac{n_2}{n_1} \approx 1 - \frac{1}{2}\left(\frac{V_{eff2} - V_{eff1}}{E}\right)^2 = 1 - \frac{(\theta_c')^2}{2} \tag{4.24}$$

In the case of liquid helium, the critical angle is reduced by a factor of 17% compared to the empty case with saturated helium gas. Therefore, more divergent neutrons will pass through the empty target chamber than through the filled target, and the beam profile becomes target dependent.

4.5.4 Monte Carlo simulation of the apparatus

We performed a calculation to investigate the effects of changing target chamber contents (liquid or gaseous helium) on the neutron count-rate at the detector. The cross section information discussed in Section 4.5.2, was used in a Monte Carlo particle tracking calculation to simulate the two-target system in the experimental set-up. The neutron spectrum with a beryllium cut-off used in the Egelstaf and London measurements is similar to our beam spectrum and these results were applied in the calculation. The neutron scattering in liquid helium was assumed to be isotropic in the lab frame, a reasonable simplification in that both the forward scattering and the backward scattering were 35 mb for temperatures near the boiling point of the helium. Assuming isotropic scattering, the calculated total cross section of about 0.4 barns is close to the total cross section found in Figure 4.5 (about 0.5 b). We assumed multiple scattering was negligible, in agreement with Goldstein and Summers [GS56].

The interaction of the neutrons with the wall surfaces was included. The critical angle for a Pyrex to air interface (1.1 mrads/Å) was used for the guide tubes, and the critical angle for an aluminum to air interface (0.81 mrads/Å) was used for the

empty target chambers. The reduced critical angle (0.67 mrads/Å) was used in the target chamber containing liquid helium.

The transmission of neutrons through the system with no liquid helium in the target chambers was calculated as about 40%. The number of neutrons lost to scattering was determined and the fraction of the scattered neutrons that are detected was calculated to be less than 1×10^{-3}. With a 100 μGauss axial magnetic field producing a rotation of about 2 mrads, this gives a maximum possible contribution to φ_{PCtarg} of 2×10^{-6}, which is relatively large.

The calculation showed a difference in the number of scattered neutrons detected for the two target states. More scattered neutrons are detected for the target state in which the liquid helium is in the rear target chamber. This difference is at most 3×10^{-4}. Seeing more scattered neutrons reach the detector for the back target position is reasonable considering that the solid angle acceptance of the detector is greater for this downstream target position compared to the front position. The difference in solid angle can account for the difference in detected scattered neutrons.

To reduce the number of scattered neutrons that are detected, we placed collimators in the target chamber regions, (Section 5.3) and placed an additional collimator at the end of the exiting guide tube, before the detector (Section 5.5.3). While the increased collimation and the use of absorptive walls decreased the count-rate, and therefore increased the statistical uncertainty, we obtained a cleaner signal and greatly reduced the systematic error associated with scattering in the target.

Chapter 5

APPARATUS

In Chapter 4, we reviewed the basic design of the experiment and discussed the requirements for achieving the desired systematic limit of 5×10^{-8} radians. In this chapter, we describe the apparatus and review the performance of the individual components.

A schematic representation of the apparatus is given in Figure 5.1. Neutrons were transversely polarized in a supermirror, and traveled through a long guide tube to the apparatus. The neutrons passed into the low magnetic field region through the input coil, which preserved the neutron spin polarization along the vertical direction. The PNC $n + \alpha$ interaction rotated the neutron spins as they traversed the target region contained within the low field region. The neutrons left the target region through the output coil which preserved the horizontal component of the spin, and then entered the supermirror analyzer. A detector just behind the analyzer measured the neutron count-rate which was proportional to the angle of spin rotation.

5.1 Cold neutron beam

The Cold Neutron Research Facility (CNRF) at the National Institute of Standards and Technology (NIST), in Gaithersburg, Maryland, consists of a 20 MW research reactor with a liquid para-hydrogen cold source producing neutrons with energies in the 10^{-3} eV range. Neutrons from the cold source travel through reflective guides coated with ^{58}Ni (critical angle of 2.1 mrads/Å) to the Fundamental Physics beam line, designated NG-6. During our data runs, we placed two types of liquid nitrogen

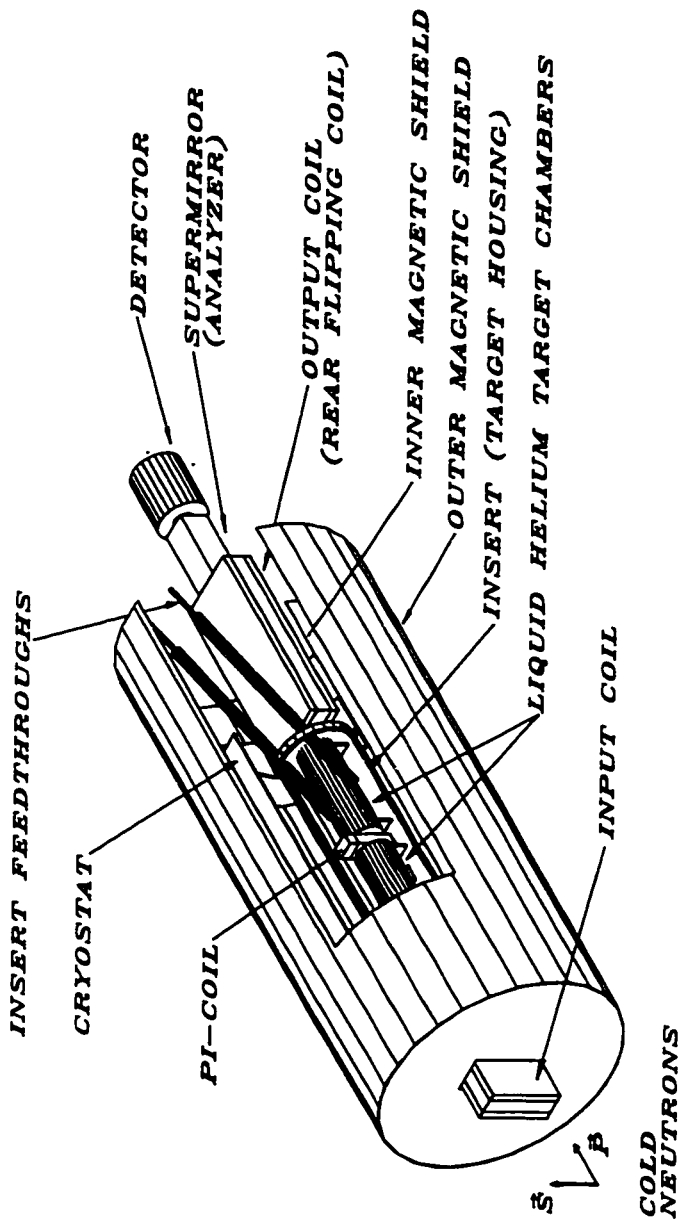

Figure 5.1: Schematic diagram of the spin-rotation apparatus.

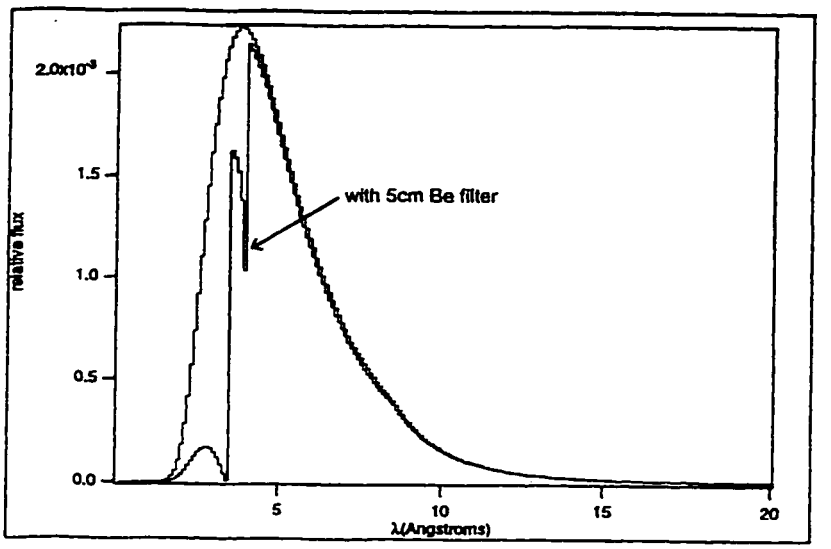

Figure 5.2: Expected NG-6 beam line spectrum exiting the polarizing supermirror. This calculated spectrum includes 20 cm each of bismuth and beryllium filters.[Wie96]

cooled crystal filters in the beam line. Four polycrystalline beryllium sections of 2 inches each provided a high energy cut off at a wavelength of 3.96 Å. For 20 cm of polycrystalline beryllium, there is essentially no transmission of neutrons with wavelengths less than 3.4Å, approximately 4% transmission of neutrons with wavelengths between 3.4 and 3.9Å, and a transmission of about 90% for neutrons with wavelengths greater than 3.9Å. [de 84]

Two single-crystal bismuth sections of 2 inches each, filtered gamma-rays to reduce radiation exposure. The loss of beam from these filters was about 19%. With a calibrated fission chamber detector, Wietfeldt *et al.* measured the capture flux (effective thermal neutron flux) exiting the filter cryostat as 8.5×10^8 neutrons/sec/cm^2.[WN96]

The neutron energy spectrum was approximately a Maxwell-Boltzmann distribution at 35 degrees Kelvin, multiplied by a wavelength-dependent factor (proportional to λ^2) to model the acceptance of the reflective guides. A calculated energy spec-

trum for the NG-6 line is presented in Figure 5.2.[Wie96] This spectrum includes the calculated losses from the bismuth and beryllium filters, and from the polarizing supermirror (see Section 5.2) located immediately downstream of the filter-cryostat are included in the calculated spectrum. The expected beam spectrum peaks at approximately 5Å, and drops by an order of magnitude at 12Å.

After the supermirror, the neutrons traveled through an 8 ft section of guide tube. The guide tube contained four, 4 ft sections of rectangular borosilicate glass tubes. The two pairs, placed side-by-side, produced split 2.1 cm (horizontal) x 4.4 cm (vertical) beams with a 0.8 cm separation. A collimator on the downstream face of the guide tube limited the diverging beam to 2.2 cm x 4.2 cm with a 0.8 cm center septum. To improve the neutron transmission, we filled the guides with helium gas and maintained a small positive pressure with a constant, slow flow through the glass tubes.

The critical angle for glass is 1.1 mrads/Å and dominates the horizontal divergence of the beam exiting the guide tube. For an 8 foot path, neutrons with a divergence greater than 9 mrads necessarily made at least one reflection on the absorptive surface of the guide tube.

5.2 Supermirror polarizer and analyzer

Neutrons are polarized through spin-dependent scattering from magnetized mirrors. The magnetic contribution to the index of refraction is directly proportional to the local magnetization of the material. Equation 3.12 becomes [HPW78]

$$n = 1 - \left(\frac{2\pi\rho\hbar^2 a}{p^2} \pm \frac{\mu(B-H)m}{p^2} \right) \equiv 1 - \frac{\theta_{c\pm}^2}{2} \tag{5.1}$$

where p, μ, and m, are the momentum, magnetic moment and mass of the neutron, ρ, a, and B are the nuclear density, average bound coherent scattering amplitude and magnetic induction of the magnetic material, and H is the applied field in the plane of the reflecting surface. The positive (negative) sign refers to the neutron

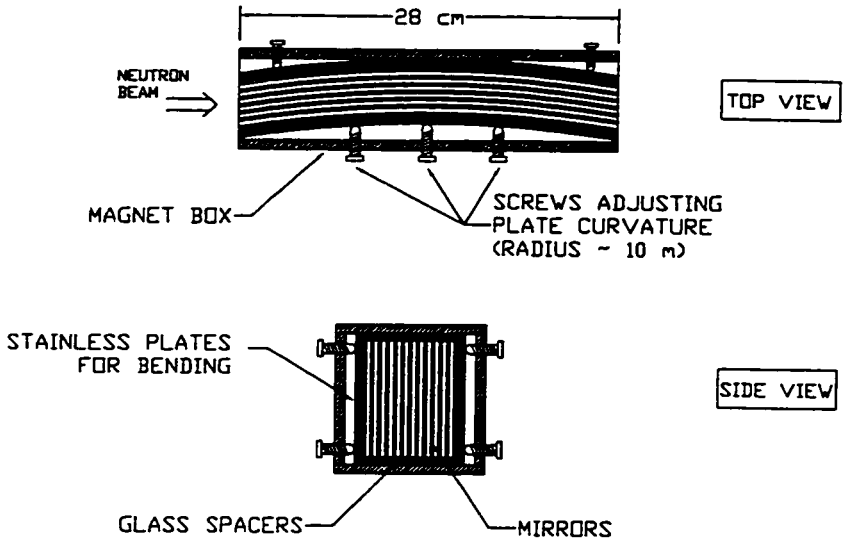

Figure 5.3: Top view and side view drawings of a supermirror polarizer. Adapted from [Sch89].

magnetic moment, μ, being parallel (antiparallel) to the magnetization, $(\vec{B} - \vec{H})$, of the reflecting medium. We define in Equation 5.1, an effective critical glancing angle, $\theta^2_{c\pm}$, the maximum incident angle at which neutrons of the given spin state, $(\pm)$, will reflect from the surface.

The neutron supermirror polarizer is based on the multilayered Soller or "beam bender" design in which plates consisting of thin-film polarizing material laid on an absorptive substrate are stacked and bent into a large radius of curvature. A schematic diagram of the supermirror is given in Figure 5.2. The materials and thicknesses are chosen so that one spin state is preferentially reflected by the mirror surface (θ_c is large) while the other is transmitted (θ_c nearly zero) and absorbed in the underlying layers. The radius of curvature and plate spacing are chosen so that the neutrons must undergo at least one interaction with the ferromagnetic substance comprising the mirror surface. Typical polarizations for these supermirrors are 98%.[Sch89]

The NIST supermirrors (polarizer and analyzer) were fabricated at the Institut Laue Langevin in Grenoble, France. These were constructed of Pyrex glass plates coated with alternating layers of titanium (used for matching the neutron index of refraction for the minus spin state) and gadolinium (the absorptive layer) with a top layer of cobalt (the magnetic mirror surface). The plates were placed with 1 mm separation in a saturating magnetic field using a 300 Gauss permanent magnet box, and were pressed to a radius of curvature of about 10 m. For a plate length of 28 cm, this gives a geometric deflection angle of 28 mrads, or 1.6°. This defines the beam axis downstream of the supermirror.

Specifically, the supermirror polarizer was constructed from 45 plates and transmitted a 4.5 cm (vertical) by 5.5 cm (horizontal) beam defined by the B_4C windows. Both sides of all the plates were coated as described above. The analyzer contained 55 plates, had thin aluminum windows of dimensions 4.5 cm by 6 cm, and only the central plates were coated on both sides, with the outer plates coated on one side. Both supermirrors were designed with the magnetic field in the vertical direction, and passed neutrons with the "up" spin state along this field direction.

Previous to our data run, Wietfeldt *et al.* measured the polarization and transmission of the supermirror polarizer and analyzer pair. They placed a magnetic field coil spin-flipper between the two supermirrors and measured the neutron transmission asymmetry of the two spin-flip states of the coil.[WN96] They extracted a polarization product of 88% for the two supermirrors and calculated a polarization factor of (96±2)% for each supermirror. In addition, they measured the transmission through the polarizing supermirror as 24%.

The analyzer was aligned on the beam line by determining the maximum beam transmission as a function of angular position about its central vertical axis.

5.3 Liquid Helium Target

The target region consisted of two target chambers separated by the π-coil (see Section 5.4) that were housed in the cylindrical "insert". The insert formed a vacuum tight region that isolated the target system from the surrounding cryostat, described in Section 5.6. A schematic diagram of the target system is given in Figure 5.4. A pump and drain system filled and emptied the target chambers from a liquid helium reservoir contained within the insert and below the beam height. This filling system is described in Section 5.3.2. Two feedthrough tubes extended from the downstream end of the chamber, providing external access to the insert for liquid helium transfer and control of the target fill system.

We monitored the liquid helium level in the insert reservoir and in the target chambers using resistive wire level sensors manufactured by Lakeshore Cryotronics. The sensors require an activation current of 70 mA, which generated undesired magnetic field gradients in the target chambers. For this reason, the level sensors remained inactive during data collection times.

We reduced liquid helium loss by isolating the fixed volume region that defines the insert. The temperature and therefore the pressure within the insert varied slowly over time. A baratron located at room temperature on one of the feedthrough tubes, continuously monitored the insert pressure. We mounted two pressure relief valves on the insert volume, one on each feedthrough. One relief valve was set to release at about 900 torr and could be closed off with a ball valve. The other relief valve was set at 1000 torr, defining the maximum allowable pressure in the insert. In addition, we used a one-way valve that released at a pressure of 2 torr over atmosphere, for exhausting during liquid helium fills. During data acquisition, the exhaust valve was isolated from the insert with a ball valve.

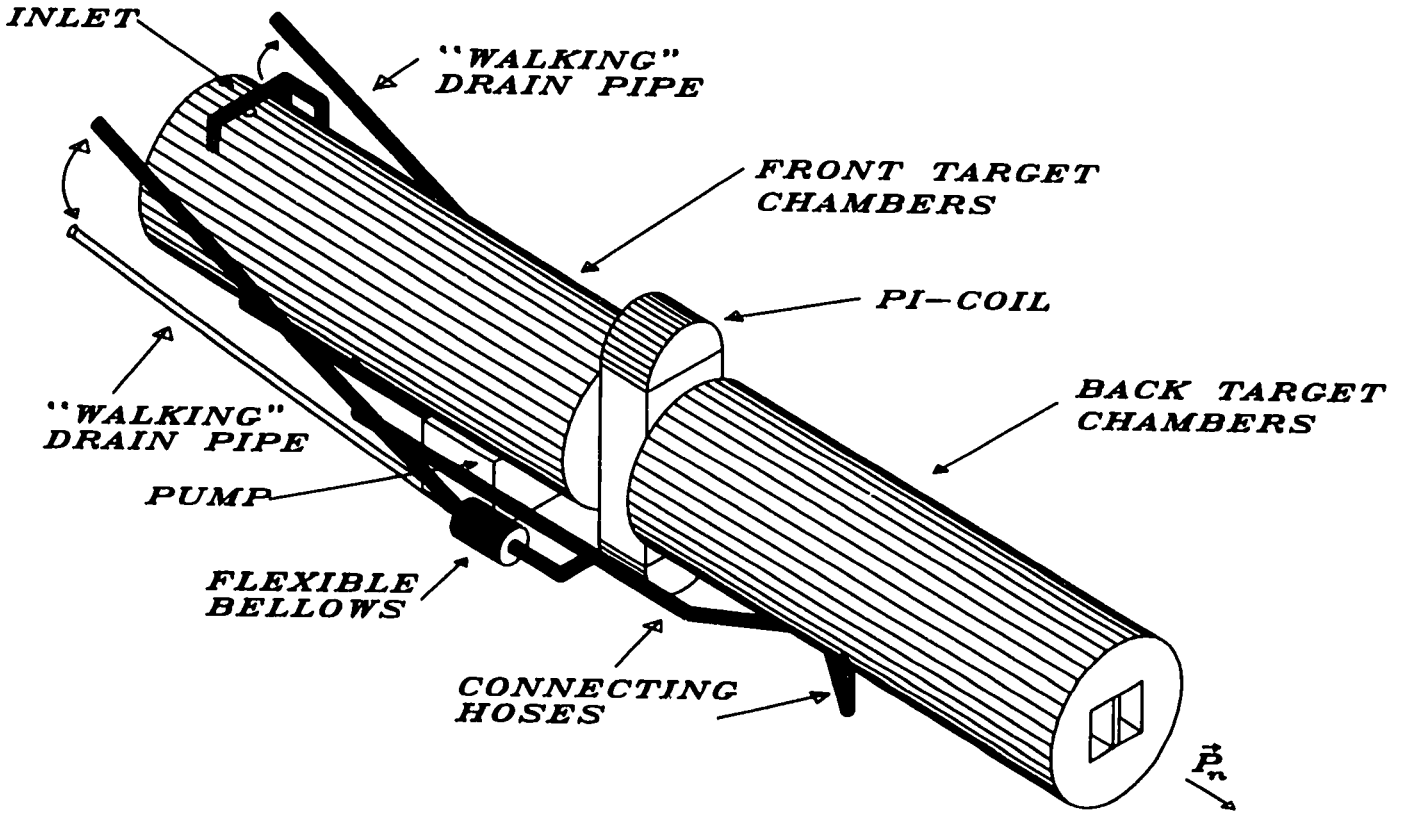

Figure 5.4: Schematic diagram of the target housing. The π-coil target chambers, and liquid helium pump and drain system are shown.

5.3.1 Target chambers

We constructed the liquid helium target chambers from aluminum, a non-magnetic material with a high thermal conductivity. A 0.125 inch (3.2 mm) septum divides the target region into two side-by-side, isolated chambers. Vacuum tests on the target chambers confirmed the isolation of the two half-regions. The liquid helium target volume was 45.7 cm (18 inches) in length, 7 cm in height and 3 cm in width.

A ^{6}LiF collimator located on the outer surface of the upstream face of the insert, defined two beams 4.2 cm high by 1.9 cm wide separated by 1.2 cm. The collimated beam separation was much larger than the target separation to reduce the number of neutrons that could hit the center septum. To reduce further scattering off the center aluminum septum, we placed three collimators inside the target chambers, limiting the two beams to cross sectional area of 4.3 cm in height and 2.1 cm wide, with a 1 cm separation. Neutrons that would otherwise hit the septum wall were either absorbed on the collimators, or their divergence angle was so large that they could not reach the detector.

The target window material must have small neutron absorption and scattering cross sections, and be strong enough not to flex or change shape depending on whether the gas or liquid is in the chamber. A flex of the target window producing a difference in neutron path length on the order of 5 microns will introduce a target dependent change in the spin-rotation of up to 10^{-8} radians assuming a 100 μGauss field. We chose 0.1 mm thick foils made of an alloy of aluminum (97%) and magnesium (3%) for the target and insert windows. The window foil is sandwiched between the target chamber face and a mask that secured the foil to the chamber end face and provided support to prevent flexing. We pressure tested the Al97/Mg3 material at liquid nitrogen temperatures. The windows withstood 3 atm pressure (well above operating pressures) before breaking or bursting.

For radiation safety, ^{6}LiF polymer sheet lined the inner surface of the target

chambers to reduce γ-ray production from neutron absorption on aluminum. These absorbing sheets were located on the target walls, outside the beam dimensions.

5.3.2 Pump and drain system

The centrifugal pump creates a pressure difference between the inlet located below the central axis of the rotor and the outlet located on one of the side walls. The liquid helium moves through the pump located below the targets in the reservoir, and through latex tubing connecting the pump outlet to openings on the top of the two front target chambers. Latex tubing on the underside of the targets connects each of the front target chambers with the respective back chamber on the other beam side. Therefore, the target chambers are filled in the desired diagonal pattern as discussed in Section 4.2.

The drive train connects the pump located in the liquid helium reservoir to the stepping motor located outside the insert at room temperature, and beyond the low magnetic field region. We set the stepping motor to run at 3 Hz, so that the pump, with a 6 to 1 gearing ratio, rotated at 18 Hz. The primary pump and gear-box materials were aluminum and Teflon, with small parts made of Del rin and brass. All magnetic materials associated with operating the pump, were located outside of the inner magnetic shield layer. The pump remained idle during data acquisition.

As seen in Figure 5.4, for each target set, a thin-walled copper tube left open at one end is connected via a bellows and latex tubing to a target drain port. These tubes serve as valves which when in the up position, allow the target chambers to fill with liquid helium and when in the lowered position enable the targets to drain.

We externally positioned the "walking pipes" with the use of nylon strings attached to the copper tube and passed through the insert liquid helium transfer line feedthrough. At the room temperature end, two computer controlled pneumatic pistons pulled nylon strings to raise and lower the drain pipes. Each piston was associated with the filling and draining of one set of target chambers.

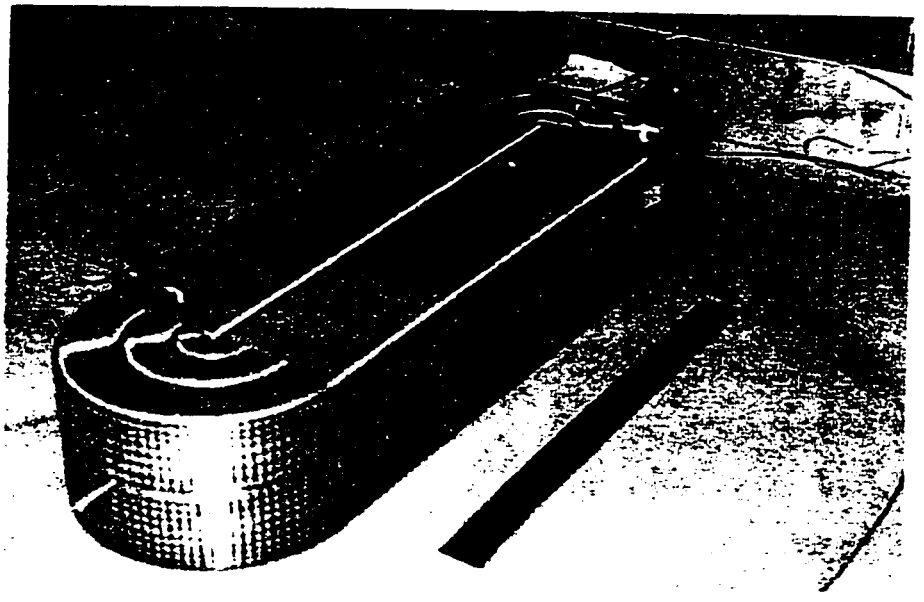

Figure 5.5: The photo shows the π-coil laying on a work-bench. The ruler in the picture is 6 inches in length. The positioning pin can be seen in the lower left corner.

Tests of the fill and drain system showed that the target chambers were leak-tight on a time scale of about 1 hour, which is sufficiently long compared to the data acquisition time scale of 10 minutes or less for any given target position. The pump filled the target chambers in about 30 seconds. The drain time, however, was about 2 minutes. These times varied, depending upon the reservoir level.

5.4 π-coil

A photo of the π-coil is given in Figure 5.4. The π-coil consisted of two side-by-side rectangular coils, 16 cm high and 4 cm wide. The two solenoid coils (each associated with one side of the experiment) carried equal currents in opposite directions, producing equal and opposite vertical magnetic fields in the two halves of the beam. Each

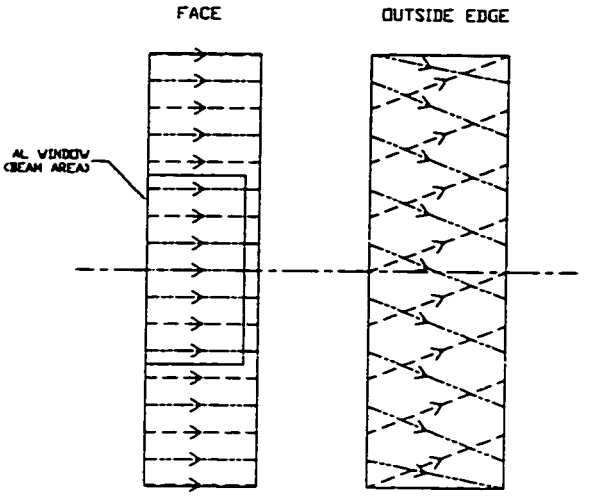

Figure 5.6: Winding scheme of the π-coil. The figure illustrates the wire wrap for one solenoid cylinder and the resulting overlap pattern. As discussed in the text, half the wires are wrapped down the coil and the other half progress up the coil. For clarity, a winding density of 1 wire per cm is shown. The arrows indicate the winding (current) direction.

solenoid serves as a return coil for the magnetic flux of the other coil. Half-toroid coils located above and below the cylinders, assist the return flux of the solenoid fields.

To capture all the flux exiting the top of the cylinder (intersection of the cylinder and the toroid) an infinite number of toroidal coils would be needed to match the $\frac{1}{r}$ radial dependence of the magnetic field in the toroid to the uniform field of the cylinder. However, practical constraints limited the number of return coils we used. We studied the leakage fields and internal field homogeneities caused by the field mismatch at the intersection of the solenoids and various numbers of toroids. From the calculations, we determined the minimum number of toroidal coils that could return the solenoid magnetic flux and preserve the homogeneity of the vertical fields to one part in 10^4. We chose three nested toroid coils with effective radii of 0.89, 1.65, and 3.02 cm.

We designed the coil for 10 Gauss-cm, the product of the magnetic field and the neutron path length in the coil, so that the spin of a neutron traveling with a velocity of about 600 m/sec (6.6 Å) will precess a total of π radians over the path of the coil. This criterion imposed a field of about 2 Gauss for a π-coil depth of 5 cm along the beam axis. We wrapped the aluminum π-coil form with 28 gauge, polyurethane coated, copper magnet wire, with a winding density of 10 wires per cm in the solenoid region. Since the copper wire has essentially no resistance at 4 K, the π-coil introduces a negligible amount of heat into the target chamber.

We put 28, 52, and 98 wraps on the inner, middle and outer toroidal coils respectively, to provide the optimized toroidal fields determined from calculations. Thin aluminum plates support the windings in the beam area, with a region in-between that is able to exchange gas with the insert environment. Therefore, when in place, the beam region consists mostly of He gas. In this configuration, a π-coil current of 155 mA rotates an off-axis spin component of 7 Å neutrons 180 degrees about the $\hat{z}$ axis.

We minimized possible field imperfections by constructing the aluminum cores with grooves to position the wire. The aluminum was anodized and the corners were slightly rounded to lessen the possibility of shorting the wires to the core. We separately wound the cylindrical and toroidal coils, and then soldered the ends. All single wires were twisted with another wire carrying current in the opposite direction to minimize current loops and stray magnetic fields.

The helical pitch of a real, continuously wire-wrapped finite solenoid coil causes deviations from an ideal, homogeneous axial field inside. We wrapped the coil with three sides straight across and the fourth side connected one loop to the next, thereby taking all of the pitch angle. To lessen the effect of the pitch on one side of the solenoid, every other loop of the solenoid coil was wrapped progressively down the coil, and then the skipped loops were then wrapped with windings progressing back up the coil. The overlap of wires were placed on the outer edge of the solenoids,

farthest away from the neutron beam area. The resulting winding pattern can be seen in Figure 5.4.Where the wires overlap, the two currents sum to nearly cancel the effective axial current. With the overlap, one wire necessarily must be at a radius slightly greater than the other, causing residual deviations from field homogeneity.

We measured the leakage fields surrounding the π-coil as a function of distance along the beam axis. To increase the sensitivity of the measurements, we placed the π-coil within the magnetic shields and used a current of 250 mA producing a calculated vertical field of 3 Gauss inside the solenoids. Figure 5.7 diagrams the positions where the leakage fields were measured and the results are presented in Table 5.1. The leakage fields in the beam area were less than 120 μGauss a half-inch from the wires. Note that the liquid helium target was located 1.32 cm (about 0.5 in) away from the π-coil. The only large field was in the $\hat{y}$ direction (parallel to the wires) on one side of the π-coil. The rest of the fields measured less than 70 μGauss. Since we ran the π-coil at 170 mA or less during data acquisition, the criterion of magnetic fields less than 100 μGauss was well satisfied by the π-coil leakage fields. The field in the target region (up to 2 inches away from the π-coil) induced by the π-coil was about 30 μGauss for a 250 mA current.

With the π-coil current set at the nominal operating value of 156 mA, 5 Å neutrons rotate 127 degrees, while 10 Å neutrons precess by an angle of 253 degrees. This spread of precession angles in the π-coil causes the magnitude of the transverse spin component (the $\hat{y}$ direction) to be on average about half the value before entering the π-coil. We measure this energy averaged spread in the transverse spin component of the neutrons as a reduction of the polarization product when the π-coil is on compared to when it is off. (The measurement of the polarization product is discussed in Section 6.2.)

Table 5.1: Leakage fields of the π-coil. Data were taken with a π-coil current of 250mA, which is greater than the settings during data acquisition. The positions used in this field map are diagramed in Figure 5.7. All magnetic fields are given in units of μGauss.

Upstream Face										
		LOWER			CENTER			UPPER		
Position	d_z	B_x	B_y	B_z	B_x	B_y	B_z	B_x	B_y	B_z
SIDE 1	0	5	-82.5	-2.5	10	-65	5	15	-40	2.5
	1	5	-37.5	- 5	5	-30	2.5	10	-17	-7.5
	2	5	-15	-5	7.5	-12	7.5	5	7.5	10
MIDDLE	0	12.5	45	-25	20	25	2.5	25	15	-2.5
	1	7.5	27	-5	10	-18	-2.5	12.5	10	5
	2	10	15	0	5	-10	5	7.5	7.5	7.5
SIDE 2	0	20	-12.50	30	27.5	5	-22.5	17.5	20	2.5
	1	12.5	-12.5	10	17.5	-7.5	-5	12.5	2.5	2.5
	2	5	-10	0	7.5	-10	2.5	5	5	5

Downstream Face										
		LOWER			CENTER			UPPER		
Position	d_z	B_x	B_y	B_z	B_x	B_y	B_z	B_x	B_y	B_z
SIDE 1	0	25	-150	50	20	-110	22.5	2.5	-150	17.5
	1	7.5	-73	32	7.5	-52	25	2.5	-73	22.5
	2	5	-40	23	2.5	-23	20	2.5	-40	17.5
MIDDLE	0	-2.5	-65	85	33	-60	55	25	-65	33
	1	+13	-43	55	10	-33	35	10	-43	25
	2	7.5	-25	27	5	-15	22	7.5	-25	20
SIDE 2	0	25	37	95	47	0	-65	38	25	35
	1	10	15	50	20	-5	-40	17	10	25
	2	5	10	30	10	-5	-25	10	5	20

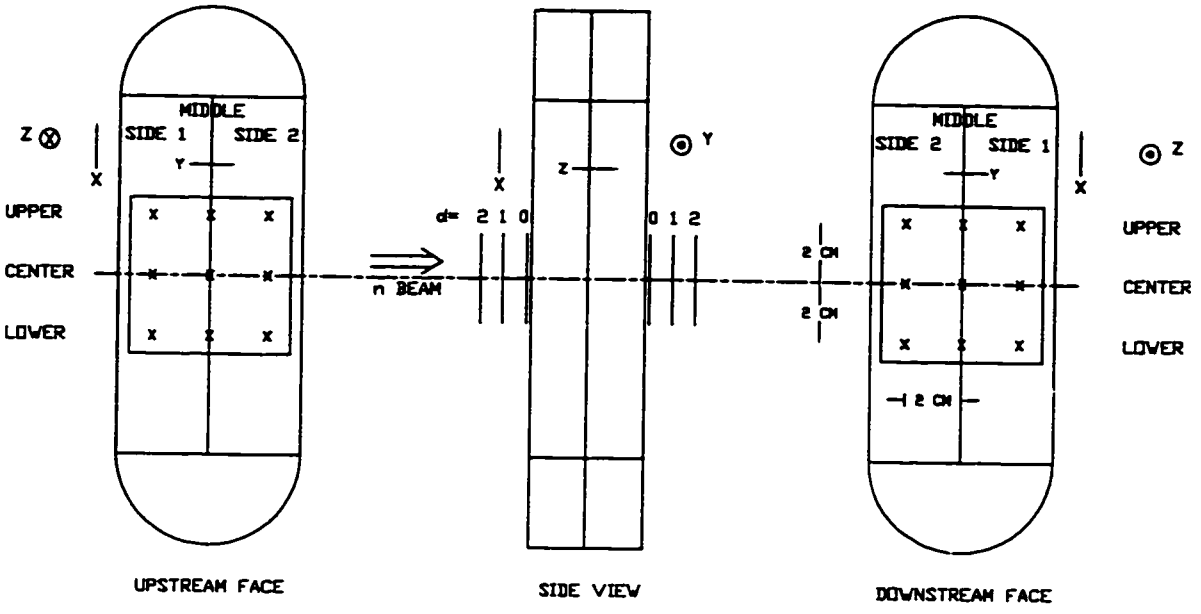

Figure 5.7: Field measurement positions used to study the leakage fields of the π-coil. See Table 5.1.

5.5 Magnetic field coils

The input and output coils preserved the vertical alignment of the neutron spin up-stream of the target region and the horizontal component of the spin down-stream of the target region. Maintaining the neutron spin alignment was especially critical when the neutrons passed between two regions of differing magnetic field strength.

5.5.1 Front end coils: Guide Coil and Input coil

The initial guide tube coil maintained the vertical spin polarization as the neutrons exited the large magnetic field region of the supermirror, and traversed the 8 foot flight tube. The 300 Gauss field in the supermirror box falls off as $\frac{1}{e}$ in the beam direction. We placed the two halves of a 20 wire Helmholtz coil above and below the guide tube. With a current of 4.2 amps, this guide tube coil produced a 5 Gauss vertical field. The guide coil simply prevented the spins from precessing about the

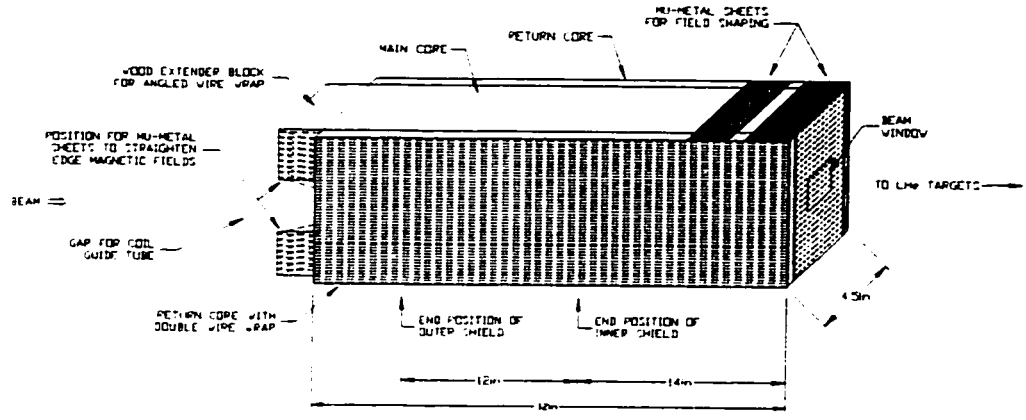

Figure 5.8: Diagram of the input coil.

unknown ambient fields along the flight-path, and therefore, the field alignment was not critical. The strength of the coil was determined from field matching with the input coil.

We positioned the input coil between the guide tube located outside the magnetic shields and the cryostat housing the targets inside the field-free region. The neutrons adiabatically precessed about the imperfectly aligned guide coil magnetic fields, until they entered the input coil. Once inside the input coil, the neutron spins precessed about a progressively better aligned vertical field. When the neutrons reach the other end of the input coil, the spins were aligned with a homogeneous vertical field and passed non-adiabatically into the field free region.

The input coil is shown in Figure 5.8. It consisted of windings on a 32 inch long main core, and two return cores located one on each side. The cores were made of non-magnetic G-10 circuit board material. The opening at one end of the main core allows the beam tube to pass through. At the other end, the beam passes non-

adiabatically through a current sheet of 18 gauge, 40 mil (1 mm) diameter aluminum wire. Copper wire was used for areas outside of the beam dimensions. The wires were tightly wrapped and glued in place to minimize imperfections in the windings, protect the wires and preserve their position during handling.

The width of the return cores were $\frac{1}{4}$ that of the main core necessitating two sets of windings on each to return half of the main core magnetic field flux. To assist the return flux, and therefore improve homogeneity within the beam path region of the main core, μ-metal sheets were placed at the top and bottom of the coil across the main core and return cores, as shown in Figure 5.8. These μ-metal pieces could be degaussed while the coil was in position on the beam line.

The input coil current was set to 0.5 amps, to produce a flat field of approximately 5 Gauss inside. We empirically matched the field of the guide coil to that of the input coil. The wires of the front guide coil were bent at the input coil end in approximately a 45° angle to counteract the fringing fields of the open end of the input coil. In addition, μ-metal shims were added above and below the guide tube at the open end of the input coil to help straighten the fields.

As discussed in Section 4.5.3, the dipole fringing fields from the input coil must be minimized in the target region, and satisfy the maximum axial field limit of 100 μGauss. We compared the input coil leakage fields in the beam area just outside of the current sheet for the case of no μ-metal and with μ-metal pieces placed with various gap distances between them and the coil form. For the case with the μ-metal pieces placed in their final configuration (0.03 inch gap), we measured a reduction in the overall leakage fields by a factor of 4 to 5 compared to no μ-metal at all.

The leakage field measurements of the input coil in position within the shields is presented in Figure 5.9. The target chambers begin about 2 inches away from the coil end.

We positioned the input coil on a table that enabled the coil to rotate about the beam axis for alignment with the vertical field of the π-coil. (See Section 6.2.) The

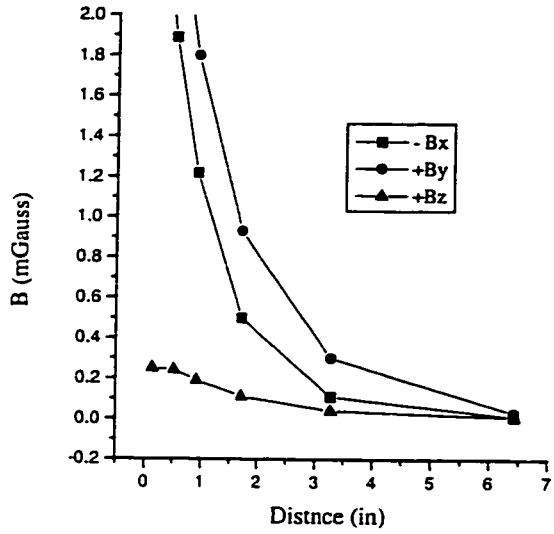

Figure 5.9: Magnetic field measurements outside of the input coil. The axial field, B_z, drops below 1 μGauss by a distance of 2 inches from the current sheet wires.

rotated position of the input coil was determined by the setting of a micrometer that measured the horizontal displacement of the coil centerline. The angle of rotation is the arc tangent of the micrometer distance over the lever arm distance of 7.62 inches. The coil rotation angle was constrained by space limitations from the opening in the inner and outer magnetic shields.

5.5.2 Output coils: adiabatic rotator and flipping coil

We positioned the output coil between the down-stream end of the field free target region and the analyzer. The output coil served the same function as the input coil though in the reverse order: the neutron spins non-adiabatically passed from the field free region into the homogeneous fields aligned in the $\hat{y}$ direction of the coil. This preserved the transverse component of the neutron spin in the transition from the target region. Recall that the transverse component carries the information on the

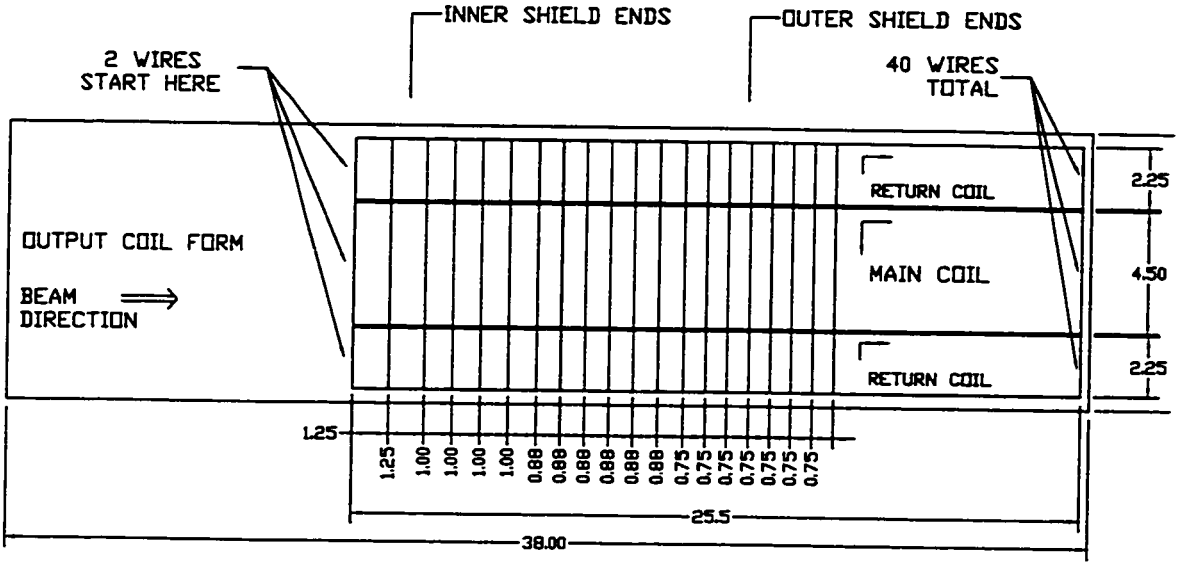

Figure 5.10: Diagram of the output adiabatic coil windings. All dimensions are in inches.

neutron spin-rotation angle.

The rear flipping coil was similar in form and construction to the input coil, with a main core of length 38 inches. The wire wrapping scheme and the positioning of μ-metal shims was the same for both the output and input coils. The output coil was positioned on the holding tray with its axis in the $\hat{y}$ direction.

We examined the transients and residual ringing in the flipping output coil circuit after switching the current between plus and minus values. With the addition of a 4 μF capacitor in series with the output coil resistance, the transients died away in approximately 1 msec.

We performed field maps on the output coil to check the leakage fields in the target region. The fields inside the cryostat were measured with the output coil in position on the tray holder. The measured leakage fields are presented in Figure 5.11.

The output coil preserved the transverse component of the spin, but the analyzer, however, was aligned in the vertical direction. An adiabatic rotator coil gradually

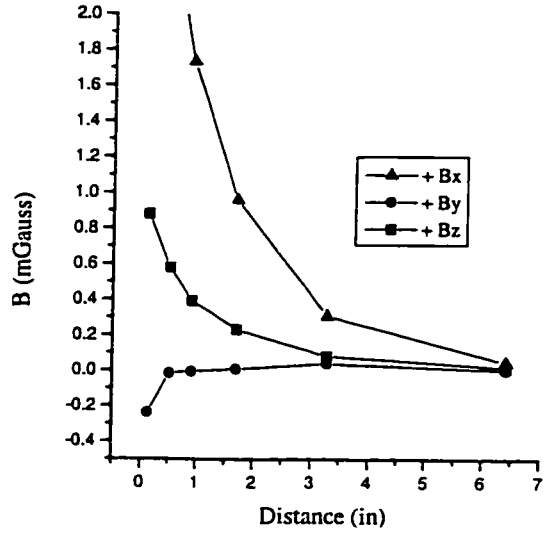

Figure 5.11: Magnetic field measurements outside of the output coil in the target region. The axial field, B_z, drops below 1 μGauss by a distance of 2 inches from the current sheet wires.

rotated the magnetic field from the $\hat{y}$ direction of the flipping coil to the vertical ($\hat{x}$) direction of the analyzer. As the flipping coil fields fall off, the field in the vertical direction increased so that the spins adiabatically rotated approximately 90 degrees. A transverse spin component parallel to the direction of the flipping coil then became field aligned with the analyzer ($+\hat{x}$), while the transverse spin components antiparallel to the flipping field became anti-aligned with the analyzer ($-\hat{x}$).

The static adiabatic rotator coil has an increasing field in the $\hat{x}$ direction. This was achieved by increasing the wire density as a function of z along the beam direction. As shown in Figure 5.10, the coil windings started where the inner shield ends and increased to a total of 40 windings at the end of the output coil. This coil was epoxied onto the flipping coil, so that the two fields were mutually perpendicular, independent of coil rotation position.

The magnetic field variation along the beam path must be small enough not to

depolarize the neutron spin. We require the depolarization to be less than 10^{-4}. In Appendix A, we present the magnetic field requirements to satisfy the adiabatic condition and the maximum allowable depolarization. We put 3.85 amps into the coil to produce a maximum field of about 6 Gauss that matched the residual vertical fields from the analyzer magnet. The measured fields in the $\hat{x}$ and $\hat{y}$ direction as a function of position along the $\hat{z}$ (beam) direction, are given in Figure 5.12. Note that the vertical field increases slowly in the region of constant horizontal field.

At the exit of the output coil, the analyzing magnet fields dominate. We positioned stainless steel plates above and below the analyzer magnet box for field matching between the analyzer field and the end of the output coil. These plate shims straightened the fields in the region at the open end of the output coil and where the output coil guide tube extends out beyond the magnet coil. The field shaping also decreased the rate of change of the vertical field in the region of decreasing horizontal field.

5.5.3 Coil guide tubes

The Pyrex guide tubes within the input and the output coils were oversized (6 cm x 6 cm) to allow the tube to rotate with the coil and not cut off the beam. Using the oversized coil tubes also eliminated stringent requirements for the horizontal and vertical alignment of the input and output coils. Four collimators of LiF plastic are located along the tube and leave an opening of 5.2 cm in height and 5.6 cm in width. Each of these tubes contained a glass septum to maintain beam separation. The 0.069 inch thick glass septum was covered with Li loaded epoxy to reduce scattering.

We placed a clean-up collimator of dimensions 2.25 cm by 4.2 cm, with a 0.8 cm septum separation, at the end of the output guide tube. The vertical dimension was the same as that for the target collimators while the horizontal dimension is larger, to take advantage of the wider acceptance of the analyzer (width of 6.0 cm). This removed scattered neutrons that passed through the oversized output guide tube while keeping those neutrons which spread with the divergence of the beam.

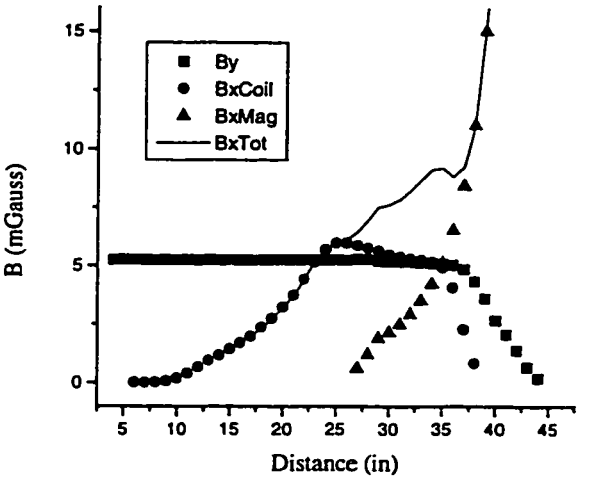

Figure 5.12: Magnetic fields inside the output coil, and extending beyond the open, downstream end. The horizontal field (B_y) from the flipping output coil, the adiabatic coil field in the vertical direction (B_xCoil) and the residual fields from the analyzing magnet (B_xMag) are shown. The total field adiabatically rotates from $\hat{y}$ to $\hat{x}$.

5.6 Cryogenics

Figure 5.13 shows a cross sectional view of the cold-bore cryostat (Project Number 37409.4), which was built to our specifications by Oxford Instruments Inc. The low magnetic field criterion required the cryostat be constructed with non-magnetic materials, primarily aluminum and G-10 (a fiberglass and epoxy material). The cryostat consisted of a liquid nitrogen cylindrical shell and a co-axial liquid helium cylindrical shell each surrounded by a single vacuum region. The inner cylinder of the liquid helium region forms the 12 inch diameter cold-bore boundary. Our target insert was placed into this cold-bore region and thermally linked to the helium can. The insert diagnostic and π-coil current wires were soldered to twisted wire pairs threaded through the cryostat and room temperature electronic feedthroughs.

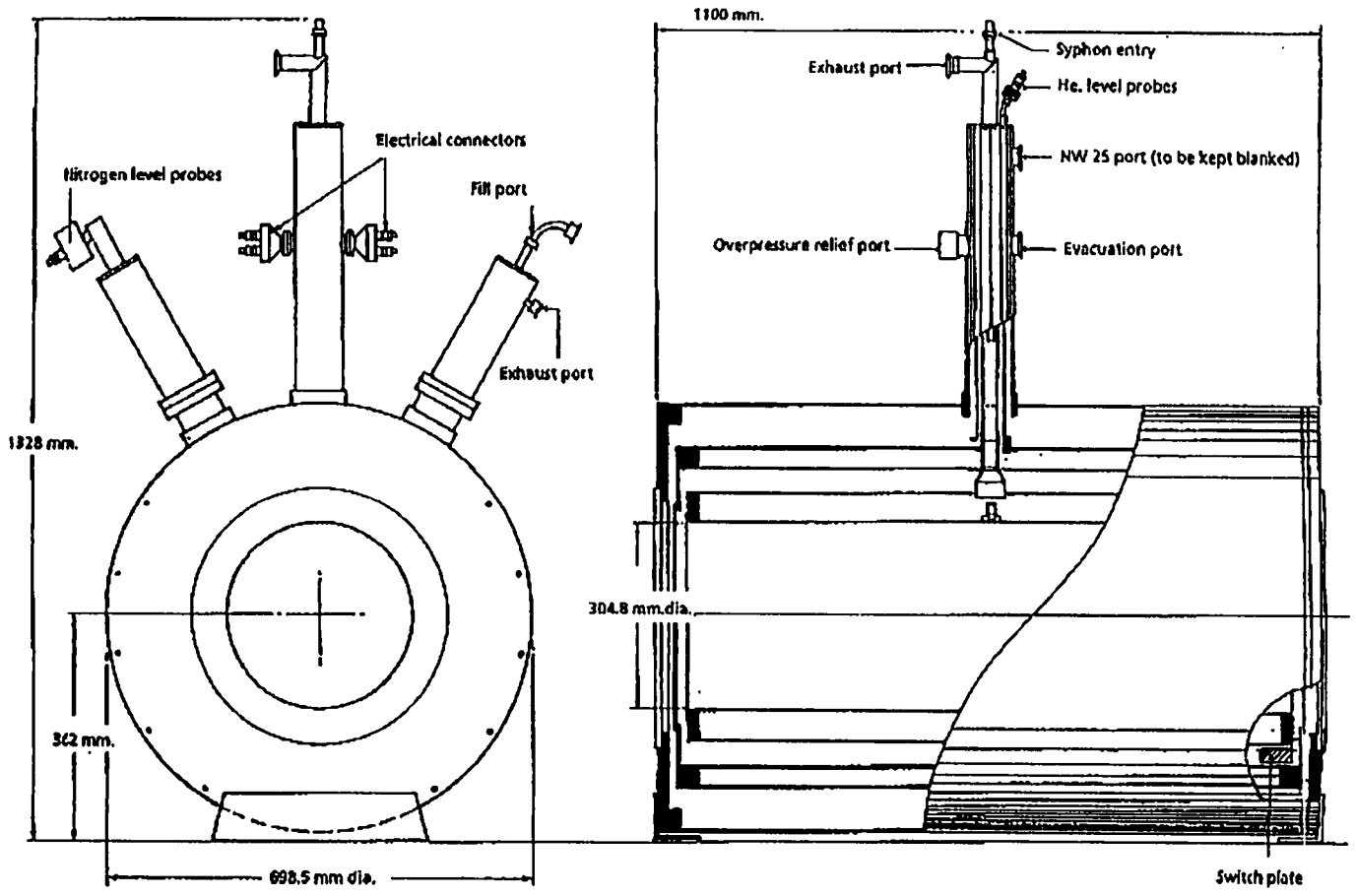

Figure 5.13: Sketches from the Operator's Handbook for the horizontal cold bore cryostat constructed by Oxford Instruments, Inc. [Oxf]

Cool-down tests showed movement of the cold-bore relative to the outer vacuum can from room temperature, 300 K, down to liquid nitrogen temperatures, 77 K, (the range in which most of the contraction and movement would occur) was at most 15 mils in any one direction. Therefore, alignment was performed at room temperatures.

A large source of heat entered the cryostat through the insert feedthrough tubes which were at room temperature at one end and 4 K, 26 inches away at the other end. We placed a 77 K thermal anchor on the G-10 tubes approximately 10 inches from the liquid helium end. In addition, the running of the pump for the target fill system put a non-negligible amount of heat into the system. We estimated our total heat load on the system was about 1 Watt.

We transfered the heat on the insert to the Oxford cryostat to prevent the insert temperature, and therefore the pressure, from rising and subsequently increasing the neutron scattering in the targets (as discussed in Section 4.5.2), and to prevent boil-off of the target reservoir helium. Unfortunately, the thermal link between the insert and the cold bore was not optimal, providing an insufficient transfer of heat from the insert to the cryostat.

We lowered the temperature of the insert by pumping on the Oxford cryostat helium can. We attempted a balance of reduced temperature, constant pressures, and minimum helium loss while pumping. We were able to prevent the temperature in the insert from rising above the pressures of the safety relief valve (1000 torr), and often were below the lower pressure relief valve setting of 900 torr. This corresponds to insert temperatures of 4.3-4.5 K.

Cold temperature vacuum leaks rendered the cryostat fill stacks aluminum to G-10 joints unreliable. The leak in the nitrogen fill stack was repaired before taking data. The helium stack became progressively problematic during the data acquisition time. This reduced our liquid helium hold time, caused difficulties during liquid helium filling and when pumping on the helium can to reduce the temperature.

5.7 Shielding and trim coils

The Earth's magnetic field is about 0.5 Gauss. We required the axial magnetic fields in the target region to be less than 100 μGauss. Changes in the magnetic fields must also be small and take place over time scales long compared to the data acquisition sequence.

The magnetic shielding consisted of two cylindrical μ-metal magnetic shields with end caps. To further reduce the magnetic fields, we placed solenoid coils inside the shields. Tests were performed to determine the effect of a cylindrical coil located between and inside μ-metal shields. With a previously constructed set of shields (smaller in size than our shields) and solenoid coils, we mapped the fields for different configurations of shielding and coil current. The axial field could indeed be reduced with a solenoid located inside the shields, though the effect of the coil on the axial profile was to alter the edge fields and reduce the axial distance where the field is flat. This was not a problem because the fields of the input and output coils dominated in those areas where the field was not flat.

The shield sizes were constrained by practical physical limitations and cost considerations. The optimum ratio of the length to radius for cylindrical shields is between 4 and 8, with the maximum shielding factor obtained for a ratio of 5.5 [Sum79]. For two nested cylindrical shields, the relationship between the lengths of the two, optimized for axial shielding, is given by $L_2 \sim (1.3)^2 L_1$, Similarly, the ratio of the radii, optimized for the shielding of transverse fields, is given by $R_2 \sim (1.3)R_1$.

Our inner shield was a cylinder made from 50 mil thick μ-metal material with a radius 15.4 inches and length 71 inches giving a length to radius ratio of 4.6. The outer cylindrical shield was constructed from 62 mil thick μ-metal into a radius of 19.1 inches and a length of 95 inches with a length to radius ratio of 5.0. The length ratio $L_2/L_1 = 1.3$ was smaller than the optimum while the radius ratio, $R_2/R_1 = 1.2$ was close to the best value. The μ-metal pieces were annealed after they were

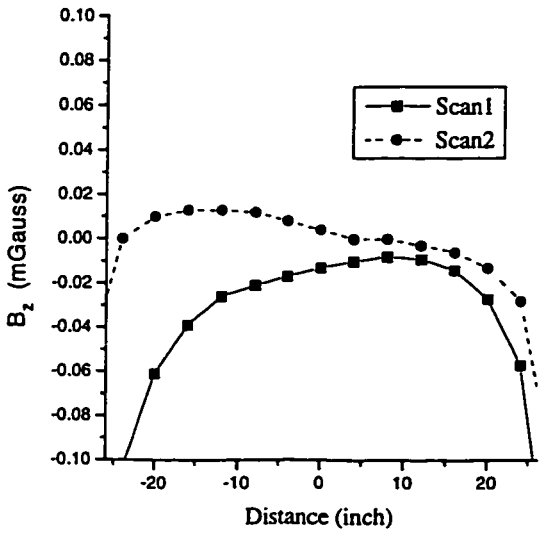

Figure 5.14: Measured axial fields at the neutron beam position. The fields were measured with the cryostat in place within the two layers of magnetic shields. The distances are given from the center, with the cryostat ends at ±20 inch.

machined to achieve the highest possible permeativity. Assuming a permeativity, $\mu = 20,000$, estimates for this shielding configuration (without end caps) predict an axial shield factor of about 100. The inclusion of end caps increases the estimate by a factor of about 10.

The two layers of shielding completely encompassed the cryostat. The shields were constructed in two axial halves, mechanically joined in the center with a seam of μ-metal strips. Three holes located radially in the center of the shields enabled the cryostat fill-stacks to penetrate the shields. Both the inner and outer shields contained 50 mil μ-metal end caps that fit snugly over the ends. Slots of dimension 12 inches by 6 inches were cut into the end caps to allow the input and output coils to extend beyond the end of the shields.

We measured and mapped the magnetic fields inside the cryostat (in the central

beam target region) with the two layers of shielding in place. The magnetic field criterion of less than 100 μGauss was met with a field of 40 μGauss maximum at the center, giving a shielding factor of greater than 5000 (much larger than expected). The fields along the central axis are presented in Figure 5.14, which shows the parabolic shape of the fields as a function of axial position. The axial field leakage effects from the openings for the input and output coils were measured, though in the end region, the neutrons see the dominant 5 Gauss field of these coils.

With the large measured shielding factor from the shields alone, we decided not to use a full solenoid coil as previously tested to further reduce the fields inside. Instead, to provide additional field shaping if needed, we formed two trim coils consisting of current loops wrapped on the cryostat inside both layers of shielding. A uniform field coil consisted of 4 windings on the cryostat ends and two sets of 2 windings one quarter the distance toward the center from the ends, all wrapped in the same direction. The gradient coil consisted of 4 loops on each end of the cryostat, wound in opposite directions. The coils were wound for positive current producing a positive axial magnetic field in the beam direction. The setting of these coils is discussed in Section 6.2.4.

The shielding factor for a single layer of shielding is proportional to the material permeability, defined as:

$$\vec{B} = \mu\vec{H} \qquad \text{where} \qquad \vec{H} = \frac{1}{\mu_0}\vec{B} - \vec{M} \tag{5.2}$$

and $\vec{M}$ is the magnetization of the material. The μ-metal is a ferromagnetic material with a large permeability. The permeability of the material is dependent upon the magnetic history of the material. As a result, the μ-metal must be periodically "degaussed" to restore the permeability of the material to its largest value. The degaussing process changes the magnetic state of the material from a point on the normal magnetization curve (B *vs.* H plot) to a point on the anhysteretic magnetization curve (B *vs.* H plot in which the permeability, μ, is larger). To achieve

this higher permeability, a large alternating magnetic field is applied in the material and is gradually reduced to zero. We used a degauss coil of 9 wires wrapped axially around the two shields so that an AC current of up to 15 amps induced a saturating magnetic field of about 1.3 k Gauss inside the μ-metal shield material. The degauss coil wires were open-circuited when not in use.

5.8 ^{3}He neutron detector

With an expected flux of 2×10^8 neutrons/second, we chose to integrate the charge collected from a segmented ionization chamber filled with a ^{3}He and Argon gas mixture. The neutrons were detected through the following reaction:

$$n + {}^3\mathrm{He} \rightarrow {}^3\mathrm{H} + {}^1\mathrm{H} \qquad \mathrm{Q} = 750 \text{ keV} \tag{5.3}$$

producing charged reaction products that ionized the gas mixture. An average energy of 28 eV was required to produce an ion pair in the gas, therefore, approximately 2.5×10^4 ion pairs on average were produced per neutron absorbed.

A drawing of the ^{3}He ionization chamber (designed and constructed by Steve Penn) is provided in Figure 5.15. A series of interspaced high-voltage and grounded charge collecting plates divide the detector into four collection regions. Half-voltage annular rings were placed between the sensing plates and the high-voltage plates to help shape the electric field, reducing fringing fields and sparking. The sensor plates contained an active region of 3 inches in diameter and were divided into 4 quadrants with a 1 mm spacing. There were 16 total channels for the collection of detector current, with each channel associated with one of the quadrants on one of the 4 plates. The electronics used to collect the detector current is described in Section 5.9 below.

We chose the argon partial pressure so that the proton range was less than 3 mm, which is sufficiently smaller than the 1 cm separation of the left and right beams. This proton range assured that the ion pairs produced by neutrons captured on one

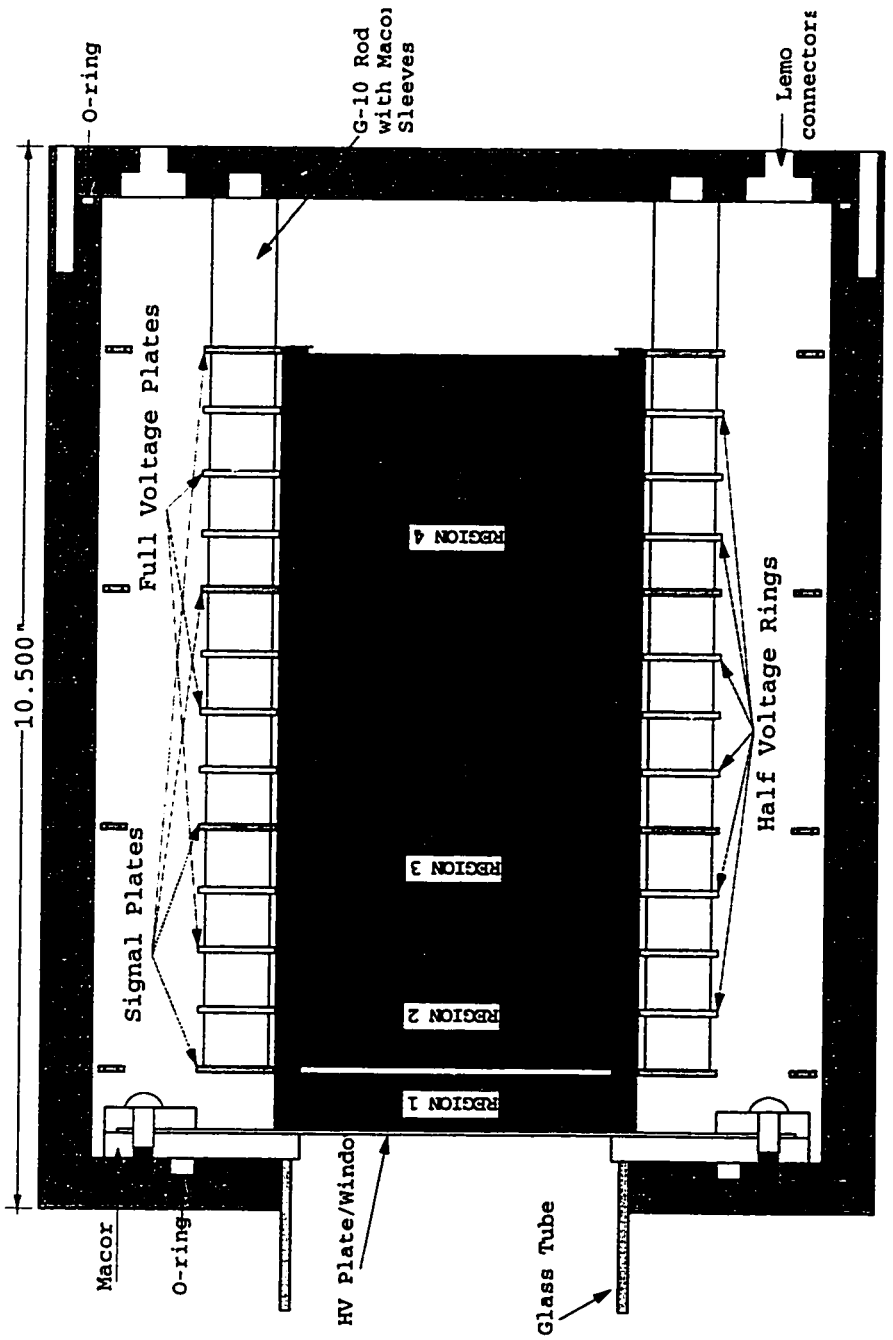

Figure 5.15: Longitudinal cut-away of the segmented ^{3}He ionization chamber.

side of the detector are collected on the same side. We checked the amount of left-right cross talk by blocking the beam on one half of the up-stream guide tube. The detected current on the blocked side dropped by a factor of 10^4.

The ^{3}He pressure was chosen to give similar detection sensitivity for the first, second, and combined third and fourth collection regions. For running pressures of 6.8 psi (0.5 atm) ^{3}He, and 44 psi (3.0 atm) Ar, the calculated fraction of neutrons absorbed for plates 1 through 4 was 31%, 34%, 25%, and 8%, with a 2% loss of neutrons onto the lithium absorber at the back of the detector.

The ^{3}He absorption cross section is proportional to $\frac{1}{v}$ so that the average velocity of absorbed neutrons increased with depth in the detector. Since the magnetic field rotations were inversely proportional to the velocity, while the PNC rotation was independent of velocity, comparing the measured asymmetries as a function of detector plate indicated the presence (or absence) of magnetic fields in the target region. The plate separation determined the sensitivity of the detector to distinguish small magnetic field rotations.

Table 5.2 gives the spacing between collecting plates, the calculated average velocity associated with each plate for the measured spectrum at the end of the apparatus. Using a Maxwell-Boltzman distribution, the peak wavelength was fit to the measured counts as a function of detector plate. Included in the table is the calculated rotation angle for a neutron with the given average velocity, traveling through a 100 μGauss field over a length of the target region (1 m). From the table, we see that the difference in magnetic rotation angle in the first and fourth plates is about 0.7 mrads out of a total of about 2.5-3.0 mrads. This difference in measured asymmetries was sufficient to determine the presence of fields on the order of 100 μGauss.

We operated the detector high voltage in the plateau region. Detector tests prior to the data runs gave an ionization plateau region between voltages of 1.0-1.7 kV. We ran at 1.2 kV.

Table 5.2: Detector plate velocity distribution for the measured neutron spectrum. The spin factor, γ is defined in Section 4.5.1. The magnetic rotation was calculated for a field of 100 μGauss over a 1 meter path length.

		Measured ($\lambda_{peak} \approx 5.9$Å)				
Detector Plate	Position [cm]	Velocity [m/sec]	Wavelength Å	Absorption [%]	γ [mrad/m-mG]	θ_{mag} [mrad]
1	1.50	576	6.7	33	33	3.27
2	4.50	646	6.1	34	29	2.92
3	10.50	724	5.5	23	26	2.60
4	19.50	802	4.9	7	23	2.35

5.9 Signal processing and experiment control

Figure 5.16 shows the signal path from the detector to the computer. We integrated a current of less than 40 nA per detector channel (associated with one quadrant of one sensor plate) and required that electronic noise be less than one part in 10^4.

We used a combined integrator and pre-amplifier circuit to collect the detector channel current and convert the integrated charge to an output voltage. The integrating pre-amp circuit was based on the Burr-Brown Low-Noise, Dual Switched-Integrator chip, ACF2101 [BBC95], with an external integration capacitor. There were 4 pre-amp boxes mounted on the back of the detector. Each box contained two ACF1201 chips, processing a total of 4 signals.

The computer controls the timing of the detector current integration with two incoming signals from a central pre-amp control box diagramed in Figure 5.16. The central pre-amp box serves to distribute the power and the control signals to the 4 integrator boxes. The RESET signal shorts the charge collecting capacitors to drain

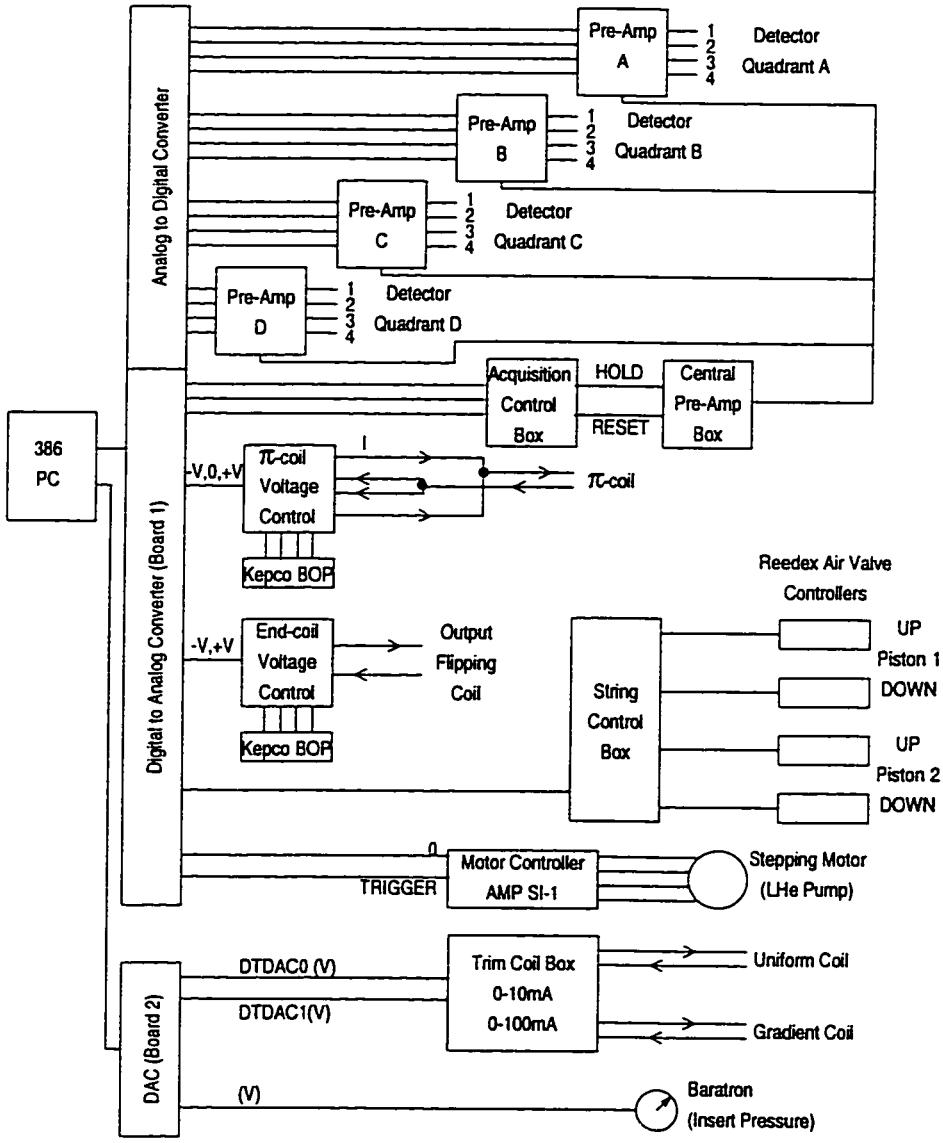

Figure 5.16: Signal processing and routing for the spin-rotation apparatus.

the charge. The HOLD signal determines when charge is collected on the capacitors.

We connected an external capacitor to the ACF2101 internal charge collection capacitor to optimize the output voltage. For maximum accuracy, the signal from the pre-amp should be in the upper range of operating voltages of the analog to digital converter (ADC) which accepts a maximum of 10 volts. We used 3 nf capacitors in the integration circuit for plates 1, 2, and 3 which collected charge from a current of about 30 nA per channel and 1 nf capacitors for plate 4, which collected charge from a 10 nA current.

We routed the voltage signal cables from the experiment beam line to the electronics rack located behind the biological shield. The Digital to Analog Converter (DAC) board received the analog voltage signal from the pre-amp and converted it to a digital signal. We used a PC running a 386 processor for data acquisition and experiment control. The computer program which controls the apparatus for the data acquisition sequence and the signal processing is described in Section 6.3.

The data collection sequence is presented in Figure 5.17. The computer controls this sequence through digital output that was converted to an analog voltage and sent to the pre-amp control box. When data were not being collected, the control box kept both RESET and HOLD at low voltage so that the capacitors were discharged.

For increased accuracy in measuring the integrated detector current, we recorded the voltages on the integrating capacitors before and after the integration interval. This was carried out with a series of HOLD, RESET and READ commands issued by the computer as depicted in Figure 5.17. The computer recorded the differences in capacitor voltages as an equivalent total charge collected for that state of the apparatus.

The detector and signal processing electronics were calibrated with a known current source. With the calibrated current source connected to the pre-amp integrator for one channel, we read the collected charge recorded as bits by the data acquisition program. The conversion of bits to nanocoulombs was determined for each channel.

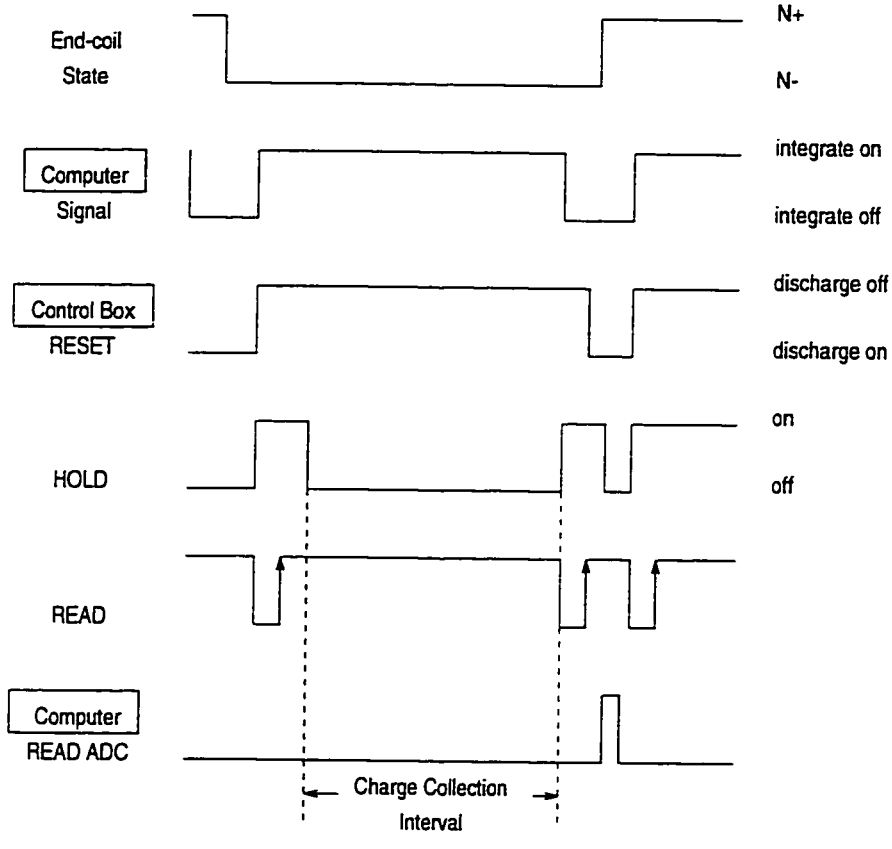

Figure 5.17: Timing sequence and control of the charge integration routine for data acquisition.

Since the spin-rotation measurements involved asymmetries, and therefore ratios of the collected charges, we emphasized in the calibration procedure that each channel read the same total nanocoulombs for the same source current. The absolute calibration of each channel was not as critical. The detector channel assignments and calibration factors are presented in Table 5.3.

The computer program controlled the states of the apparatus (see Section 6.3) through a sequence of digital signals. Figure 5.16 shows the routing diagrams for these control signals. To initiate the stepping motor that rotated the pump, the computer sent a digital high pulse to trigger the Applied Motion Products SI-1 Step Motor Indexer that controlled the Applied Motion Products 2035 Step Motor Driver. The drain-pipe location was determined by the position of the pistons controlling the strings. The piston control valves opened or closed based on a high or low pulse sent by the computer to the piston control box built at the Nuclear Physics Lab electronics shop. The current regulated power supplies for the π-coil, the flipping output coil, and the trim coils, received computer generated signals designating the sign, and the magnitude of the output current.

Table 5.3: Detector channel identification and calibration factors.

Detector				Pre-Amp	Calibration
Channel	Plate	Quadrant	Location	Capacitor (μF)	(bits/nC)
1	1	A	TOP/WEST	1.00	2998.64
2	1	B	TOP/EAST	1.00	3013.91
3	1	C	BOT/EAST	1.00	3048.65
4	1	D	BOT/WEST	1.00	3083.23
5	2	A	TOP/WEST	1.00	3034.42
6	2	B	TOP/EAST	1.00	3084.68
7	2	C	BOT/EAST	1.00	2950.19
8	2	D	BOT/WEST	1.00	3039.87
9	3	A	TOP/WEST	1.00	2992.31
10	3	B	TOP/EAST	1.00	3056.77
11	3	C	BOT/EAST	1.00	3119.79
12	3	D	BOT/WEST	1.00	3042.29
13	4	A	TOP/WEST	0.33	9311.46
14	4	B	TOP/EAST	0.33	10026.30
15	4	C	BOT/EAST	0.33	9975.95
16	4	D	BOT/WEST	0.33	9130.66

Chapter 6

DATA ACQUISITION

We assembled the spin-rotation apparatus on the NG-6 beam line, and collected preliminary test data during two reactor cycles. We characterized the beam profile, determined the polarimeter settings, debugged the data acquisition code, and optimized the acquisition methodology. In the following 6 week reactor cycle, PNC data were obtained.

6.1 Measurement of the neutron beam profile

We measured the beam profile with a fission chamber attached to an automated positioning system. A raster scan of the beam leaving the guide tube (before entering the input coil) is shown in Figure 6.1. As expected, the raster scan shows there was a sharp cut-off of the beam at the collimated edges, and the beam was completely blocked from the septum area. The scan revealed that the beam intensity entering our target region was greater in the lower "east" quadrant of the beam.

We measured the effective capture neutron count-rate at various points along the experimental apparatus, using a calibrated fission chamber. The capture flux is related to the true spectrum by a factor of about 3. Table 6.1 presents the measured capture flux rates and transmission factors along the apparatus.

As the beam progressed through the guide tubes and through the apparatus, the lower energy neutrons with the greater critical angle of reflection, are more likely to be lost than the higher energy neutrons. Thus, we expect the spectrum at the ^{3}He detector to be shifted to higher energies compared to the spectrum entering the initial

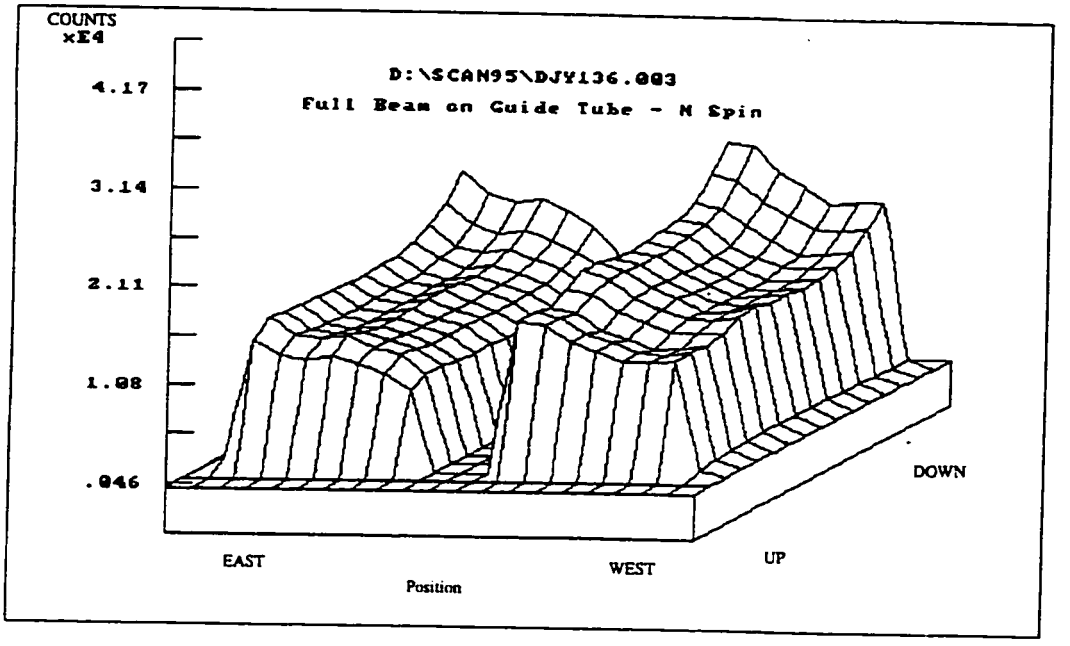

Figure 6.1: Raster scan of the neutron beam taken at the exit of the 8 foot guide tube. Data were collected using a calibrated fission chamber.

Table 6.1: Transmission through the apparatus. The effective total flux was calculated from the fission chamber calibration for the thermal capture flux. The count-rate in the final (detector) position was measured without liquid helium in the target chambers.

Position Along Beam Line	Avg Counts/100 Sec West	East	Total Flux Neutrons/cm^2/sec	Differential Transmission
Before Polarizer	63721		2.5×10^{-7}	
After Polarizer	15291		6.0×10^{-8}	24%
Guide tube Exit	5754	6967	2.5×10^{-8}	42%
End-Coil Exit	1102	1222	4.6×10^{-9}	18%
After Analyzer	328	383	1.4×10^{-9}	31%

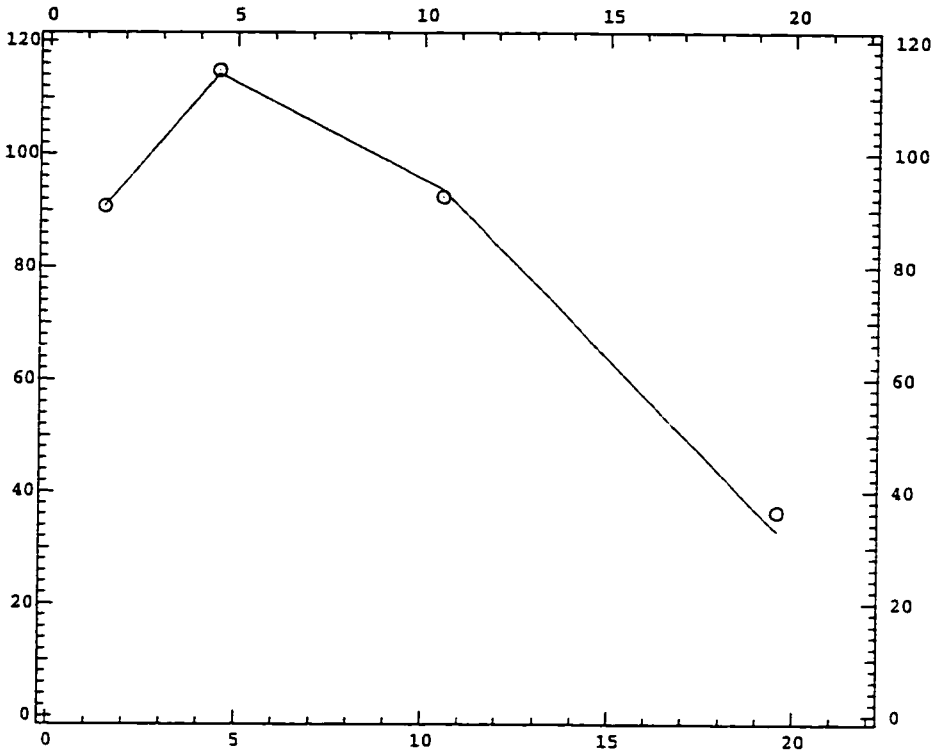

Figure 6.2: Measured neutron counts as a function of detector plate. Assuming a Maxwell-Boltzmann distribution with an exponent of 2, we fit the data to a peak wavelength of 5.96Å.

8 foot flight-tube. The detector current plotted as a function of plate is presented in Figure 6.2. The best fit of a Maxwell-Boltzmann shape to the ^{3}He detector data has a peak of 5.96 Å, compared to the 5.0 Å peak calculated for the NG-6 beam line. (See Figure 5.2.) In addition, similar fits to the detector current data by quadrant show that quadrant C, the lower, east side, (compare with Figure 6.1) has the lowest effective peak neutron wavelength and therefore the greatest average energy neutrons compared to the other 3 quadrants.

6.2 Setting the polarimeter parameters

This section discusses our procedures for orienting the input and output coils, optimizing the π-coil current, and setting the uniform and gradient field coil currents.

6.2.1 Alignment of the input and output coils

The π-coil field defined the vertical axis of the polarimeter. The front input coil must be rotated so that its axis coincides with that of the π-coil. In the absence of magnetic fields, the front coil would be aligned when the neutrons exiting this coil were not rotated by the π-coil. However, magnetic rotations occurred between the input coil and the π-coilTherefore, the input coil was in position when the rotation angle as measured by the count rate asymmetry (defined in Equation 4.8) was independent of π-coil current. We rotated the front coil until the measured asymmetry changed by less than 1×10^{-3} when the π-coil was switched on and off.

Similarly, the rear flipping coil axis must be set perpendicular to the π-coil axis. In the ideal case of zero magnetic fields and the rear flipping coil perfectly aligned perpendicular to the π-coil, the background spin-rotation is zero. To determine the rear coil position, we rotated the the output coil until the residual rotation was less than 1 mrad. (Effectively we assumed the background rotations were from misalignment only). This procedure was repeated after the fields were "zeroed" (Section 6.2.4).

In practice, this background rotation was greater than 1 milliradian for a fraction of the data, for example for one π-coil state, or in channels associated with one detector plate. The condition of 1 mrad was sought for the mean of the data from all detector channels.

6.2.2 Setting the π-coil current

As explained in Section 5.4, the choice of π-coil current was necessarily a compromise because the magnetic precession angle in the coil depends on the neutron wavelength.

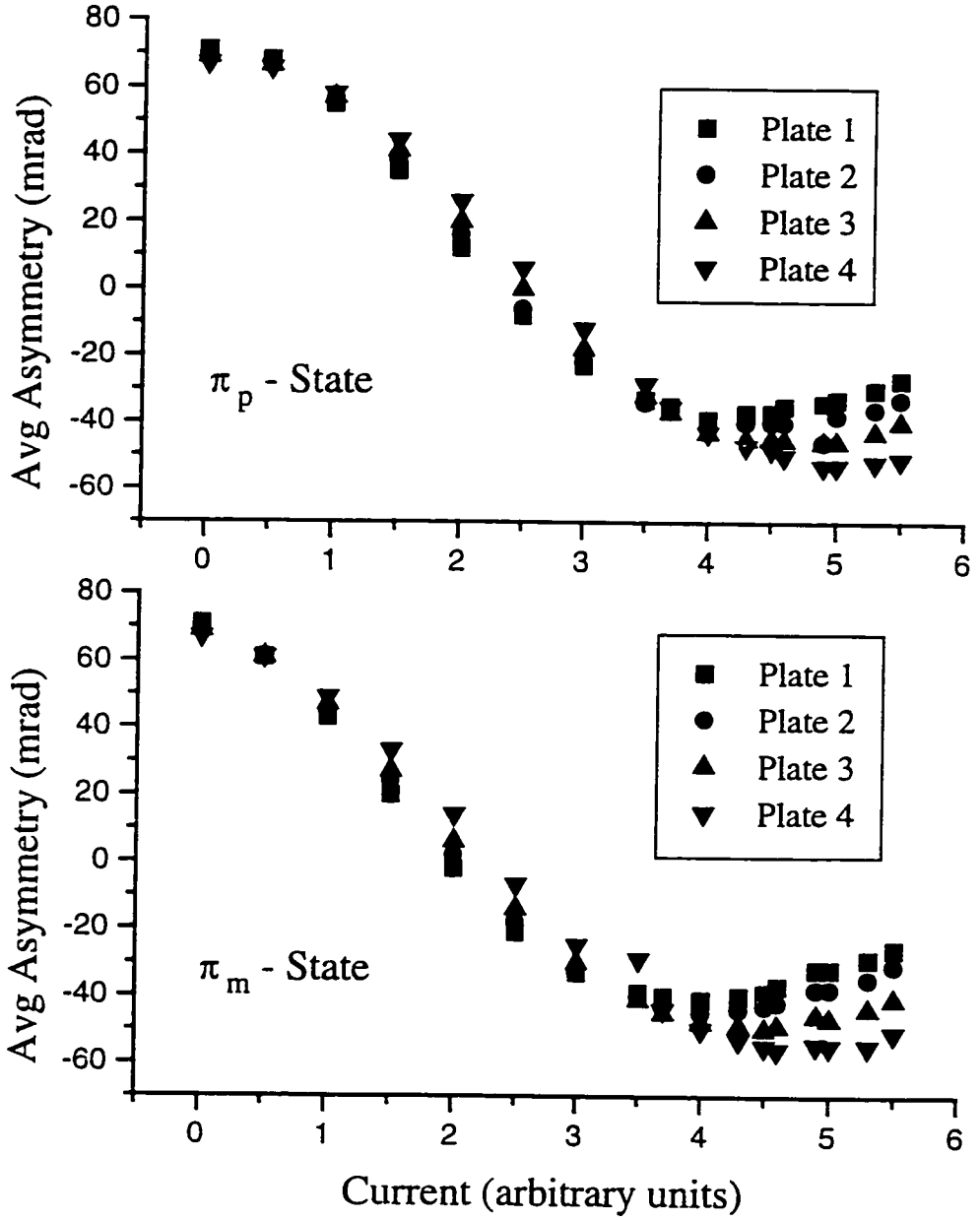

Figure 6.3: Measured asymmetry as a function of current in the π-coil. The current value of 4.0 corresponds to 156 mA in the π-coil. Curves for both the positive and negative π-coil current states are presented.

We stepped the π-coil current through a range of values about a nominal setting that rotated 5Å neutrons, the spectrum peak value, by 180 degrees. The asymmetry as a function of detector plate, or velocity, was measured for each π-coil setting. The observed rotations as functions of π-coil current are given in Figure 6.3.

We initially chose to run at a current setting of 4.4 on the π-coil plots, where the curves for plates 2 and 3 were minimized. This corresponded to a current setting of 172 mA, and a 2 Gauss field inside the coil. This current optimized the effective rotation (angle times polarization product) for neutrons detected by plate 2 which captured the largest fraction of the detected beam. According to calculations, this setting rotates 6.6 Å neutrons 180 degrees. Neutrons detected by plate 1 were over-rotated, and those detected by plate 3 were under-rotated by nearly the same amount. The smaller percentage of fast neutrons (plate 4) were clearly under-rotated. We later changed the π-coil setting to 156 mA, shifting the optimized rotation further to the slower neutrons. In this setting, the majority of neutrons were rotated by an angle between 135 and 225 degrees which maximizes the transverse spin factor. (See Figure 4.4.)

We initially performed this scan with helium gas targets at liquid nitrogen temperatures and then repeated the scan with liquid helium in the target chambers. The shape was nearly the same, implying that the velocity spectrum of the beam was not significantly altered by the liquid helium.

6.2.3 Polarization product measurement

After the front and rear coils were nominally aligned and the π-coil current was set, the polarization products (defined in Section 4.3) were measured. For the non-ideal polarimeter, (see Equation 4.11) the measured asymmetry is the product of the rotation angle times the polarization product factor ($\mathcal{P}$).

$$A_\theta = \mathcal{P} \sin\theta = \frac{(N_+ - N_-)}{(N_+ + N_-)} \tag{6.1}$$

The polarization product was determined by measuring the asymmetry for a large rotation of the neutron spin. We rotated the spins by an amount that was large compared to the magnetic background by rotating the input coil away from its aligned position. We increased the accuracy of determining the polarization products by measuring the asymmetries for two angles, one rotated in the opposite sense to the other, and taking the difference. We calculated the polarization product from

$$\mathcal{P} = \frac{\left(\frac{(N_+ - N_-)}{(N_+ + N_-)}\right)_1 - \left(\frac{(N_+ - N_-)}{(N_+ + N_-)}\right)_2}{\sin\theta_1 - \sin\theta_2} \tag{6.2}$$

where 1 and 2 refer to the two input coil positions.

The nominal angle of rotation was about $3\frac{1}{2}$ degrees clockwise and 1 degree counterclockwise from the normal input coil position. The asymmetric rotation of the input coil was a result of physical space limitations imposed by the magnetic shield openings. The difference measurement was independent of the exact angle of the input coil position, and relied on the micrometer setting which was reproducible to an estimated one part in 10^3.

We reduced the sensitivity of the measurement to linear drifts (for example, from magnetic fields or reactor fluctuations), by rotating the input coil to position 1 for one target cycle of data, then to position 2 for two target cycles, and finally to position 1 for an additional target cycle.

6.2.4 Zeroing the magnetic fields

Next, the magnetic field in the target region was minimized. The uniform component of the field was minimized with the π-coil off while the gradient field was minimized with the π-coil on. The currents in the corresponding trim coils were set so that the rotation angles as measured in the four detector planes were the same to less than 1 mrad. As discussed in Section 5.8, a difference of less than about 1 mrad on average between detector planes implies an integrated field in the target region of less than

100 μGauss. Thus,

$$\frac{A_\theta(Plate1)}{\mathcal{P}(Plate1)} = \cdots = \frac{A_\theta(Plate4)}{\mathcal{P}(Plate4)}. \tag{6.3}$$

We found that the gradient trim coil was not necessary, and accumulated data with this coil off.

After the magnetic fields within the target region were minimized, the routine to align the front and rear coils was repeated. We then iterated through the field reduction routine and the alignments of the input and output coils until these parameters were optimized.

The measured background asymmetries were continuously monitored during data acquisition. The iterative procedure of aligning the coils and zeroing the magnetic fields were repeated if the criteria were not satisfied. As the background magnetic fields slowly varied over time, periodic adjustments to the uniform trim coil were necessary.

6.3 Data acquisition sequence and control

Data were taken for each state of the apparatus designated by end-coil current polarity, π-coil current, and liquid helium target chamber configuration. The experiment controller cycled the system through the polarimeter states in a hierarchy that is presented in Figure 6.4 and discussed in detail below.

The computer control of the experiment and the data acquisition were integrated into one software program, NSAC (Neutron Spin-rotation Acquisition and Control) written by Erik Swanson. This program directed the control sequence for the apparatus, and managed the data retrieval and storage. The software was written in Microsoft FORTRAN for an IBM-compatible PC running under MS-DOS. For real-time interaction, assembler routines supplement the FORTRAN code to allow for subroutine calls from an interrupt, for programming of hardware modules, and for interception of keyboard input.

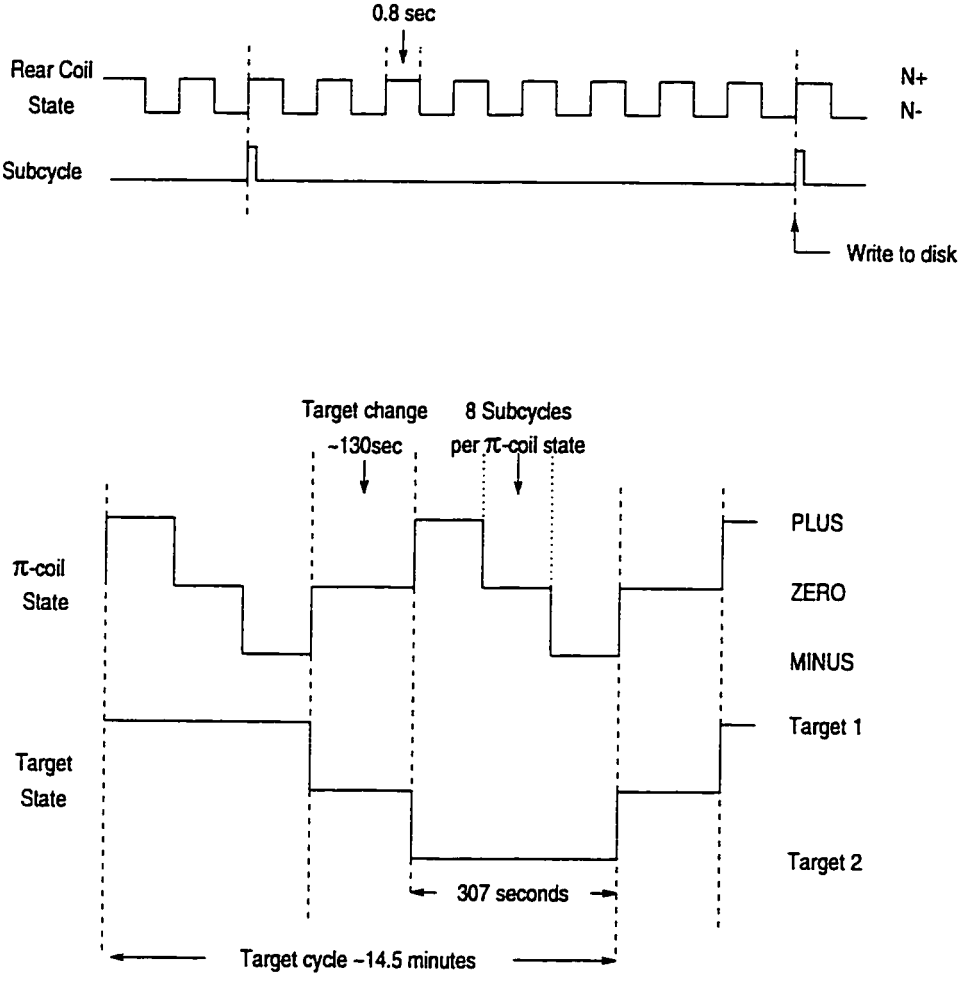

Figure 6.4: Control sequence and hierarchy of polarimeter states of the apparatus.

The control sequence timing was based on the computer's internal clock, which ticked 18.2 times per second, or 0.055 sec/tick. The end-coil current was flipped from positive to negative, or *vice versa*, after 15 clock ticks, or 0.82 seconds. The timing of each subsequent flipping parameter (π-coil current and target state) was based on the number of end-coil flips.

The timing sequence included a delay of 1 tick (55 msec) after the end-coil was flipped and before the program initiated the detector current integration process. This allowed magnetic field transients in the end-coil to die out before the data was collected.

The program flipped the end-coil state, and initiated the charge collection routine depicted in Figure 5.17. Since the integrator voltage was read at the initiation and termination of the charge collection interval, the recorded signal was proportional to the current accumulated during a specified amount of time, for a designated state of the apparatus, and was independent of voltage offsets.

An artificial data cycle parameter, denoted as a "subcycle", consisting of a user designated number of end-coil flips, was introduced for ease of storing data on disk. For each subcycle, the end-coil positive, (N_+), and end-coil negative, (N_-), counts were summed and these values were stored in the data file.

A specified number of data subcycles constitutes each π-coil state. There are nominally three π-coil states $(+, 0, -)$ for each target state. During the time when the target state was changing, the π-coil current was parked at zero current so that the actual π-coil sequence was $+, 0, -, 0, +, 0, \ldots$. Each set of subcycle summary data was written to disk at the completion of the data sequence, creating a single record containing data from a single target state. The completion of two target states constituted a target cycle at which point the program calculated such values as the asymmetry, and total counts.

For most data runs, we ran with 8 subcycles of 8 end-coil flips for a total of about 5 minutes of data acquisition for each target position. The 2 minute dead-time

associated with the target change-over, imposed a practical lower limit to the length of the target state.

During the target change-over sequence, all the target chambers are initially filled with liquid helium with the pump running and the drain-pipes in the up position. The drain-pipe associated with the next set of target chambers remains in the up position, while the drain-pipe for the current target set is lowered. While one set of target chambers drains, the other full set equilibrates, allowing any turbulence to subside, the target chamber temperature to become uniform, and bubbles to dissipate so that the density becomes homogeneous.

The target state is determined by which drain-pipe is lowered during the emptying process. For our configuration, target state 1 corresponds to full target chambers on the front east or "left" side and the back west or "right" side. The neutrons travel north in the beam line, so that the "left" and "right" sides of the apparatus are designated from the perspective of an observer looking upstream.[1] Target state 2 corresponds to the other two chambers filled; front right side and back left side.

Two primary modes of acquisition were used. The data acquisition mode cycled through the polarimeter states during normal data collection runs. For measuring the polarization products of the polarimeter, the program executed the measurement sequence described in Section 6.2.3 by prompting the experimenter to rotate the front coil and enter its position. In addition, during diagnostic runs, the target changing cycle could be suppressed (bypass target mode) for efficiently checking the system or accumulating test data while varying running parameters.

For some runs, the drain-pipe piston control leads were exchanged which reversed the target assignments, and changed which set of chambers was filled first in the target cycle. Similarly, the assignment of the π-coil states was changed by reversing

[1] This assignment of "left" and "right" is consistent with the designation of neutrons collected in the left and right sides of the detector from the perspective of an observer looking upstream at the back end of the detector.

the π-coil leads. We removed many possible spurious or correlated effects by averaging the results taken with randomly altered sequencing of the states of the system.

6.4 Experimental difficulties

The length of the data runs was determined by the hold time of the cryostat of approximately 34 hours. The high boil-off rate of liquid helium was a consequence of the large heat load on the insert, the vacuum leaks in the fill stacks and from pumping on the helium can. After allocating an hour total for polarization product measurements before and after each run, about 32 hours of data acquisition time were available between cryostat refills. Therefore, data runs were nominally 16 hours each. The long drain times, restricted these data runs to approximately 60 target cycles.

Our ability to acquire data was compromised by cold vacuum leaks. The Oxford Instruments cryostat developed an increasingly troublesome vacuum leak in the helium stack. The feed through tubes for the target chamber suffered from cold-shock induced vacuum leaks. The vacuum failure of a G-10 to aluminum joint on one of the feed through tubes required an online repair. Smaller leaks through cold O-ring seals greatly hampered the insert liquid helium refill process. In addition, ice entered the liquid helium reservoir which caused catastrophic damage to the pump and drive train necessitating online repairs. The total downtime as a result of cryogenic problems and repairs, was about 7 weeks.

Chapter 7

DATA ANALYSIS AND RESULTS

The challenging objective of the data analysis was to extract a parity-violating signal on the order of 10^{-7} radians from a background signal on the order of 2 mrads. We analyzed the data using the Data Analysis for Neutron Spin-Rotation (DANSR) computer programs written in FORTRAN that implemented the methods outlined below.

To determine the contributions to the target-dependent signal from PC effects, we must understand the extent that the neutrons see the same conditions for the two target states. These false signals arise either from count-rate asymmetries induced by target-position dependent scattering, or from target-dependent magnetic field rotations. The analysis of the data and of systematic test data includes a review of these sources of systematic errors.

7.1 Extraction of φ_{PNC}

The neutron counts collected in the jth detector channel for a specific end-coil state $(+,-)$ when the polarimeter was in π-coil state π, $(p,\ m,\ 0)$ and target state, T, (1 or 2) was given by

$$(N_{\pm})_{j,\pi,T} = \frac{1}{2}\mathcal{N}_{j,\pi,T}(1 \pm \mathcal{P}\sin\theta)_{j,\pi,T} \tag{7.1}$$

where $\mathcal{N} = N_+ + N_-$, and $\mathcal{P}$ is the polarization product in the specified detector channel, π-coil and target states.

7.1.1 Sources of neutron spin-rotation

We identified the following contributions to the total spin-rotation angle, θ.

$$\mathcal{P}\sin\theta = \mathcal{P}\sin(\alpha + \phi_{targ}) \approx \mathcal{P}(\alpha + \phi_{targ}) \tag{7.2}$$

where α represents rotations that were independent of the target state of the system, and ϕ_{targ}, (defined in Equation 4.18), represents the sum of the target-dependent PC rotations, $\varphi_{\mathrm{PC}targ}$, and the PNC rotation, φ_{PNC}. To a very good approximation for the small angles we measured, (on the order of milliradians or smaller), we replaced the sine function with the first-order linear term in the angle.

The target-independent rotations, α, include contributions θ_F and θ_B, the rotations from misalignment of the input ("front") coil and the output ("back") coil with respect to the π-coil axis, θ_{MF} and θ_{MB}, the magnetic field rotations in the front and back target regions respectively, and θ_π, the π-state dependent rotations from leakage fields and inhomogeneities in the π-coil field. We divided this non-ideal π-coil contribution into rotations in front of ($\theta_{\pi F}$) and behind ($\theta_{\pi B}$) the π-coil. We have,

$$\pi\text{-coil ON} \quad \begin{cases} \mathcal{P}\alpha = -\mathcal{P}_\pi(\theta_F + \theta_{MF} + \theta_{\pi F}) + \mathcal{P}_0(\theta_{MB} + \theta_B + \theta_{\pi B}) & \\ \mathcal{P}\phi_{targ} = -\mathcal{P}_\pi(\varphi_{\mathrm{PNC}} + \varphi_{\mathrm{PC}targ}) & \text{(target in front)} \\ \mathcal{P}\phi_{targ} = +\mathcal{P}_0(\varphi_{\mathrm{PNC}} + \varphi_{\mathrm{PC}targ}) & \text{(target in back)} \end{cases} \tag{7.3}$$

$$\pi\text{-coil OFF} \quad \begin{cases} \mathcal{P}\alpha = +\mathcal{P}_0(\theta_F + \theta_{MF} + \theta_{MB} + \theta_B) \\ \mathcal{P}\phi_{targ} = +\mathcal{P}_0(\varphi_{\mathrm{PNC}} + \varphi_{\mathrm{PC}targ}) \end{cases} \tag{7.4}$$

The relative contribution of each rotation to the overall precession of the spin polarization vector, was decreased by the polarization product factor associated with that rotation. Therefore, the product of $\mathcal{P}\alpha$ contains the linear sum of the individual contributions times their respective polarization products. For measurements with the π-coil current on, the rotations occurring upstream of the π-coil (θ_F, θ_{MF} and $\theta_{\pi F}$) were weighted by the polarization product factor for the particular current state, denoted as $\mathcal{P}_\pi$, and given a negative sign. The rotations occurring downstream of

the π-coil were not affected by the π-coil and were therefore weighted by the π-coil off polarization product, $\mathcal{P}_0$. For the π-coil on states, the polarization products multiplying the target-dependent rotations depended upon the position of the filled target with respect to the π-coil. For measurements with the π-coil current off, all polarization products were given by $\mathcal{P}_0$. We explicitly designated the sign for $\mathcal{P}_\pi$ and $\mathcal{P}_0$ so that all polarization products were positive.

7.1.2 Comparison by channel pair

We simultaneously collected data from two helium targets, one on each side of the beam. We summed the counts in a given data record taken for one target state, i (see Section 6.3). For a "right" side detector channel

$$(R_\pm)_{\pi,T} = \sum_k \frac{1}{2}\mathcal{N}_{k,\pi,T}(1 \pm \mathcal{P}_R\theta_R)_{\pi,T} = \frac{1}{2}\mathcal{N}_{R,\pi,T}(1 \pm \mathcal{P}_R\theta_R)_{\pi,T} \tag{7.5}$$

with an analogous expression for $L_\pm$, the counts in a "left" quadrant. We grouped the right channel and the opposing left channel into associated "channel pairs".

Taking the ratio of the expressions for the sum of the right and left detector counts, we obtain

$$\left(\frac{R_+L_-}{R_-L_+}\right)_{\pi,T} = \left(\frac{\frac{1}{2}\mathcal{N}_R(1+\mathcal{P}_R\theta_R)}{\frac{1}{2}\mathcal{N}_R(1-\mathcal{P}_R\theta_R)}\right)_{\pi,T}\left(\frac{\frac{1}{2}\mathcal{N}_L(1-\mathcal{P}_L\theta_L)}{\frac{1}{2}\mathcal{N}_L(1+\mathcal{P}_L\theta_L)}\right)_{\pi,T} \tag{7.6}$$

$$= \left(\frac{1+\mathcal{P}_R\theta_R-\mathcal{P}_L\theta_L}{1-\mathcal{P}_R\theta_R+\mathcal{P}_L\theta_L}\right)_{\pi,T} \tag{7.7}$$

$$\approx 1 + 2(\mathcal{P}_R\theta_R - \mathcal{P}_L\theta_L)_{\pi,T} \tag{7.8}$$

where we kept only first-order terms in θ. Note that in this ratio expression, the count-rate sums canceled. We therefore decreased the sensitivity of our signal to fluctuations in the count-rates by comparing the total counts of one plate quadrant to the associated quadrant on the other beam side.

As discussed in Section 4.2, the helium targets were filled so that the PNC rotation always had opposite signs on the two sides of the apparatus. We consider a

specific target state, T1, where right-side channels detected neutrons that traveled through the target in the back position, and left-side channels measured rotations produced with the target in the front position. Substituting the expressions for the total rotation angle, (Equations 7.3 and 7.4) into Equation 7.8, we obtain

$$\frac{1}{2}\left[\left(\frac{R_+L_-}{R_-L_+}\right)-1\right]_{\pi,T1} = (\mathcal{P}_R\theta_R - \mathcal{P}_L\theta_L)_{\pi,T1} \quad (7.9)$$

$$= [(\mathcal{P}\alpha + \mathcal{P}_0\phi_{targ})_R - (\mathcal{P}\alpha - \mathcal{P}_\pi\phi_{targ})_L]_{\pi,T1} \quad (7.10)$$

$$= [(\mathcal{P}_{0R} + \mathcal{P}_{\pi L})\phi_{targ} + \xi]_{\pi,T1} \quad (7.11)$$

where

$$\xi = -[\mathcal{P}_{\pi R}(\theta_F + \theta_{MF} + \theta_{\pi F})_R - \mathcal{P}_{\pi L}(\theta_F + \theta_{MF} + \theta_{\pi F})_L] + [\mathcal{P}_{0R}(\theta_{MB} + \theta_B + \theta_{\pi B})_R - \mathcal{P}_{0L}(\theta_{MB} + \theta_B + \theta_{\pi B})_L] \quad (7.12)$$

In an ideal experiment, ξ would be zero. In our case, ξ, the right-left difference in target independent rotations, was not zero because the right and left sides of the apparatus were not exactly the same. Field gradients in the $\hat{y}$ direction within the input and output coils contributed to differing misalignment rotations, θ_F and θ_B on the left and right sides. Magnetic field differences between the two halves of the target chamber produced left-right dependent magnetic rotations.

Since the rotations that contribute to ξ were target independent, this expression was the same for both target states. In target state T2, when the helium is in front of the π-coil on the right side, the target dependent rotations have a relative negative sign. The analogous expression of Equation 7.11 for target state T2 is

$$\frac{1}{2}\left[\left(\frac{R_+L_-}{R_-L_+}\right)-1\right]_{\pi,T2} = [-(\mathcal{P}_{0L} + \mathcal{P}_{\pi R})\phi_{targ} + \xi]_{\pi,T2} \quad (7.13)$$

For each channel pair, we averaged the left and right polarization products for π-coil on and off to define an effective polarization product factor that was independent of the target state.

$$\overline{(\mathcal{P}_0 + \mathcal{P}_\pi)} \equiv \frac{1}{2}((\mathcal{P}_{0R} + \mathcal{P}_{\pi L}) + (\mathcal{P}_{0L} + \mathcal{P}_{\pi R})) \quad (7.14)$$

Each data record, i, contains the counts for a single target state in either configuration T1 or T2. Using Equations 7.11 and 7.13, we obtained a general relation between the ratio of right-left counts and the spin-rotation angles, for any given record, i. For π-states π_p and π_m we have

$$\tilde{\phi}_{c,\pi,i} \equiv \pm\phi_{targ} + \frac{\xi_{\pi,i}}{(\overline{\mathcal{P}_0 + \mathcal{P}_\pi})} = \frac{1}{2(\overline{\mathcal{P}_0 + \mathcal{P}_\pi})}\left(\frac{R_+L_-}{R_-L_+} - 1\right)_{c,\pi,i} \tag{7.15}$$

where $\tilde{\phi}_{c,\pi,i}$ was the calculated value for the target dependent rotations for a given π-state (plus or minus) and data record, i. The plus sign in front of ϕ_{targ} was for target state 1 while the minus sign was for target state 2. We have explicitly included the notation for a single channel pair of data.

7.1.3 Separation of target independent rotations and drifts

If we simply subtract the expressions (Equation 7.15) for two successive target states, we obtain

$$\begin{aligned}
&\frac{1}{2}[\tilde{\phi}_{c,\pi,i} - \tilde{\phi}_{c,\pi,i+1}] \\
&= \frac{(-1)^{i+1}}{4(\overline{\mathcal{P}_0 + \mathcal{P}_\pi})}\left[\left(\frac{R_+L_-}{R_-L_+} - 1\right)_{T1} - \left(\frac{R_+L_-}{R_-L_+} - 1\right)_{T2}\right]_{c,\pi} \qquad (7.16) \\
&= (-1)^{i+1}\left[(\phi_{targ})_\pi + \left(\frac{[(\xi)_{T1} - (\xi)_{T2}]}{(\overline{\mathcal{P}_0 + \mathcal{P}_\pi})}\right)_{c,\pi}\right] \\
&= (-1)^{i+1}(\varphi_{\mathsf{PNC}} + \varphi_{\mathsf{PC}targ} + \alpha_r)_{c,\pi} \qquad (7.17)
\end{aligned}$$

where the plus and minus sign take into account whether record i is in target state 1 or 2 respectively. We define α_r as the contribution to the PNC signal from residual differences in the target independent rotations. Note that $\tilde{\phi}$ is expressed in Equation 7.16 in terms of measured quantities for the specified π-state, channel pair, and target state, and is expressed in Equation 7.17 in terms of the parameterized rotations.

While the expression ξ, was nominally independent of target position, the rotations that contribute were not independent of time. Two successive target states

were separated in time by about 7 minutes. During this time interval, the ambient magnetic fields may have drifted, changing the background rotations from one target state to the next, and α_r becomes non-zero.

To eliminate the contribution from α_r arising from linear and quadratic time-dependent drifts in ξ, we stepped through a quadratic smoothing routine,

$$(\overline{\phi_{\mathsf{PNC}}})_{c,\pi,i} \equiv (-1)^{i+1}\frac{1}{8}(\bar{\phi}_i - 3\bar{\phi}_{i+1} + 3\bar{\phi}_{i+2} - \bar{\phi}_{i+3})_{c,\pi} \tag{7.18}$$

We defined $(\overline{\phi_{\mathsf{PNC}}})_{c,\pi,i}$ as the averaged target-dependent rotations associated with record i, calculated from the ratio of counts in channel pair c in π-coil state π. The smoothing routine involves results from the 3 subsequent target states, therefore each value for $(\overline{\phi_{\mathsf{PNC}}})_i$ was correlated with that for three records before and after it in time.

7.1.4 Weighted sum over channel pairs

Our value of φ_{PNC} was obtained from a weighted sum of the $(\overline{\phi_{\mathsf{PNC}}})_{c,\pi,i}$, over all channel pairs. We combined the results from two channel pairs to form the result for a given plane. We combined the channel pairs on the top half of the detector to form the 'TOP' results and similarly for the lower half, or 'BOT' results. All detector channel pairs were combined to form the overall result denoted by 'ALL'.

The channel pair data contributed an uncertainty to φ_{PNC} based on two sources of error. The first comes from the measurement and the averaging of the polarization products associated with the channel pair and the second from statistical errors in the measured neutron counts. The polarization products ranged from 0.64 (channel 16) to 0.47 (channel 2), a factor of 0.75 less. In comparison, the measured neutron counts varied more by detector quadrant and plate (Section 6.1). In particular, the neutron current in the fourth plate was a factor of 3 smaller than that of the other three plates. In the analysis, the removal of half of the subcycles from the lower detector data altered the relative neutron counts associated with each channel pair. We therefore neglected the variance in the polarization products and weighted the

channel pair data based on the statistical error in the neutron counts, and the relative magnitude of the polarization products.

From Equation 7.15, the expression for the computed rotation for a channel pair and a single target state (before the smoothing routine) was given by

$$\tilde{\phi}_c = \frac{1}{2(\overline{\mathcal{P}_0 + \mathcal{P}_\pi})} \left(\frac{R_+ L_-}{R_- L_+} - 1 \right)_c \tag{7.19}$$

For a single target state and π-state, we calculated the weights, W_c, from the inverse square of the standard deviation as follows.

$$\sigma_{c,\pi}{}^2 = \left[\left(\frac{\partial \tilde{\phi}}{\partial R_+} \right)^2 \sigma_{R_+}^2 + \left(\frac{\partial \tilde{\phi}}{\partial L_-} \right)^2 \sigma_{L_-}^2 + \left(\frac{\partial \tilde{\phi}}{\partial R_-} \right)^2 \sigma_{R_-}^2 + \left(\frac{\partial \tilde{\phi}}{\partial L_+} \right)^2 \sigma_{L_+}^2 \right]_{c,\pi} \tag{7.20}$$

$$= \frac{1}{4(\overline{\mathcal{P}_0 + \mathcal{P}_\pi})} \left(\frac{R_+ L_-}{R_- L_+} \right)^2 \left(\frac{1}{R_+} + \frac{1}{L_-} + \frac{1}{R_-} + \frac{1}{L_+} \right)_{c,\pi} \tag{7.21}$$

$$= \frac{1}{W_{c,\pi}} \tag{7.22}$$

The expression for $\tilde{\phi}_\kappa$, where κ is a particular sum for a plate, top, bottom or all, becomes

$$\tilde{\phi}_{\kappa,\pi} = \frac{\sum_{c \in \kappa} \tilde{\phi}_{c,\pi} W_{c,\pi}}{\sum_{c \in \kappa} W_{c,\pi}} \tag{7.23}$$

These weighted sums ($\tilde{\phi}_{\kappa,\pi,i}$) replaced ($\tilde{\phi}_{c,\pi,i}$) in the smoothing routine, Equation 7.18.

We calculated the weights for each channel pair using the neutron counts summed for a single record (target state) and then averaged the weighting factor over the records in 22 data runs taken with the the π-coil current at 156 mA. These data were collected under the same data acquisition parameters and therefore had similar total count-rates for each channel pair. By construction, the averaged weights were independent of target state and data run.

7.1.5 The final experimental signal

We averaged the smoothed results $(\overline{\phi_{\mathsf{PNC}}})_{\kappa,\pi,i}$ for κ=all (the sum over all channel pairs in one π-state) over all records within one set of data runs, grouped by similar data

acquisition sequencing structure and π-coil current.

$$(\overline{\phi_{\mathsf{PNC}}})_{\pi} = \frac{1}{n}\sum_{i=1}^{n}(\overline{\phi_{\mathsf{PNC}}})_{\pi,i} \tag{7.24}$$

where n was the number of records in a data set.

To obtain the final value for φ_{PNC}, we averaged the results for the π_p and π_m states. This removed any linear dependence of our signal on the π-coil magnetic fields. To first order, effects of the π-coil leakage fields and inhomogeneities within the coil, reversed with the current. Our final experimental result was the quantity

$$(\overline{\phi_{\mathsf{PNC}}}) = \frac{1}{2}[(\overline{\phi_{\mathsf{PNC}}})_{\pi_p} + (\overline{\phi_{\mathsf{PNC}}})_{\pi_m}] \tag{7.25}$$

which is related to φ_{PNC} by

$$\overline{\phi_{\mathsf{PNC}}} = \phi_{targ} = \varphi_{\mathsf{PNC}} + \varphi_{\mathsf{PC}targ} \approx \varphi_{\mathsf{PNC}} \tag{7.26}$$

7.2 Polarization product calculation

Polarization product calibration runs were taken before and after each data run and with the same set-up of the polarimeter. For example, if data were taken with the π-coil leads switched, then the polarization product data were also accumulated with the switched π-coil leads.

Tables 7.1 and 7.2 list the polarization products for each detector channel averaged over all the calibration runs taken for the π-coil current setting of 172 mA and 156 mA respectively. The polarization products vary as a function of detector plate or velocity, becoming larger for faster neutrons. In the π_0-state, this variance reflects the velocity-dependence of the supermirrors in which the polarizing efficiency increases with velocity. In the case with the π-coil current on, (π_p and π_m states) we see the effect from the under-rotation of the fast neutrons detected in plate 4, and the over-rotation of the slow neutrons in plate 1.

Comparing the two tables shows the advantage of running at the lower π-coil current setting. As expected for a reduced magnetic field, the slower neutrons were

Table 7.1: Polarization product values measured for each detector channel averaged over 17 runs with the π-coil current at 172 mA. The errors were calculated from the statistical fluctuations in the data.

	π_p State		π_m State		π_0 State	
Channel	Target 1	Target 2	Target 1	Target 2	Target 1	Target 2
1	.4293 ± .0015	.4283 ± .0017	.4341 ± .0017	.4331 ± .0018	.8732 ± .0016	.8756 ± .0022
2	.3993 ± .0015	.3992 ± .0014	.4341 ± .0017	.4331 ± .0018	.8509 ± .0017	.8521 ± .0023
3	.4403 ± .0012	.4423 ± .0018	.4434 ± .0018	.4437 ± .0016	.8651 ± .0015	.8679 ± .0023
4	.4554 ± .0013	.4543 ± .0017	.4592 ± .0017	.4573 ± .0018	.8788 ± .0013	.8819 ± .0025
5	.4969 ± .0012	.4979 ± .0018	.5023 ± .0017	.5026 ± .0018	.8868 ± .0018	.8864 ± .0016
6	.4706 ± .0016	.4703 ± .0014	.4739 ± .0017	.4745 ± .0016	.8664 ± .0015	.8672 ± .0023
7	.5065 ± .0012	.5073 ± .0015	.5088 ± .0018	.5101 ± .0016	.8764 ± .0019	.8780 ± .0020
8	.5206 ± .0016	.5207 ± .0012	.5241 ± .0016	.5253 ± .0017	.8893 ± .0016	.8908 ± .0022
9	.5923 ± .0015	.5915 ± .0017	.5959 ± .0017	.5955 ± .0015	.9028 ± .0016	.9051 ± .0021
10	.5652 ± .0017	.5658 ± .0017	.5711 ± .0019	.5692 ± .0015	.8852 ± .0019	.8874 ± .0022
11	.5941 ± .0014	.5953 ± .0015	.5980 ± .0015	.5980 ± .0017	.8969 ± .0016	.8974 ± .0020
12	.6078 ± .0015	.6086 ± .0016	.6098 ± .0016	.6099 ± .0016	.9054 ± .0015	.9077 ± .0021
13	.6693 ± .0015	.6699 ± .0014	.6729 ± .0019	.6700 ± .0011	.9182 ± .0020	.9196 ± .0023
14	.6484 ± .0020	.6494 ± .0015	.6557 ± .0019	.6568 ± .0017	.9022 ± .0023	.9083 ± .0025
15	.6661 ± .0017	.6682 ± .0014	.6703 ± .0019	.6713 ± .0015	.9132 ± .0021	.9148 ± .0022
16	.6814 ± .0014	.6806 ± .0017	.6790 ± .0021	.6782 ± .0010	.9201 ± .0021	.9199 ± .0021

over-rotated less and the faster neutrons were further under-rotated. The polarization product values were greater for plates 1 and 2, in the energy range where we detect the most neutrons, essentially the same for plate 3, and reduced for plate 4 where we detect fewer neutrons.

7.3 Rejection of spurious data

7.3.1 Count-rate and asymmetry cuts

The count-rate asymmetry (proportional to the spin-rotation angle) ranged between $(0.1 - 5) \times 10^{-3}$ radians, depending upon time, neutron energy and π-coil current setting. Figure 7.1 shows, for a typical data run, the asymmetries calculated using

Table 7.2: Polarization product values measured for each detector channel averaged over 36 runs with the π-coil current at 156 mA. The errors were calculated from the statistical fluctuations in the data.

	π_p State		π_m State		π_0 State	
Channel	Target 1	Target 2	Target 1	Target 2	Target 1	Target 2
1	.4965 ± .0012	.4972 ± .0012	.5006 ± .0014	.5003 ± .0012	.8703 ± .0016	.8720 ± .0011
2	.4683 ± .0012	.4688 ± .0012	.4671 ± .0014	.4677 ± .0012	.8465 ± .0015	.8475 ± .0012
3	.5017 ± .0008	.5031 ± .0009	.5008 ± .0012	.5006 ± .0009	.8628 ± .0015	.8633 ± .0010
4	.5201 ± .0009	.5202 ± .0010	.5199 ± .0012	.5194 ± .0011	.8751 ± .0015	.8765 ± .0012
5	.5476 ± .0009	.5495 ± .0011	.5517 ± .0012	.5519 ± .0009	.8815 ± .0014	.8832 ± .0010
6	.5210 ± .0010	.5217 ± .0011	.5224 ± .0014	.5221 ± .0011	.8617 ± .0015	.8621 ± .0010
7	.5489 ± .0009	.5509 ± .0009	.5493 ± .0012	.5450 ± .0009	.8750 ± .0014	.8762 ± .0011
8	.5681 ± .0008	.5694 ± .0010	.5667 ± .0011	.5668 ± .0010	.8866 ± .0015	.8873 ± .0010
9	.6047 ± .0009	.6057 ± .0009	.6090 ± .0011	.6093 ± .0009	.8973 ± .0014	.8992 ± .0010
10	.5787 ± .0009	.5796 ± .0009	.5839 ± .0011	.5831 ± .0009	.8807 ± .0015	.8822 ± .0010
11	.6005 ± .0008	.6019 ± .0009	.6019 ± .0012	.6021 ± .0008	.8807 ± .0015	.8822 ± .0010
12	.6212 ± .0008	.6213 ± .0009	.6155 ± .0012	.6154 ± .0007	.9015 ± .0014	.9028 ± .0010
13	.6279 ± .0009	.6280 ± .0010	.6309 ± .0012	.6303 ± .0010	.9111 ± .0016	.9115 ± .0011
14	.6050 ± .0010	.6069 ± .0011	.6138 ± .0011	.6134 ± .0013	.9001 ± .0015	.9014 ± .0012
15	.6181 ± .0008	.6197 ± .0010	.6228 ± .0011	.6224 ± .0008	.9127 ± .0013	.9135 ± .0011
16	.6406 ± .0009	.6396 ± .0010	.6312 ± .0011	.6303 ± .0010	.9185 ± .0016	.9185 ± .0010

the counts summed over all detector channels and averaged over the two target states.

As seen in Figure 7.1, the asymmetries drifted slowly on a time scale that is long compared to a single target cycle. One cause of this drift was the slowly varying insert pressure which affected the neutron transmission through the liquid helium target chambers. The asymmetries increased when the pressure decreased and decreased during the end of a run when the cryostat helium level was low and the insert temperature increased.

The background magnetic fields changed over time which altered the measured asymmetry. Gradual relaxation of the shields caused slow magnetic field changes. Movement of equipment in the area and magnetic activities of nearby experiments induced rapid changes in magnetic fields producing large step changes or a relatively

rapid drift in the asymmetries, depending on the length of time of the applied field and the time of the occurrence in the target cycle.

Records containing an asymmetry spike were eliminated. The smoothing sequence was halted at an asymmetry step change and a new sequence was initiated at the next record with the new asymmetry. On average, the asymmetry data fluctuated by about 0.5 mrads. We defined an unacceptable spike or step as a change in the count-rate asymmetry, A, by more than 1.3 mrads in comparison to the previous record, as As a check, we noted that this cut routine eliminated those data taken when we noted likely changes in the ambient magnetic fields from the movement of the over-head crane, or from activities of nearby experiments.

During data acquisition, changes in conditions external to the apparatus caused changes to the count-rate, producing asymmetries unrelated to the spin-rotation of the neutrons. One external influence on the count-rate was from step changes in the reactor flux resulting from the movement of control-rod shims used to adjust the reactor power. In some data runs, an early version of the data acquisition program occasionally read in zero bits, or was interrupted in the timing sequence, resulting in large asymmetry spikes in the data for one π-state.

We required that the count-rate in any one detector channel averaged over one target state not differ by more than 0.5% from the average for the previous target state. This count-rate condition excluded data at times when we had verified with the reactor operators that a shift in power occurred. The difference limit in count-rate also identified data from the bottom detector quadrants during target states in which we determined at the time of data acquisition that the targets were not draining below the beam height. The count-rate limit was exceeded because one target state drained slower than the other. The count-rate in each target state was the same when the liquid level in the empty targets for both configurations was below the beam height.

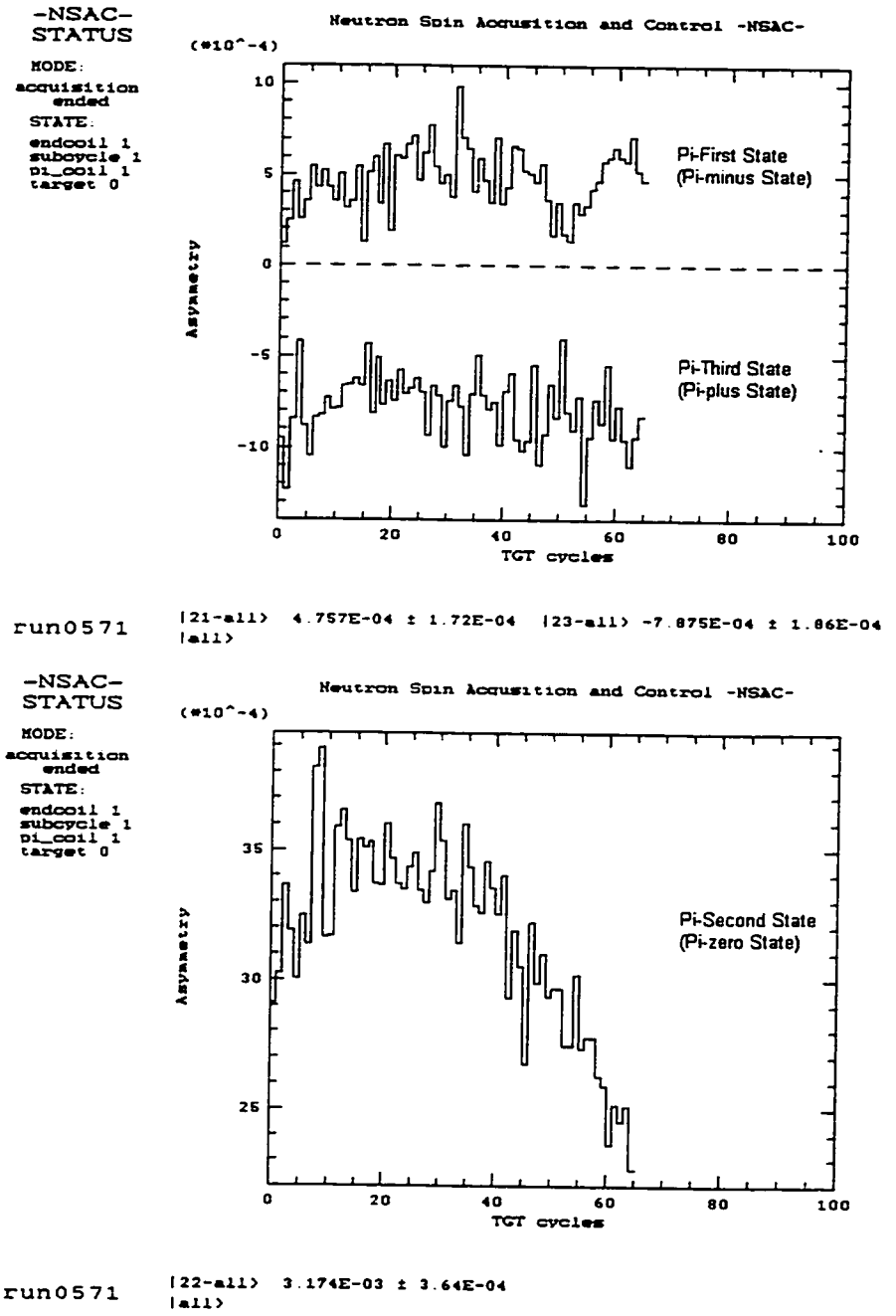

Figure 7.1: Example of measured asymmetries averaged over all detector channels for the π_p-state and π_m-state in the upper plot and the π_0-state in the lower plot. Data from a typical run are presented.

7.3.2 Scattering based cuts

We calculated the "front minus back" count-rate asymmetry, denoted A_{fb}, from the total counts collected when the target was in the front position and the total counted in the back position. For this asymmetry, the total counts $(N_+ + N_-)$ collected in the left channel during target state 1 were combined with the total counts in the corresponding right channel for target state 2 to form the total front position counts for a given channel pair. Similarly, the total counts were summed for the back target position. We formed the front-back count-rate asymmetry as

$$A_{fb} = \frac{N_{front} - N_{back}}{N_{front} + N_{back}} \tag{7.27}$$

We used A_{fb} as a measure of the target-position dependent count-rate asymmetry. Contributions to this asymmetry included differences in transmission through the two targets resulting from physical properties of the chamber, for example from a difference in length, or from effects of the windows. The differential scattering of neutrons out of the beam path, based on the different position of the liquid helium also contributed to A_{fb}.

Figure 7.2 shows the front-back count-rate asymmetry summed for the top channels, the bottom channels and all the detector channels. The data are presented as a function of subcycle, which translates to a time slice during the target state. The asymmetries were averaged over the records in the 22 data runs taken with 156 mA π-coil current.

The target count-rate asymmetries changed significantly during the target state. There were large changes in the bottom half of the detector for the first few subcycles and a gradual decrease in the top half. The target-dependent scattering was greater in the lower half with asymmetries on the order of 10^{-4}, compared to the upper half where the asymmetries were on the order of 10^{-5}.

The behavior of the top data resulted from the equilibration of the liquid helium after the chamber was filled. Density fluctuations and bubbles, gradually lessened as

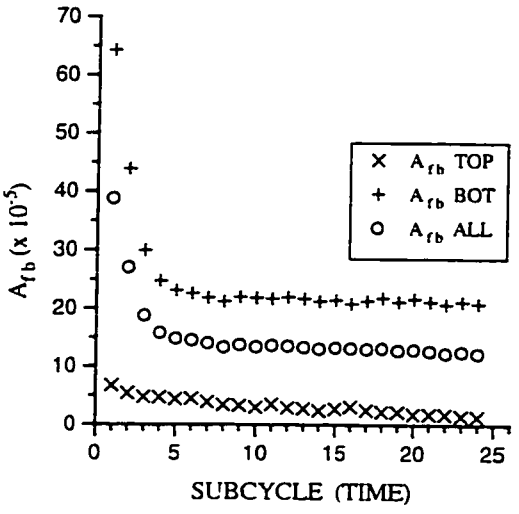

Figure 7.2: Front-back count-rate asymmetry as a function of time during the target state. The values were averaged over 2653 records at π-coil current 160 mA. Errors are the size of the symbol or less.

the liquid equilibrated. As the total scattering decreased, the front-back asymmetry decreased.

The bottom detector channel data indicate the presence of another scattering mechanism (confined to the bottom half of the target chambers) which initially decreased and then remained constant after the first four subcycles. Insufficient draining of the "empty" target chambers accounted for this scattering behavior. The scattering decreased rapidly as the liquid helium level in the empty target chambers continued to fall during the first four subcycles after the target change. While the liquid level was nominally below the beam height at the initiation of charge collection, the total neutron counts decreased by about .04% from the initial subcycle to its constant value later in the target state. The greater front-back asymmetries in the bottom half was from neutrons scattering off the pools of liquid helium located just below

the beam. We believe that the target collimators greatly impeded the helium flow, trapping liquid at a height above the bottom of the chamber.

For a symmetric apparatus, the front-back asymmetries should be small and independent of time. A typical statistical error in the bottom count-rate asymmetry data was on the order of 0.8×10^{-5}. We used this deviation as a measure of reasonable scatter in the data and imposed the condition that the front-back count-rate asymmetry differ from the value in the previous record by less than 1×10^{-5}. We therefore eliminated the first four subcycles from the data collected in the bottom half of the detector and the first subcycle from the top half of the data. After removing these subcycles, the front-back asymmetries were less than 0.6×10^{-4} in the top and less than 2.5×10^{-4} in the bottom half, giving an overall average of less than 1.5×10^{-4}.

7.4 Data Review

We studied the data from 22 runs acquired with the π-coil current at 156 mA, during the third reactor cycle to determine the trends, behavior and systematic dependences of the data. We examined the various asymmetries as a function of detector geometry, neutron velocity, time during the data target cycle, and current configuration of the π-coil to check if our measured PNC signal was independent of all these parameters. A dependence of our measured value would indicate the presence of false contributions.

7.4.1 Data as a function of detector region

Data from the 22 runs are presented in Table 7.3 which lists the averaged polarization product factor, $(\overline{\mathcal{P}_0 + \mathcal{P}_\pi})$, the average count-rate asymmetry, $\bar{A}$, the front-back asymmetry, A_{fb}, and the target-dependent rotations, $\tilde{\phi}_{c,\pi}$, for each channel pair.

The velocity dependence of the background asymmetries is evident by looking at the progression of $\bar{A}$ from plate 1 (slow neutrons), to plate 4 (fast neutrons). For the π_0-state where the magnetic rotations in the front and back add, we see that the

Table 7.3: Data as a function of channel pair from 22 runs with 156 mA π-coil current. $\bar{A}$ is the average asymmetry for the channel pair.

PLATE 1 **PLATE 2**

TOP	π_p	π_0	π_m	π_p	π_0	π_m
$\mathcal{P}$	1.342±.0018	1.718±.0018	1.343±.0019	1.407±.0016	1.744±.0016	1.409±.0017
$\bar{A} \times 10^{-4}$	0.54±0.16	-2.20±0.27	-13.56±0.15	1.93±0.16	-2.12±0.26	-13.91±0.15
$A_{fb} \times 10^{-5}$	4.29±0.16	3.81±0.14	4.12±0.15	4.09±0.13	3.34±0.12	3.31±0.13
$\bar{\phi} \times 10^{-6}$	1.26±2.61	-0.81±1.93	1.18±2.53	-0.23±2.26	-0.74±1.69	2.45±2.27
BOT	π_p	π_0	π_m	π_p	π_0	π_m
$\mathcal{P}$	1.381±.0016	1.739±.0016	1.380±.0017	1.441±.0015	1.762±.0015	1.439±.0016
$\bar{A} \times 10^{-4}$	8.70±0.16	-13.73±0.28	-23.24±0.15	8.71±0.16	-16.72±0.27	-1.10±0.15
$A_{fb} \times 10^{-5}$	28.76±0.94	28.63±0.94	28.51±0.94	23.19±0.81	23.15±0.81	23.17±0.81
$\bar{\phi} \times 10^{-6}$	5.07±2.77	-2.36±1.77	-5.53±2.65	3.86±2.41	-0.50±1.53	-0.66±2.30

PLATE 3 **PLATE 4**

TOP	π_p	π_0	π_m	π_p	π_0	π_m
$\mathcal{P}$	1.482±.0016	1.780±.0016	1.486±.0016	1.523±.0017	1.812±.0017	1.528±.0018
$\bar{A} \times 10^{-4}$	5.05±0.16	0.32±0.25	-13.58±0.16	11.67±0.18	7.64±0.25	-11.57±0.18
$A_{fb} \times 10^{-5}$	2.51±0.13	1.92±0.13	1.95±0.13	0.97±0.20	1.77±0.19	0.47±0.20
$\bar{\phi} \times 10^{-6}$	-2.56±2.60	4.09±2.00	0.36±2.50	2.13±3.81	3.05±3.03	-0.58±3.84
BOT	π_p	π_0	π_m	π_p	π_0	π_m
$\mathcal{P}$	1.509±.0015	1.796±.0015	1.507±.0016	1.545±.0016	1.832±.0016	1.542±.0016
$\bar{A} \times 10^{-4}$	8.41±0.16	-20.74±0.26	0.47±0.15	7.00±0.16	-25.95±0.25	3.19±0.16
$A_{fb} \times 10^{-5}$	16.83±0.67	16.53±0.66	17.16±0.66	10.13±0.56	10.88±0.54	11.07±0.55
$\bar{\phi} \times 10^{-6}$	0.50±2.52	-1.37±1.74	-3.17±2.40	1.58±4.13	4.80±2.67	3.07±3.85

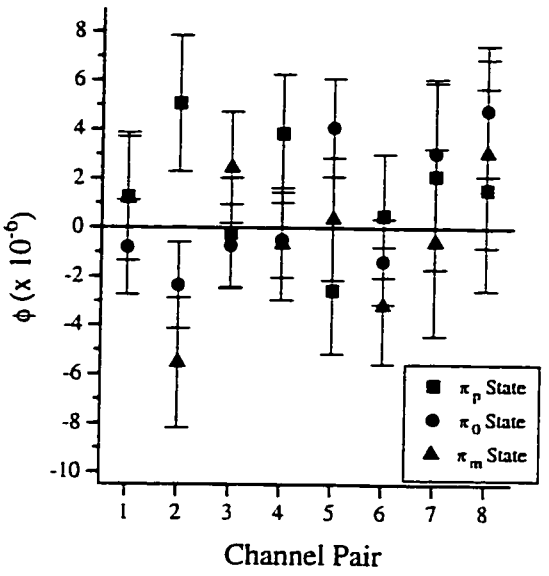

Figure 7.3: Calculated spin-rotation angle as a function of detector region for each π-state. Data are given in Table 7.3.

top asymmetries progressed from negative to positive and the bottom asymmetries to more negative values. This implies that the effective integral magnetic field in the top half of the apparatus was opposite to the effective field in the bottom half. Here, the average asymmetry was the sum of the contributions from the magnetic fields and the coil misalignment (see Equation 7.4). Assuming the velocity independence of θ_F and θ_B, we removed these misalignment rotations by subtracting asymmetries of one plane from another. We see from the table that the magnitude of the effective field which was proportional to the difference in asymmetries between plates 1 and 4, was nearly the same in the top ($\bar{A}(1,\pi_0) - \bar{A}(4,\pi_0) = -10 \times 10^{-4}$) and the bottom ($\bar{A}(1,\pi_0) - \bar{A}(4,\pi_0) = +12 \times 10^{-4}$) halves of the apparatus. The magnitude of the asymmetries was larger for the bottom π_0 case compared to the corresponding top values indicating an up-down dependence of the misalignment rotations.

Consistent with the discussions of the scattering effects in Section 7.6.4, the front-

back count-rate asymmetries were greater for the slow, long wavelength neutrons detected on plate 1 which have the larger beam divergences. Recall that the critical angle for reflection is proportional to the neutron wavelength. This supports the explanation of wavelength dependent reflection from residual helium increasing the target-dependent count-rate asymmetry.

Figure 7.4.1 shows a graphical representation of the $\tilde{\phi}_{c,\pi}$ data of Table 7.3. We did not observe a strong geometrical dependence or anomalous behavior in any one part of the detector.

7.4.2 Results as a function of time during the target cycle

Figure 7.4 shows the values for φ_{PNC} divided into top and bottom measurements and calculated for each subcycle after the target change. The data were scattered about zero and after the first four data subcycles, did not show a trend as a function of time.

In the first four subcycles, the value for φ_{PNC} in the bottom half was larger and more positive than that for the top. The large front-back count-rate asymmetry in the bottom half during this initial time interval possibly contributed a non-negligible amount to $\varphi_{\mathsf{PC}targ}$ and affected the φ_{PNC} result for these channel pairs. Consequently, as discussed in Section 7.3.2, the bottom channel data in the first four subcycles was not included in the analysis to calculate φ_{PNC}. In contrast, in the remaining subcycles, the results for the top and bottom halves were nearly equally likely to be more positive than the other value. The bottom data appear to scatter about zero less than the top data which fluctuated about zero with a larger spread in magnitude.

In Figure 7.5, φ_{PNC} is shown for the first and third π-states in the time sequence, averaged over each detector plate. Since we randomly altered which current state was first in the sequence, these data were independent of π-coil current assignment plus or minus. The data were consistent with zero and showed no dependence on the neutron energy.

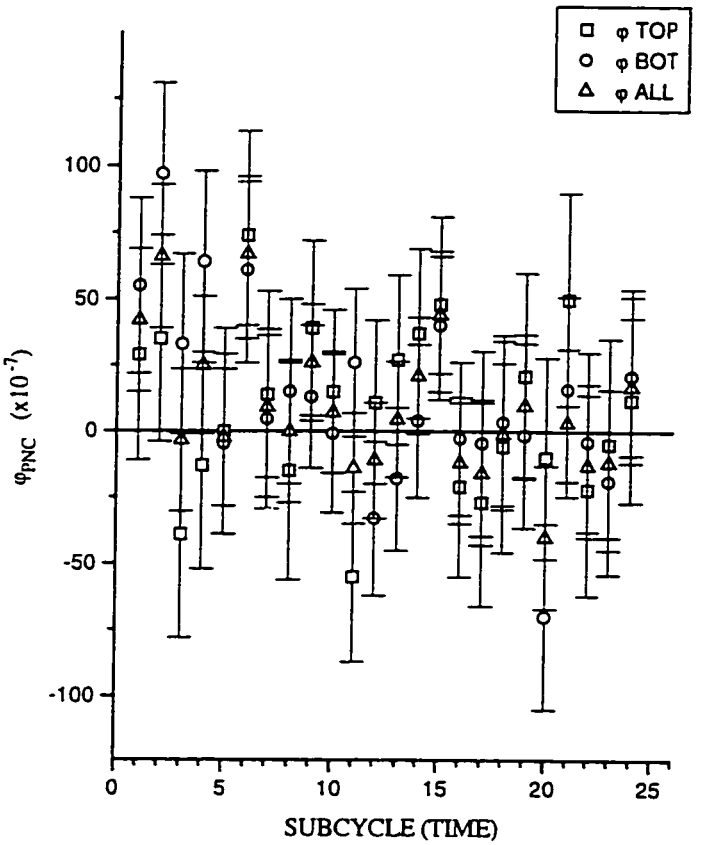

Figure 7.4: φ_{PNC} as a function of time during the target state. The values were averaged over 2653 records of data. Data for the top and bottom regions of the detector are shown separately.

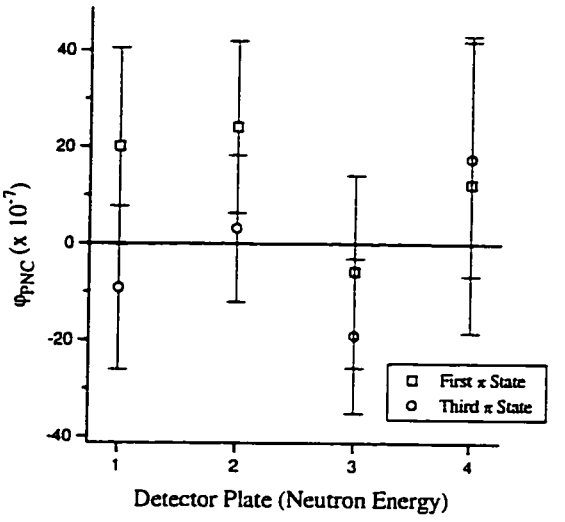

Figure 7.5: φ_{PNC} as a function of neutron energy (detector plate) for the first and third π-states in the target cycle.

7.4.3 Data as a function of π-state

We observed a difference between the two π-states in the behavior of the asymmetries as a function of detector quadrant as shown in Figure 7.6. For the π_p state, the average asymmetries in the left and right sides were each small. The same averaging in the π_m state gave large asymmetries for the right and left sides, which then combined to produce a relatively small channel pair asymmetry. For both π-states, the combined average was about 0.1 mrads.

The different behavior of the background asymmetries calculated in the two π-coil current states was also evident in the channel pair data of Table 7.3. In the π_p-state, the asymmetry was positive and independent of velocity in the bottom half whereas the asymmetries in the π_m-state were relatively large, negative and constant as a function of detector plate in the top half. The remaining asymmetries in these states

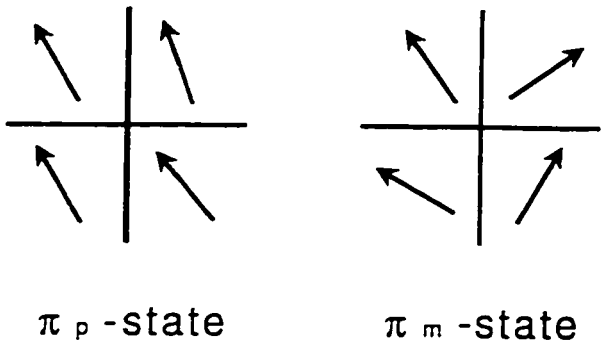

Figure 7.6: Pictorial representation of typical asymmetries by quadrant and π-state. The angles have been exaggerated for illustration. Note that one configuration cannot be rotated to the other.

showed typical velocity-dependent behavior.

The values of φ_{PNC} for the two π-coil current states as a function of channel pair are shown in Figure 7.4.1. Although the asymmetries exhibited different behavior in the two π-states, the values for φ_{PNC} were not significantly different. The extracted π_p-state and π_m-state signals for the bottom of plate 1, channel pair 2, were relatively large in magnitude, were opposite in sign, and differed by more than two standard deviations. This influenced the average for detector plate 1. The rest of the π-state pairs do overlap in value within one standard deviation.

The final value of φ_{PNC} was an average over the π_p and π_m states which removed any linear dependence of our signal on the π-coil fields. As seen in Figure 7.4.1, 6 of the 8 channel pairs have φ_{PNC} values that are opposite signs. An average of these results reduced the overall value for φ_{PNC}.

As a check, we look at half the difference in φ_{PNC} for the two π-states. In this expression, the φ_{PNC} term drops out and the π-coil dependent terms add. The 'half-difference' for plate 1 is 2σ from zero, while this value is well within one standard deviation of zero on the other plates. A study of the effects of the π-coil current on the signal is included in the discussion of systematic effects of magnetic fields. (See Section 7.6.2.)

7.5 Result for φ_{PNC}

In summary, we analyzed the data using only those records that satisfied asymmetry and count-rate difference criteria. We removed the data for the first 4 subcycles from the bottom detector channel pair data and the first subcycle from the channel pairs in the top half. The smoothed result $\overline{\phi_{\mathsf{PNC}}}$, the target-dependent rotations for each record, was averaged with all other records in the data runs that were grouped together. The runs were grouped for the same π-coil current, the same amount of data in a given record (same number of subcycles, π-coil cycles, and end-coil cycles), and whether all channel pairs or just the top channel pairs were included in the analysis. The listed value for φ_{PNC} is an average of the π_p-state and π_m-state results. A weighted average of these values for each data set gave the final result. The summary of data and the calculated φ_{PNC} are presented in Table 7.4.

Our criteria rejected 5% of the records in the data runs used in the analysis. We eliminated the bottom half of the data from 4 early runs when the empty targets contained liquid helium in the beam area, with a total of 236 records affected. The 22 data runs with the lower π-coil current, constituted about 240 hours (10 days) of data, including the π_0-state, which required 340 hours (14 days) to accumulate. These data were accumulated over 4 weeks of reactor beam time. The 10 earlier data runs contribute about 49 hours of additional data.

Table 7.4: Results for φ_{PNC} tabulated for the specified groups of data runs. The configuration of the polarimeter is listed for Normal, Pi-switched, Target-switched, and Both π-state and target states switched. The weighted average is given in the total.

π-coil	Run	Config	Records	$\varphi_{PNC} \times 10^{-7}$ (rads)
172 mA	410	N	1-24,26-138,140-177,179-184	-22.9 ± 48.6
172 mA	413	N	1-27 (Top)	13.0 ± 25.0
	417	N	1-13 (Top)	
	418	N	1-56 (Top)	
	429	N	1-40,41-140 (Top)	
172 mA	420	P	1-8,9-19,21-52	6.58 ± 33.7
	422	P	1-107,108-122,123-139	
	425	N	1-42,47-62	
172 mA	432	N	1-70	0.89 ± 32.0
	436	P	6-60	
156 mA	518	P	4-99,114-127	3.55 ± 7.23
	524	N	7-49	
	537	N	10-81,82-124	
	539	N	1-88,98-126	
	542	N	1-126	
	546	P	1-46,56-138	
	548	P	1-101,102-132	
	552	N	1-134	
	554	N	1-126	
	568	N	11-152	
	571	P	1-130	
	573	P	1-55,58-80,83-122	
	576	T	1-134	
	578	T	1-131	
	583	N	1-73,76-134	
	585	N	1-29,31-126	
	588	P	1-30,32-122	
	590	P	1-128	
	606	N	1-130	
	609	T	1-55,60-124	
	612	B	1-83,96-124	
	616	N	1-98	
TOTALS:			3443	3.7 ± 6.6

Our value for the parity non-conserving neutron spin-rotation through a 46 cm liquid helium target is

$$\overline{\phi_{PNC}} \approx \varphi_{PNC} = (3.7 \pm 6.6) \times 10^{-7} \qquad \text{radians} \tag{7.28}$$

where the error quoted is from statistical fluctuations in 3443 records of data. This value is consistent with zero.

7.6 Limits on Systematic Errors

There are two sources of systematic contributions to the measurement of φ_{PNC}. The first is the target dependence of the polarization products. The second is the effect of magnetic fields coupled to the target position. We also studied the sensitivity of the extracted signal to the analysis method.

7.6.1 Polarization Product Contribution

The scatter in the polarization product values measured for a given detector channel (Table 7.2) was about (0.1-0.2)%. The errors for the polarization product combinations for each channel pair (listed in Table 7.3), were also on the order of 0.1%. These measurements are limited by statistics and are sensitive to reactor fluctuations. The polarization product calculation necessarily used each data channel independently, so that we did not have a way to remove the sensitivity to the count-rate fluctuations.

Our signal was proportional to the average of the polarization products over the two target state positions. The target helium should not affect the neutron polarization, but a false signal could arise from a target dependence or neutron scattering dependence of the polarization products. For most of the data in Table 7.2, the polarization products for the two target states were the same within their statistical errors.

To determine the contribution to the false PNC signal from the target dependence of the polarization products. we collected data under conditions that isolated this

effect. We rotated the rear coil by a large offset rotation angle θ_B to increase the measured asymmetries independent of the target helium position and the π-state, so that $\mathcal{P}\alpha \approx \mathcal{P}_0\theta_B$. Substituting this background asymmetry into the residual signal expressions in Equations 7.12 and 7.17, we obtain

$$\xi = \mathcal{P}_{0R}(\theta_B)_R - \mathcal{P}_{0L}(\theta_B)_L = (\mathcal{P}_{0R} - \mathcal{P}_{0L})\theta_B \tag{7.29}$$

$$\alpha_r = \frac{\xi_{T1} - \xi_{T2}}{(\mathcal{P}_0 + \mathcal{P}_\pi)} = \frac{[(\mathcal{P}_{0R} - \mathcal{P}_{0L})\theta_B]_{T1} - [(\mathcal{P}_{0R} - \mathcal{P}_{0L})\theta_B]_{T2}}{(\overline{\mathcal{P}_0 + \mathcal{P}_\pi})} \tag{7.30}$$

$$= \frac{[(\mathcal{P}_{0R} - \mathcal{P}_{0L})_{T1} - (\mathcal{P}_{0R} - \mathcal{P}_{0L})_{T2}]\theta_B}{(\overline{\mathcal{P}_0 + \mathcal{P}_\pi})} \tag{7.31}$$

Two systematic data runs were performed; one with a large rear coil angle in the positive rotation sense and the other with a rear coil angle by the same amount in the negative rotation sense. Taking the difference in the results for the two runs increased the accuracy of determining the misalignment angle and the false signal contribution.

$$(\overline{\phi}_\pi)_{pos} - (\overline{\phi}_\pi)_{neg} = (\alpha_r)_{pos} - (\alpha_r)_{neg} \tag{7.32}$$

$$= (\theta_{Bpos} - \theta_{Bneg})\frac{[(\mathcal{P}_{0R} - \mathcal{P}_{0L})_{T1} - (\mathcal{P}_{0R} - \mathcal{P}_{0L})_{T2}]}{(\overline{\mathcal{P}_0 + \mathcal{P}_\pi})} \tag{7.33}$$

$$= (\Delta\theta_B)P_s \tag{7.34}$$

where the subscript "pos" and "neg" denotes the positive or negative rotation sense of the rear coil, and P_s is the "double difference" of the polarization products which is a measure of the contribution to the systematic error. For the π-coil on cases, the target-dependent rotation, ϕ_{targ}, canceled in the subtraction and $(\overline{\mathcal{P}_0 + \mathcal{P}_\pi})$ was the same for both, giving an expression that was independent of the π-state.

Table 7.5 gives the data from the two systematic runs and the calculated values for the terms in Equation 7.32. We rotated the rear coil by 39 mradians counter-clockwise for Run 565 and clockwise for Run 562, where the sense of the rotation is respect to $+\hat{z}$, looking along the beam momentum. As seen in the table, the actual average background asymmetry was 34-36 mrads for all three π-states. The misalignment angle dominated the background asymmetry compared to velocity-dependent

Table 7.5: Data from large rear coil rotation systematic test runs 565 and 562. The coil was rotated counter-clockwise during Run 565 and clockwise during Run 562.

π State	$\bar{A}$ (565) (mrads)	$\bar{A}$ (562) (mrads)	$\Delta\bar{A}$ (mrads)
P	35.96 ± 0.07	-33.80 ± 0.06	69.76 ± .09
0	35.47 ± 0.14	-34.81 ± 0.07	70.28 ± .16
M	34.76 ± 0.05	-34.54 ± 0.05	69.30 ± .07

π State	$\tilde{\phi}$ (565) ($\times 10^{-7}$)	$\tilde{\phi}$ (562) ($\times 10^{-7}$)	$\Delta\tilde{\phi}$ ($\times 10^{-7}$)	P_s ($\times 10^{-4}$)
P	10.9 ± 100.7	87.7 ± 64.0	-76.8 ± 119	1.6 ± 2.4
0	-43.8 ± 40.3	49.7 ± 51.9	-93.5 ± 65.7	-1.9 ± 1.4
M	136 ± 47.2	-16.5 ± 79.5	152.5 ± 92.5	3.1 ± 1.9
AVG	34.4 ± 39.4	40.3 ± 38.2	-5.93 ± 54.8	0.93 ± 1.1

asymmetries that were on the order of 1 mrad for a normal run. As expected, the background asymmetries in these runs were independent of the π-coil setting. The difference in background asymmetries was used to determine $\Delta\theta_B = 0.0703$ radians.

The false PNC signal was sensitive to the difference in the differences between the polarization products on the left and right sides for the two target positions. If the polarization product values were the same for the right and left sides, front and back target states, this residual term would be zero. From Table 7.5, the average double difference in the polarization products was $(0.9 \pm 1.1) \times 10^{-4}$, consistent with zero. The error in $2\mathcal{P}_0$ given in Table 7.3, was on the order of 2×10^{-3}. The combined error for directly calculating the double difference of the π-coil off polarization products was therefore on the order of 3×10^{-3}, an order of magnitude larger than these systematic data calculations. We therefore chose the systematic data analysis as our

reasonable limit for the double difference of the polarization products.

We determined the contribution of the difference in the polarization products to our signal by taking the product of the double difference result for the polarization products, and the average asymmetry, $\Sigma A = (-0.65 \pm 0.15) \times 10^{-4}$. We obtained

$$P_s \times \Sigma A = (-0.58 \pm 0.70) \times 10^{-8} \tag{7.35}$$

for the systematic contribution to φ_{PNC}.

The π_0-state result for $\overline{\phi}$ averaged over the two systematic data runs was $(\phi)_{\pm} = (54.5 \pm 40.8) \times 10^{-7}$, which was within 1.5 standard deviations of zero.

In addition, we directly examined the effects of averaging the polarization products on the calculation of φ_{PNC} by redoing the analysis with different $\mathcal{P}$ values. Running the analysis programs using only the polarization product factors for target state 1, or using only those for target state 2, or not averaging the values for the two states altered the results for φ_{PNC} at the level of 0.01×10^{-7}, well below the scatter errors.

7.6.2 Magnetic Field Contributions

We studied in two ways, the magnetic field contribution to the target-dependent PC signal, $\varphi_{\mathsf{PC}targ}$, and the ambient magnetic fields in the apparatus under normal data taking conditions. In the first case, we applied a uniform field that increased the average magnetic fields by more than a factor of 30. In the second case, we applied a gradient field almost 10 times greater than the normal data taking ambient fields. The front and rear coils were then aligned in this new configuration, so that the polarimeter was set in the same manner as the normal data runs, but with a large residual magnetic field.

To increase the sensitivity of the measurements, we applied equal and opposite fields in both cases, and subtracted the results. The large magnetic fields were produced by increasing the current in the uniform and gradient coils wrapped on the

cryostat. The computer setting for these coils was the same magnitude, but opposite in sign for the plus and minus field tests.

From Equations 7.3 through 7.4, we obtained the following expressions for the asymmetries in the π-coil on and π-coil off states.

$$A_{p/m} = -\mathcal{P}_{\pi p/m}(\theta_F + \theta_{MF} \pm \theta_{\pi F}) + \mathcal{P}_0(\theta_{MB} + \theta_B \pm \theta_{\pi B}) \quad (7.36)$$

$$A_0 = \mathcal{P}_0(\theta_F + \theta_{MF} + \theta_{MB} + \theta_B) \quad (7.37)$$

where we have ignored the target-dependent rotations that were orders of magnitude smaller than the background rotations. Note that we are interested in the π-coil leakage fields, θ_π, that are linear with the current, and therefore reverse sign upon reversal of the current sense.

We removed the π-coil dependent contributions by averaging over the π_p-state and π_m-state asymmetries. Similarly, we isolated the π-coil dependent rotations by subtracting the two as follows.

$$\Sigma A \equiv \frac{1}{2}(A_p + A_m) = -\mathcal{P}_\pi(\theta_F + \theta_{MF}) + \mathcal{P}_0(\theta_B + \theta_{MB}) \quad (7.38)$$

$$\Delta A \equiv \frac{1}{2}(A_p - A_m) = -\mathcal{P}_\pi\theta_{\pi F} + \mathcal{P}_0\theta_{\pi B} = \mathcal{P}_0\theta_\pi' \quad (7.39)$$

where $\mathcal{P}_\pi$ is the average polarization product for the two π-states and θ_π' is the effective total π-coil rotation that is the sum of the contribution behind the coil and the reduced contribution from in front of the coil. We combined these expressions to isolate the front and back rotations.

$$\frac{A_0 - \Sigma A}{\mathcal{P}_0 + \mathcal{P}_\pi} = \theta_F + \theta_{MF} \quad (7.40)$$

$$\frac{A_0(\frac{\mathcal{P}_\pi}{\mathcal{P}_0}) + \Sigma A}{\mathcal{P}_0 + \mathcal{P}_\pi} = \theta_B + \theta_{MB} \quad (7.41)$$

We combined the results for the two uniform field runs and the two gradient field runs. We obtained the average total effective π-coil rotation and the differences in the front and back rotations which were twice the contributions from the applied magnetic

field. Combining the two sets of data removed contributions from coil offsets. The results for the uniform and gradient field test runs are given in Tables 7.6 and 7.7, respectively. A more complete set of data for these runs is presented in Appendix B.

The average effective π-coil rotation, $\theta_\pi{}'$ was independent of neutron wavelength (detector plate). The π-coil leakage fields could not be axial, since any axial component to the leakage fields would have produced a wavelength-dependent rotation. The rotation was independent of the applied external fields.

A mechanism for producing this non-zero π-coil angle, $\theta_\pi{}'$, is shown in Figure 7.7. A constant field in the $\hat{y}$ direction (transverse to both the π-coil axis and the beam axis) would tip the π-coil axis in the xy plane in the same direction for both the positive and negative current state. This tip produced a different rotation axis for the two states. This would produce an asymmetric rotation of the spin based on the current sense of the π-coil, and could account for the differences in the measured asymmetries seen in Figure 7.6 and in Table 7.3. We estimate that this transverse component of the π-coil field was about 0.8 mGauss.

In Table 7.8, we list the asymmetry combinations for the 22 data runs at 156 mA π-coil current. (A more complete set of data can be found in Appendix B.) A comparison of these data with those of the systematic data runs provided a limit on the residual magnetic fields in the apparatus under normal running conditions and the effects of these fields on the results for φ_{PNC}. The misalignment rotations, θ_F and θ_B are independent of neutron wavelength. Therefore, the values in the last two difference columns of Tables 7.6 through 7.8 reflect the magnetic field induced rotations only. We have, for example, the difference between asymmetry factors in plates 1 and 4,

$$(\Delta\theta_F + \Delta\theta_{MF})_{P1} - (\Delta\theta_F + \Delta\theta_{MF})_{P4} = (\gamma_1 - \gamma_4)\Delta B \tag{7.42}$$

where γ_j is the wavelength dependent neutron spin factor plate j defined in Section 4.5.1.

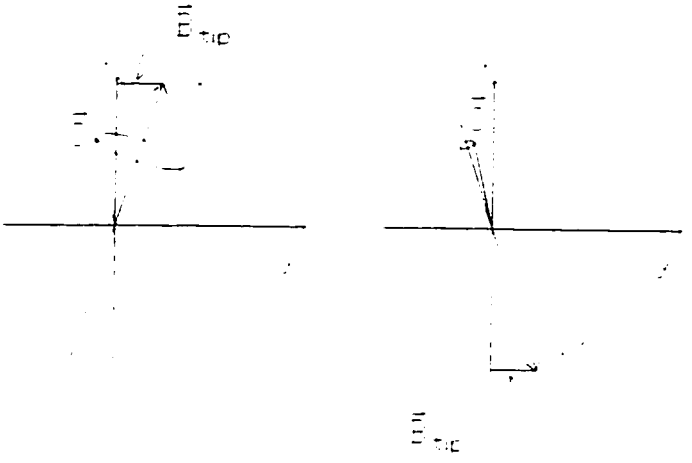

Figure 7.7: Schematic demonstration of the effects of a π-coil tip field. The π-coil is in the xy plane. $\hat{x}'$ is the tipped axis for one current sense, and $\hat{x}''$ is the tipped axis for the other sense of the π-coil current.

The data indicated that the applied uniform field was unexpectedly a factor of 2 larger in the back half of the apparatus than in the front half, and that the gradient field behaved as expected, nearly the same in magnitude and opposite in sign. The differences in plate asymmetries (listed in the last column of Table B.3) revealed the presence of a gradient field under data taking conditions since the back field is opposite in sign and smaller by 20%. Using the values listed in Table 5.2 for the neutron velocity averaged for each detector plate, and the equation defining the spin precession factor γ, (Equation 4.19) we calculated the ambient magnetic fields for the front and back halves of the apparatus (0.5 meters) under normal data taking conditions. From the difference in plates 1 and 4, we obtain 66 μGauss in the front half and -54 μGauss in the back half of the apparatus. However, comparing plates 1 and 3, yields 48 μGauss in the front and 7 μGauss in the back halves. Note that the data for the back rotations did not progress linearly from plate 1 to plate 4, so

we have no clear evidence for residual magnetic fields in the back target region. We collected data in the range of our design goal of 100 μGauss.

We calculated the PNC rotations for the uniform and gradient field data in the same way as with the normal runs. (See Table B.4.) We expect the false contribution of the magnetic fields to the target dependent rotations to be proportional to the resulting background rotations. Therefore, to determine the magnetic field contribution to the normal data PNC rotation, we multiplied the applied field PNC results by the ratio of the magnetic field rotations in the normal data and the applied field case.

The best measure of the magnetic field rotations from a uniform field was the total count-rate asymmetry in the π-coil off case. Similarly, the best measure of the gradient field rotations was the asymmetry with the π-coil on. We removed the coil alignment contribution to the background rotations by taking the differences in the asymmetries between plates. (Tables B.1, B.2 and B.3.) We present in Table 7.9, the product of the PNC rotations and these asymmetry ratios which gives a measure of the systematic contribution to the false PNC signal, $\varphi_{\mathrm{PC}targ}$.

The gradient field results were over an order of magnitude less sensitive than the uniform fields results. In the gradient field case, we ran with a weaker magnetic field strength (limited by our ability to set the front and back field coils) and the data runs were shorter. We therefore choose the uniform field results to put a limit on the systematic contribution from magnetic fields:

$$\frac{(A_0(P1) - A_0(P4))(\text{Normal Runs})}{\Delta A_0(P1) - \Delta A_0(P4))(\text{Uniform Field})} \times (\varphi_{\mathrm{PNC}})^{p,m} \lesssim 1 \times 10^{-7} \qquad (7.43)$$

where ΔA_0 refers to the difference in the positive and negative uniform field asymmetries for the π_0-state.

Table 7.6: Uniform field systematic test results. The asymmetries are given in milliradians.

Uniform Field Results (Run 597-Run 594)						
	Plate 1	Plate 2	Plate 3	Plate 4	P1-P3	P1-P4
$Avg(\mathcal{P}_0\theta_\pi')$	-0.56	-0.58	-0.59	-0.60	0.03	0.04
$Avg\theta_\pi'$	-0.65	-0.66	-0.67	-0.66	0.02	0.01
$\Delta(\theta_F + \theta_{MF})$	5.13	2.45	-1.32	-6.10	6.45	11.23
$\Delta(\theta_B + \theta_{MB})$	7.76	1.15	-7.26	-16.19	15.01	23.95

Table 7.7: Gradient field systematic test results. The asymmetries are given in milliradians.

Gradient Field Results (Run 603-Run 600)						
	Plate 1	Plate 2	Plate 3	Plate 4	P1-P3	P1-P4
$Avg\,(\mathcal{P}_0\theta_\pi')$	-0.52	-0.55	-0.56	-0.55	0.04	0.03
$Avg\,\theta_\pi'$	-0.60	-0.63	-0.62	-0.60	0.02	0.00
$\Delta(\theta_F + \theta_{MF})$	1.81	1.78	0.28	0.92	1.53	2.73
$\Delta(\theta_B + \theta_{MB})$	-0.21	0.29	1.03	2.03	-1.24	-2.23

Table 7.8: Asymmetry combinations for normal data runs. The plate asymmetries were calculated from the average over each quadrant asymmetry. The asymmetries are given in milliradians.

Normal Data (22 Runs at 156 mA)						
Asymmetry	Plate 1	Plate 2	Plate 3	Plate 4	P1-P3	P1-P4
$(\mathcal{P}_0\theta_\pi{}')$	0.54	0.56	0.57	0.58	-0.03	-0.03
$\theta_\pi{}'$	0.63	0.64	0.65	0.64	-0.02	-0.01
$\theta_F + \theta_{MF}$	-0.53	-0.65	-0.75	-0.84	0.22	0.30
$\theta_B + \theta_{MB}$	-0.55	-0.58	-0.53	-0.29	-0.02	-0.25

Table 7.9: Magnetic field systematic contributions to $\varphi_{\mathrm{PC}targ}$. This multiplicative table gives the systematic contributions in the boxes calculated from the product of the corresponding φ_{PNC} values (Table B.4) and Δ ratios (Tables B.1, B.2 and B.3.)

(Uniform)	$\varphi_{\mathrm{PNC}}{}^{p,m}$	$\varphi_{\mathrm{PNC}}{}^{0}$
$\frac{A_0(P1)-A_0(P4)}{(\Delta A_0(P1)-\Delta A_0(P4))}$	$(0.53 \pm 0.25) \times 10^{-7}$	$(0.53 \pm 0.26) \times 10^{-7}$
$\frac{A_0(P1)-A_0(P3)}{\Delta A_0(P1)-\Delta A_0(P3))}$	$(0.16 \pm 0.77) \times 10^{-7}$	$(0.16 \pm 0.80) \times 10^{-7}$

(Gradient)	$\varphi_{\mathrm{PNC}}{}^{p,m}$	$\varphi_{\mathrm{PNC}}{}^{0}$
$\frac{A_{p/m}(P1)-A_{p/m}(P4)}{\Delta A_{p/m}(P1)-\Delta A_{p/m}(P4)}$	$(7.49 \pm 10.27) \times 10^{-7}$	$(-2.16 \pm 10.95) \times 10^{-7}$
$\frac{A_{p/m}(P1)-A_{p/m}(P3)}{\Delta A_{p/m}(P1)-\Delta A_{p/m}(P3)}$	$(5.94 \pm 8.14) \times 10^{-7}$	$(-1.72 \pm 8.69) \times 10^{-7}$

7.6.3 *Background rotation differences, ξ*

We analyzed the data taken with the π-coil current off to monitor the system for spurious rotations and to look for scattering effects on the target dependent rotations. With the π-coil off the target dependent signal was no longer modulated, and Equations 7.10 through 7.13 are modified. The PNC signal will cancel in the subtraction and if we allow for right and left differences in the PC target dependent rotations, $\varphi_{\mathrm{PC}targ}$ we obtain,

$$\frac{1}{2}\left[\left(\frac{R_+L_-}{R_-L_+}\right)-1\right]_{\pi,T} = (\mathcal{P}_R\theta_R-\mathcal{P}_L\theta_L)_{\pi,T} \quad (7.44)$$

$$= [(\mathcal{P}\alpha+\mathcal{P}_0\phi_{targ})_R-(\mathcal{P}\alpha+\mathcal{P}_0\phi_{targ})_L]_{\pi,T} \quad (7.45)$$

$$= [(\overline{2\mathcal{P}_0}(\varphi_{\mathrm{PC}targ_R}-\varphi_{\mathrm{PC}targ_L})+\xi_0]_{\pi,T} \quad (7.46)$$

where the average π_0-state polarization product is given by

$$\overline{2\mathcal{P}_0}=\frac{1}{2}\left[(\mathcal{P}_0)_{R,T1}+(\mathcal{P}_0)_{L,T1}+(\mathcal{P}_0)_{R,T2}+(\mathcal{P}_0)_{L,T2}\right] \quad (7.47)$$

and ξ_0 is defined as

$$\xi_0 = [\mathcal{P}_{0R}(\theta_F+\theta_{MF})_R-\mathcal{P}_{0L}(\theta_F+\theta_{MF})_L] + [\mathcal{P}_{0R}(\theta_{MB}+\theta_B)_R-\mathcal{P}_{0L}(\theta_{MB}+\theta_B)_L] \quad (7.48)$$

Note that here with the π-coil off, the θ_π term did not contribute and the expressions are the same for the two target states.

A simple subtraction for two consecutive records in the π-coil off case becomes,

$$\frac{1}{2}[\tilde{\phi}_{c,\pi,i}-\tilde{\phi}_{c,\pi,i+1}]$$

$$= \frac{1}{4(\overline{2\mathcal{P}_0})}\left[\left(\frac{R_+L_-}{R_-L_+}-1\right)_{T1}-\left(\frac{R_+L_-}{R_-L_+}-1\right)_{T2}\right]_{c,\pi} \quad (7.49)$$

$$= \left[(\varphi_{\mathrm{PC}targ_R}-\varphi_{\mathrm{PC}targ_L})_{T1}-(\varphi_{\mathrm{PC}targ_R}-\varphi_{\mathrm{PC}targ_L})_{T2}+\left(\frac{[(\xi)_{0,T1}-(\xi)_{0,T2}]}{(\overline{2\mathcal{P}_0})}\right)_{c,\pi}\right]$$

As before, the ξ-dependent term was non-zero from drifts in time between the two target states. We assumed that ξ_0 varied at most quadratically in time so that

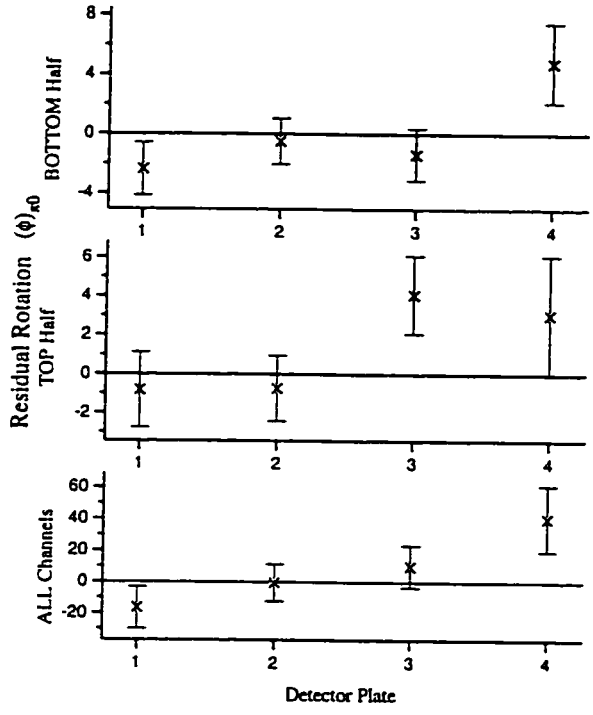

Figure 7.8: Residual rotations as a function of neutron energy and detector region. Data were taken with the π-coil current off.

the quadratic smoothing routine elimintated this term. We have for the averaged rotations,

$$(\overline{\phi}) = \left[(\varphi_{\mathrm{PC}targ_R} - \varphi_{\mathrm{PC}targ_L})_{T1} - (\varphi_{\mathrm{PC}targ_R} - \varphi_{\mathrm{PC}targ_L})_{T2}\right] \qquad (7.50)$$

The π_0-state results will be zero if the PC target dependent rotations are the same for the left and right sides. If there is a difference left and right, but there is no target dependence, this result will also be zero.

Figure 7.8 presents the residual target dependent rotations calculated from the π_0-state data of the 22 runs with the 156 mA π-coil current. Although the data might appear to indicate a non-zero slope for the rotation as a function of velocity, the error bars associated with each data point were large and a zero slope was consistent with

the data. Combining the results of the π_0-state data for the runs listed in Table 7.4, we calculated an overall value for the residual PC target-dependent rotation of $(0.26 \pm 6.67) \times 10^{-7}$, which was consistent with zero.

We also studied the residual target-dependent rotations by taking the ratio of up and down associated channel pairs, obtaining an expression for the difference of these asymmetries and proceeding as before. Reactor fluctuations were removed with the ratio expression, and the smoothing routine removed background rotations by subtracting the back and front results. In this analysis, all three π-states should give a result that is consistent with zero.

With the up-down channel pairs, we used the same convention for $U_\pm$ and $D_\pm$ defined in Equation 7.5. As in the π_0-state above, the PNC signal will cancel in the now up-down ratio expression, while any difference in the PC target-dependent rotation in the upper and lower halves of the apparatus will remain. As before, the signal for the π_p and π_m states will modulate from one target state to the other while the π_0-state signal will not.

We have

$$\frac{1}{2}\left[\left(\frac{U_+D_-}{U_-D_+}\right)-1\right]_{\pi,T} = (\mathcal{P}_U\theta_U - \mathcal{P}_D\theta_D)_{\pi,T} \quad (7.51)$$

$$= [(\mathcal{P}\alpha + \mathcal{P}_0\phi_{targ})_U - (\mathcal{P}\alpha + \mathcal{P}_0\phi_{targ})_D]_{\pi,T} \quad (7.52)$$

$$= [(\overline{2\mathcal{P}_0}(\varphi_{\mathrm{PC}targ_U} - \varphi_{\mathrm{PC}targ_D}) + \xi_{UD}]_{\pi,T} \quad (7.53)$$

where

$$\xi_{UD} = -(\mathcal{P}_{\pi U}(\theta_F + \theta_{MF})_U - \mathcal{P}_{\pi D}(\theta_F + \theta_{MF})_D) + (\mathcal{P}_{0U}(\theta_{MB} + \theta_B + \theta_\pi)_U - \mathcal{P}_{0D}(\theta_{MB} + \theta_B + \theta_\pi)_D) \quad (7.54)$$

for the π_p and π_m states, and

$$\xi_{UD} = -(\mathcal{P}_{0U}(\theta_F + \theta_{MF})_U - \mathcal{P}_{0D}(\theta_F + \theta_{MF})_D) + (\mathcal{P}_{0U}(\theta_{MB} + \theta_B + \theta_\pi)_U - \mathcal{P}_{0D}(\theta_{MB} + \theta_B)_D) \quad (7.55)$$

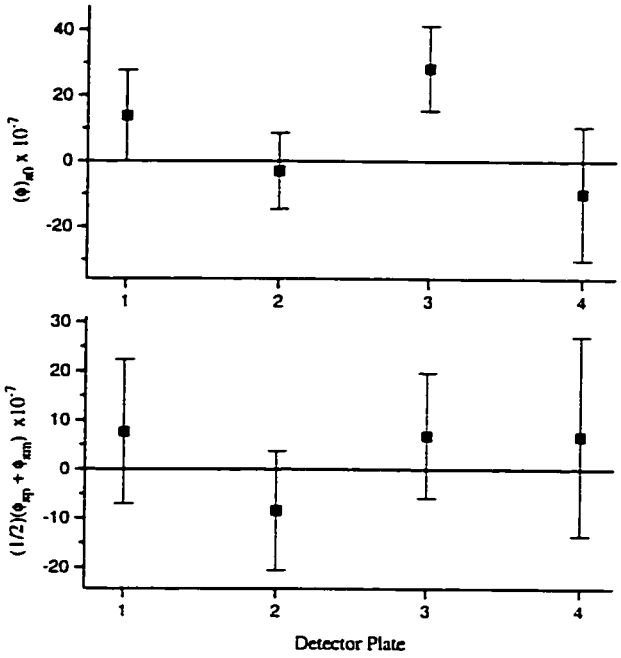

Figure 7.9: Average rotations as a function of neutron energy and detector region calculated using the up-down analysis scheme. The upper plot shows the rotations for the π-coil off case and the lower plot gives the average rotations for the π_p and π_m states.

for the π_0-state. In this analysis, the polarization product combinations were formed with the corresponding up-down channel pairs and averaged over target states as in the right-left analysis.

In the up-down analysis, the calculated expression for $\tilde{\phi}$ was a measure of the residual magnetic and field coil induced rotations in the up and down (verses right and left) parts of the apparatus. As before, the π_p-state and π_m-state results included the rotations from the π-coil leakage fields, and the π_0-state results do not.

We present in Figure 7.9 the results of the up-down analysis. In these calculations, the first 4 subcycles were removed from both the right and left side channel pairs. As a result, the statistical errors were larger than for the right-left analysis.

The upper plot presents the residual rotations for the π_0-state, and the lower plot presents the averaged π_p and π_m state residual rotations. The calculated overall residual rotation for the π-coil off case was $(7.2 \pm 7.9) \times 10^{-7}$ radians and for the π-coil on case was $(3.3 \pm 7.9) \times 10^{-7}$ radians, both consistent with zero.

The asymmetry data indicated the presence of gradients in the background rotations in both the right-left and up-down directions of the apparatus. These residual rotation results show that the differences in the fields and coil inhomogeneities in the right and left sides or the up and down halves when the two target state data are subtracted using the quadratic smoothing routine, were consistent with zero at the limit of our sensitivity, on the order of $(7 - 8) \times 10^{-7}$ radians.

7.6.4 Effects of scattering

Count-rate differences altering the total number of neutrons that reach the detector did not contribute directly to the measured rotation asymmetry, A, since both N_+ and N_- counts are equally affected. Recall that small angle scattering, which alters the path of the neutrons and therefore their rotation angle in the presence of a magnetic field, contributes to the measured rotation asymmetry. Target-dependent differences in this scattering contribute to the false PNC signal, φ_{PCtarg}. (Section 4.5.2) Since the amount of small angle neutron scattering was roughly proportional to the neutron scattering into angles greater than the detector acceptance angle, we used the front-back count-rate asymmetry to measure the presence of target-dependent scattering that led to changes in rotation angles.

We estimated the scattering contribution to the target-dependent PC rotation asymmetry as follows. We assumed the target-dependent difference in the number of detected neutrons was a measure of the number of neutrons whose trajectories depended upon the target helium position relative to the detector. We also estimated that the difference in magnetic rotation of these neutrons was comparable to the background asymmetry averaged over all records in these 22 data runs: -0.5 mrads

for the top channels and +0.4 mrads for the bottom channels. A conservative estimate for the average scattering contribution to the PNC signal was then the product of the count-rate asymmetry and the average background rotation, given by 0.2×10^{-7} in the upper and 0.6×10^{-7} in the lower halves of the detector.

A review of the data in Table 7.3 shows that the product, $A_{fb} \times \bar{A}$ was on the order of 6×10^{-7} or less for any given channel pair in the bottom half and an order of magnitude smaller in the top half. These contributions were less than the error for $\tilde{\phi}_{c,\pi}$ on the order of $(2-3) \times 10^{-6}$ for plates 1 through 3 and 4×10^{-6} on plate 4 where we detected fewer neutrons.

7.6.5 Summary of Systematic Analysis

We studied the effects of the data rejection criteria on the results. Including the records that had been eliminated by count-rate or by asymmetry differences in the analysis of the 22 data runs at 156 mA π-coil current, we obtained $\varphi_{\mathsf{PNC}} = (3.64 \pm 7.12) \times 10^{-7}$ radians which was not significantly different from the original result of $\varphi_{\mathsf{PNC}} = (3.55 \pm 7.23) \times 10^{-7}$ radians.

We combined the errors calculated from the polarization product systematic analysis (1×10^{-7}) and the magnetic field analysis (1.3×10^{-8}) to obtain an overall systematic error of

$$\sigma_{syst} = 1.0 \times 10^{-7} \tag{7.56}$$

We estimated the neutron count-rate in the detector as 2×10^6 neutrons/second. Adding the available counts from all the data runs used to calculate φ_{PNC}, we estimated the shot noise limit on the error as 6×10^{-7} radians.

We have shown that the analysis method extracts φ_{PNC} with an error that is close to the statistical limits of the data. The magnetic fields were subtracted with final residual rotations that were consistent with zero. The estimated contribution from target-dependent scattering effects were well below the statistical errors.

Chapter 8

DISCUSSION

We measured the parity non-conserving spin-rotation of cold neutrons through a 46 cm liquid helium target and obtained

$$\varphi_{\mathrm{PNC}}(\vec{n},\alpha) = (8.0 \pm 14(\mathrm{stat}) \pm 2.2(\mathrm{syst})) \times 10^{-7}\mathrm{radians/m} \qquad (8.1)$$

where the first error is statistical and the second error is systematic. This is the most sensitive spin-rotation measurement to date.

8.1 Weak interaction meson exchange coefficients.

As presented in Section 3.3, the predicted spin-rotation of neutrons transmitted through a liquid helium target, expressed in terms of the meson exchange coefficients is: [DFST83]

$$\varphi_{\mathrm{PNC}}(\vec{n},\alpha)[\mathrm{rads/m}] = -0.97 f_\pi - 0.32 h_\rho^0 + 0.11 h_\rho^1 - 0.22(h_\omega^0 - h_\omega^1) \qquad (8.2)$$

We combined the results for the $\vec{n}+\alpha$ system with results in the isospin analog system, $\vec{p}+\alpha$, and obtained an expression for f_π that depends only weakly on the remaining coupling constants. The longitudinal analyzing power of polarized protons on a helium target in terms of the meson exchange coefficients is given by: [LMM+86]

$$A_{\mathrm{L}}(\vec{p},\alpha) = -0.34 f_\pi + 0.14 h_\rho^0 + 0.05 h_\rho^1 + 0.06(h_\omega^0 + h_\omega^1) \qquad (8.3)$$

Combining Equations 8.2 and 8.3, we find

$$f_\pi = -[0.51\varphi_{\mathrm{PNC}}(\vec{n},\alpha) + 1.47 A_{\mathrm{L}}(\vec{p},\alpha)] + 0.04 h_\rho^0 + 0.13 h_\rho^1 - 0.03 h_\omega^0 + 0.21 h_\omega^1 \qquad (8.4)$$

We substituted our results for φ_{PNC} given in Equation 8.1, the measured analyzing power, $A_L(\vec{p},\alpha) = -(3.3 \pm 0.9) \times 10^{-7}$, [LMM+86] and the DDH "best values" for the coupling coefficients, $h_\rho{}^0$, $h_\rho{}^1$, $h_\omega{}^0$, $h_\omega{}^1$ (Table 2.2) to obtain,

$$f_\pi = (-1.75 \pm 10.5) \times 10^{-7} \tag{8.5}$$

For one standard deviation, we predict the acceptable range to be

$$-34 < f_\pi < 23 \qquad \text{(units of } 3.8 \times 10^{-8}\text{)} \tag{8.6}$$

From Table 2.2, the theoretical range is $0 < f_\pi < 30$ in units of the sum rule value 3.8×10^{-8}.

We have successfully extracted information on f_π from our measurement of the neutron spin-rotation in a liquid helium target. Our calculated range for the weak isovector coupling constant is consistent with the theoretical predictions of Desplanques, Donoghue, and Holstein.

Figure 8.1 is a revised plot of Figure 2.2 that includes our results. The upper boundary is shown with arrows indicating the included range and the lower boundary for f_π is off-scale. The large error band makes our number consistent with both the large and small predictions for f_π.

8.2 *n+^{4}He spin-rotation experiment: The next generation*

This measurement of the neutron spin-rotation in liquid helium was limited by statistical errors. We achieved a sensitivity to φ_{PNC} on the order of 5×10^{-5} for a single run of about 60 target cycles. To achieve the original goal of a 1×10^{-7} measurement error, we must acquire more statistics and improve the efficiency of the apparatus. The apparatus can be improved in the following ways to increase the rate of data accumulation for the next run.

- Increase the available beam. Recent improvements on the NG-6 beam line at NIST have increased the beam throughput in the area of the cryo-filters. New

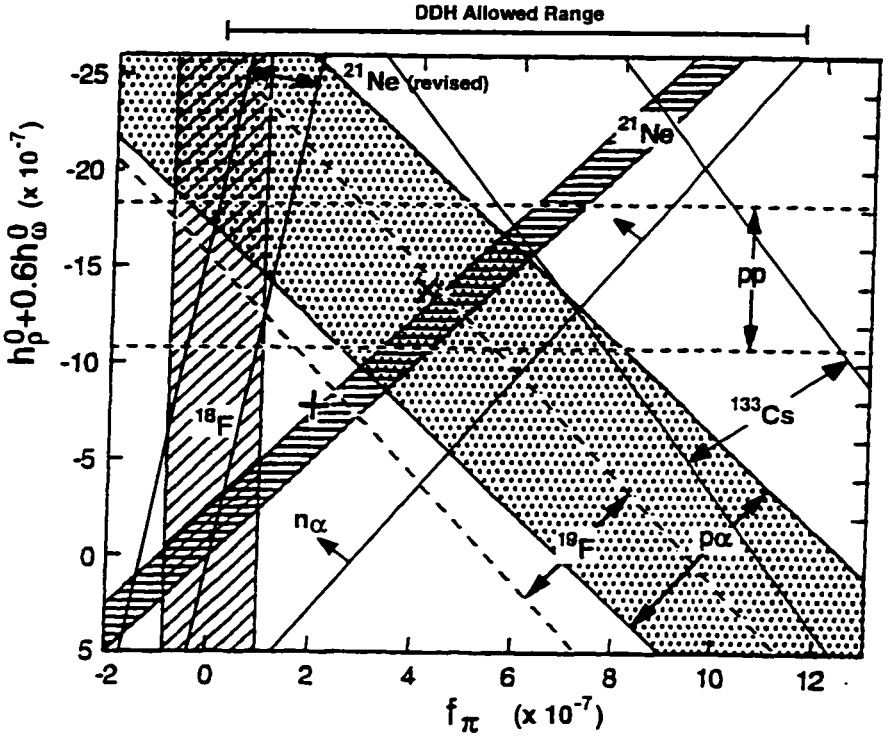

Figure 8.1: Revised plot of the constraints on the isoscalar and isovector couplings that includes the results of this $n + \alpha$ spin-rotation measurement.

measurements indicate the γ radiation is acceptable with fewer Bismuth filters. Our results indicate the experiment can tolerate more shorter wavelength neutrons so that fewer Beryllium filters could also be used. During NG-6 beam line tests following our experiment, the NIST scientists discovered a damaged Beryllium filter that caused the downward deflection of the beam. These changes in beam profile would harden the spectrum and lower the divergence of the beam entering the polarizer, increasing the transmission through the supermirror.

- Improve transmission through the apparatus. Open up the collimators to accept more neutrons in the horizontal direction (2.3 cm x 4.2 cm). Make the 8 foot flight tube and input coil tube one long piece to reduce losses and increase the initial acceptance of neutrons exiting the supermirror.

- Shorten the dead time of data acquisition by reducing the drain time. The helium flow out of the targets can be increased by opening the target drain-holes, removing obstructions of the draining pathway in the target (for instance from the target collimators) and opening the target vent holes.

- Improve the cryostat fill stack joints and the insert feed through joints. These improvements will eliminate the downtime from repairs and vacuum accidents. Repairing the helium stack will improve the stability of pumping on the helium can to reduce the temperature of the insert. Increase the hold time for the cryostat to lengthen the data runs, and to reduce the downtime from helium transfers.

Indications are that the systematic contributions to a false PNC signal are small. We are statistically limited in our sensitivity to these false contributions, and in our ability to determine the size of the systematic errors. A new measurement at the level of 1×10^{-7} may be sensitive to these systematics. The primary systematic

that will need to be reduced for a 10^{-7} sensitivity or better is to improve the target dependent scattering and achieve a front-back count-rate asymmetry below 10^{-5}. The systematics could be improved with the following changes:

- Put holes in the bottom of the target collimator holders to allow liquid helium to drain completely.

- Reduce the operating temperature of the target region. Lowering the temperature of the liquid helium in the cryostat and improving the thermal link between the insert and the cryostat would lower the running temperature, and reduce the background scattering in the helium. An improved thermal link would also increase the temperature stability in the insert, reducing this contribution to the slow drift of background asymmetries, and to pressure induced fluctuations in the transmission. With improved helium stack joints, and a larger pumping capacity, it may be possible to lower the temperature of the cryostat helium to less than 3 K. Eliminating the insert can would put the target helium reservoir in direct contact with the cryostat liquid helium can inner cylindrical wall. This would enable the target helium to equilibrate at a temperature close to that of the cryostat.

- The π-coil should be checked for small residual transverse magnetic fields that may have caused the tipping of the vertical fields. If the solenoid coils are to be rebuilt, the spacing between the wires should be reduced to decrease the fraction of neutrons that feel the edge fields from the wires.

- Add an independent beam flux monitor to normalize the polarization product calibration data, reducing the sensitivity to reactor fluctuations.

Improvements at the NG-6 end-station should increase the beam by about a factor of 1.5. Opening the collimators and extending the front guide tube will provide

an additional factor of about 2.3 increase in beam. The lower target temperatures will increase the transmission by about 20%. Increasing the efficiency of filling and draining the targets, introducing automatic filling of the cryogens, and eliminating downtime from vacuum accidents should increase the available data rate by a factor of about 5. These improvements, should give a sensitivity of about 6×10^{-7} radians per day, compared to the current experiment which achieved a sensitivity of 2.6×10^{-6} radians per day of data accumulation.

Figure 8.2 is the f_π *vs.* isoscalar couplings plot showing an error band that would be produced by a spin-rotation measurement of zero with a sensitivity of $\pm 10^{-7}$ radians. With this sensitivity, a neutron spin-rotation measurement in liquid helium would provide an important constraint on f_π.

8.3 n+H spin-rotation experiment: The next step

The two nucleon system is the most fundamental system in which to study the nucleon-nucleon weak interaction. The spin-rotation observable in the $n + p$ system has contributions from both the isovector and isoscalar couplings, but is dominated by f_π which enters with a coefficient that is greater than the others by a factor of 14.

The predicted neutron spin-rotation observable in a parahydrogen target is larger than that for the helium target. However, the scattering in the parahydrogen target is also larger, which increases the neutron scattering background and decreases the count-rate. A 15 cm long target (approximately 1.5 absorption lengths), would produce a measurable signal with a reasonable neutron count-rate. The neutron-proton spin-rotation observable is predicted to be in the range of $(0 - 1.35) \times 10^{-7}$ radians for a 15 cm parahydrogen target [AG84]. A sensitivity less than 5×10^{-8} is needed to resolve the different predictions for f_π: 1.35×10^{-7} radians for a large value of f_π and $0.97 \cdot 10^{-7}$ radians for f_π around zero. An improved $\varphi_{\mathrm{PNC}}(\vec{n} + \alpha)$ result will indicate the feasibility of using the current spin-rotation apparatus (modified to accommodate

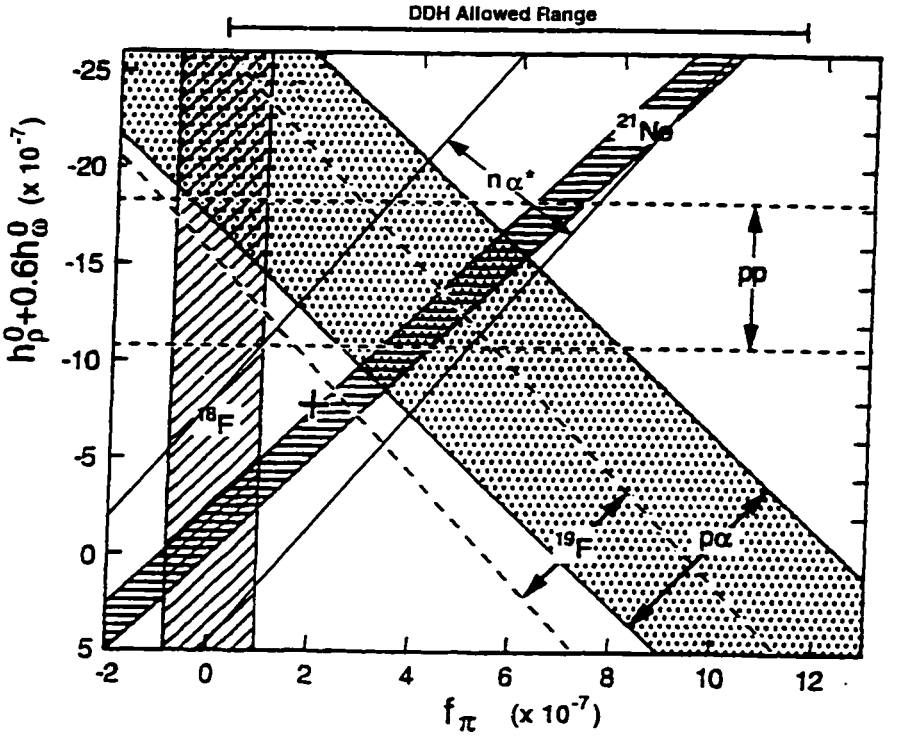

Figure 8.2: Predicted constraints on f_π and h_ρ^0 for the next $\vec{n}+\alpha$ measurement. The error band is shown for a zero spin-rotation measurement with a predicted sensitivity of $\pm 10^{-7}$ radians.

the parahydrogen target) to reach a sensitivity below 5×10^{-8} radians in the $n + p$ system.

The success of these neutron spin-rotation experiments will produce results that will greatly improve the limits on f_π. In addition, an improved apparatus to measure the gamma-ray asymmetry, A_γ, in the reaction $n + p \rightarrow d + \gamma$ is currently under construction [WBP+97], [BGH+97]. This observable is sensitive only to the isovector couplings, specifically, f_π, with contributions from other couplings ($h_\rho{}^1$ and $h_\omega{}^1$) that is smaller by 2 orders of magnitude. The spin-rotation and gamma-ray asymmetry measurements in the $n+p$ system will provide complementary results because of their different dependences on the coupling constants. With the successful completion of these measurements to the necessary sensitivities, we will be able to quantify the strength of the neutral current contribution to the weak nucleon-nucleon interaction.

BIBLIOGRAPHY

[AG84] Y. Avishai and P. Grange. Parity violation in threshold neutron-proton scattering. *J. Phys. G: Nucl. Phys.*, 10:L263–70, 1984.

[AH85] E.G. Adelberger and W.C. Haxton. Parity violation in the nucleon-nucleon interaction. *Ann.Rev.Nucl.Part.Sci*, 35:501–558, 1985.

[Avi82] Y. Avishai. Parity non-conserving n-α elastic scattering: Estimates of observables. *Physics Letters*, 112B(4,5):311–4, 1982.

[Bar61] G. Barton. Notes on the static parity non-conserving interaction potential. *Il Nuovo Cimento*, 19(3):512, 1961.

[BBC95] Burr-Brown IC Data Book (Linear Products), 1995.

[BGH+97] J. D. Bowman, G. L. Greene, G. E. Hogan, J. N. Knudson, S. K. Lamoreaux, , G. L. Morgan, C. L. Morris, S. I. Pentilla, D. A. Smith, W. S. Wilburn, V. W. Yuan, et al. Measurement of the parity-violating gamma asymmetry A_γ in the capture of polarized cold neutrons by para-hydrogen, $\vec{n} + p \rightarrow d + \gamma$. Technical report, Los Alamos National Laboratory; Proposal, 1997.

[BGJM93] J. D. Bowman, G. T. Garvey, M. B. Johnson, and G. E. Mitchell. Recent advances in the study of parity violation in the compound nucleus. *Annual Reviews of Nuclear and Particle Science*, 43:829–881, 1993.

[CB83] E.D. Commins and P.H. Bucksbaum. *Weak Interactions of leptons and quarks*. Cambridge University Press, 1983.

[DDH80] B. Desplanques, J. F. Donoghue, and B. R. Holstein. Unified treatment of the parity violating nuclear force. *Annals of Physics*, 124(2):449–95, 1980.

[de 84] L. A. de Graaf. Filters for neutron beams. Technical report, Interuniversitair Reactor Instituut, February 1984.

[Des97] Bertrand Desplanques. Parity violation in hadronic systems. In *Bulletin of the American Physical Society*, volume 42, October 1997.

[Des98] Bertrand Desplanques. Parity non-conservationn in nuclear forces at low energy: Phenomenology and questions. *Physics Reports*, 1998. To be published.

[DFST83] V. F. Dmitriev, V. V. Flambaum, O. P. Sushkov, and V. B. Telitsin. The parity violating rotation of the neutron spin in helium. *Physics Letters B*, 125B(1):1–4, 1983.

[DZ86] V. M. Dubovik and S. V. Zenkin. Formation of parity-nonconserving nuclear forces in the standard model $SU(2)_L$ * U(1) * $SU(3)_c$. *Annals of Physics*, 172(1):100–35, 1986.

[EL57] P. A. Egelstaff and H. London. The scattering of cold neutrons by liquid helium. *Proceedings of the Royal Society*, A242:347, 1957.

[FCDH91] G. B. Feldman, G. A. Crawford, J. Dubach, and B. R. Holstein. Delta contributions to the parity-violating nuclear interaction. *Physical Review C (Nuclear Physics)*, 43(2):863–74, 1991.

[FHR+80] M. Forte, B.R. Heckel, N.F. Ramsey, K. Green, G.L. Greene, J. Byrne, and J.M. Pendlebury. First measurement of parity-nonconserving

neutron-spin rotation: the tin isotopes. *Physical Review Letters*, 45(26):2088–92, 1980.

[FLS63] Richard P. Feynman, Robert B. Leighton, and Mathew Sands. *The Feynman Lectures on Physics*, chapter 6, page 6:14. Addison-Wesley Publishing Company, 1963.

[FM97] V. V. Flambaum and D. W. Murray. Anapole moment and nucleon weak interactions. *Physical Review C (Nuclear Physics)*, 56(3):1641–4, 1997.

[Gol80] H. Goldstein. *Classical Mechanics*, pages 588–596. Addison Wesley Publishing Co., 2nd edition, 1980.

[GS56] L. Goldstein and H. S. Sommers Jr. Transmission of slow neutrons by liquid helium-4, II. *Physical Review*, 101(4):1235–42, Feb 1956.

[GW64] M. L. Goldberger and K. M. Watson. *Collision Theory.* John Wiley, 1964.

[Hax97] W. C. Haxton. Atomic parity violation and the nuclear anapole moment. *Science*, 275:1753–4, March 1997.

[HB95] M. Horoi and B. A. Brown. Toward a consistent description of parity nonconservation in a=18-21 nuclei. *Physical Review Letters*, 74(2):231–4, 1995.

[Hec81] Blayne R. Heckel. *Parity Non-Conserving Neutron Spin Rotation: The Tin Isotopes.* PhD thesis, Harvard University, 1981.

[HFR+84] B. Heckel, M. Forte, N. F. Ramsey, G. L. Greene, K. Green, J. Byrne, and J. M. Pendlebury. Parity non-conserving neutron spin rotation. volume 45, pages 89–92, 1984.

[HFS+84] B. Heckel, M. Forte, O. Schaerpf, K. Green, G. L. Greene, N. F. Ramsey, J. Byrne, and J. M. Pendlebury. Measurement of parity nonconserving neutron spin rotation in lanthanum. *Physical Review C (Nuclear Physics)*, 29(6):2389–91, 1984.

[HH95] Wick C. Haxton and Ernest M. Henly. *Symmetries and Fundamental Interactions in Nuclei*, chapter 2, pages 17–66. World Scientific, 1995.

[Hol89] Barry R. Holstein. *Weak Interactions in Nuclei.* Princeton University Press, 1989.

[HPW78] J. B. Hayter, J. Penfold, and W. G. Williams. Compact polarising Soller guides for cold neutrons. *Journal of Physics E; Scientific Instruments*, 11:454–8, 1978.

[HRG+82] B. Heckel, N. F. Ramsey, K. Green, G. L. Greene, R. Gahler, O. Schaerpf, M. Forte, W. Dress, P. D. Miller, R. Golub, and J. Byrne. A measurement of parity non-conserving neutron spin rotation in lead and tin. *Physics Letters B*, 119B(4-6):298–302, 1982.

[Hug54] D. J. Hughes. *Neutron Optics.* Interscience Publishers, Inc., 1954.

[KLL+87] S. Kistryn, J. Lang, J. Liechti, Th. Maier, F. Muller, Tedaldi. F. Nessi, M. Simonius, J. Smyrski, S. Jaccard, W. Haeberli, and J. Sromicki. Precision measurement of parity nonconservation in proton- proton scattering at 45 mev. *Physical Review Letters*, 58(16):1616–19, 1987.

[KS77a] L. Koester and A. Styerl. *Neutron Physics*, chapter 1, page 36. Springer Verlag, 1977.

[KS77b] L. Koester and A. Styerl. *Neutron Physics*, chapter 1, page 36. Springer Verlag, 1977.

[L+67] V. M. Lobashov et al. Parity violation in ^{181}Ta. *Physics Letters B*, 25, 1967.

[LMM+86] J. Lang, Th. Maier, R. Muller, Tedaldi. F. Nessi, Th. Roser, M. Simonius, J. Sromicki, and W. Haeberli. Parity nonconservation in elastic p alpha scattering. *Physical Review C (Nuclear Physics)*, 34(5):1545–58, 1986.

[LY56] T. D. Lee and C. N. Yang. Question of parity conservation in weak interactions. *Physical Review*, 104(1):254–8, Oct 1956.

[Mic64] F. Curtis Michel. Parity nonconservation in nuclei. *Physical Review*, 133(2B):B329–49, January 1964.

[Oxf] Oxford Instruments, Inc. *Operator's Handbook for Horizontal Cold Bore Cryostat: (Project Number 37409.4).*

[Pag97] Shelley A. Page. The TRIUMF parity violation experiment. In *Bulletin of the American Physical Society*, volume 42, October 1997.

[RGL91] David J. Richardson Robert Golub and Steve K. Lamoreaux. *Ultra-cold Neutrons.* Adam Hilger, 1991.

[Sch89] O. Schaerpf. Properties of beam bender type neutron polarizers using supermirrors. volume 156-157, pages 639–46, 1989.

[Sco59] Russell B. Scott. *Cryogenic Engineering.* D. Van Nostrand Co., Inc., 1959.

[SDG55] H. S. Sommers Jr., J. G. Dash, and L. Goldstein. Transmission of slow neutrons by liquid helium. *Physical Review*, 97(4):855–62, Feb 1955.

[Sto74] L. Stodolsky. Neutron optics and weak currents. *Physics Letters*, 50B(3):352–6, June 1974.

[Sum79] Timothy J. Sumner. *Progress towards a new experiment to search for the electric dipole moment of the neutron using ultra-cold neutrons.* PhD thesis, University of Sussex, 1979.

[WAH+57] C. S. Wu, E. Ambler, R. W. Hayward, D. D. Hoppes, and R. P. Hudson. Experimental test of parity violation in beta decay. *Physical Review*, 105:1413, 1957.

[WBC+97] C. S. Wood, S. C. Bennett, D. Cho, B. P. Masterson, J. L. Roberts, C. E. Tanner, and C.E. Wieman. Measurement of parity nonconservation and an anapole moment in cesium. *Science*, 275:1759–63, March 1997.

[WBP+97] W. S. Wilburn, J. D. Bowman, S. I. Pentilla, V. Yuan, M. B. Leuschner, V. R. Pomeroy, D. R. Rich, and W. M. Snow. Low-noise photocathode preamplifiers for measuring a_γ in $\vec{n} + p \rightarrow d + \gamma$. In *Bulletin of the American Physical Society*, volume 42, October 1997.

[Wie96] Fred E. Wietfeldt. Study of expected beamline flux for the emit experiment. Private communication., 1996.

[WN96] Fred E. Wietfeldt and Jeff S. Nico. NIST, Gaithersburg, May 1996. Private communication.

Appendix A

INPUT/OUTPUT COIL DESIGN CRITERIA

The hamiltonian describing the interaction of the neutron spin in a magnetic field is given by

$$\mathcal{H}_{\text{mag}} = -\vec{\mu}_n \cdot \vec{B} = -\left(\frac{\gamma_n \hbar}{2}\right) \vec{\sigma} \cdot \vec{B} \tag{A.1}$$

where $\vec{\mu}_n$ is the magnetic moment of the neutron and $\vec{B}$ is the applied field. The resulting (Larmor) precession frequency of the neutron spin about the applied field is then

$$\omega_L = \gamma_n |\vec{B}| \tag{A.2}$$

The proportionality factor γ_n, is the gyromagnetic ratio for neutrons given by

$$\gamma_n = -3.8\left(\frac{e}{2Mc}\right) = -3.8\frac{\mu_n}{\hbar} \tag{A.3}$$

where e is the basic quantum of charge, M is the neutron mass, and c is the speed of light.

The adiabatic condition for spin precession is satisfied when the fractional rate of change of the magnetic field is very much less than the Larmor frequency.

$$\frac{1}{|\vec{\mathrm{B}}|}\left|\frac{d\vec{\mathrm{B}}}{dt}\right| \ll \omega_L \tag{A.4}$$

If the field changes faster than the spin can follow, then the spin will in time no longer be aligned with the field.

For a neutron traveling in the $\hat{z}$ direction with a velocity v, for a time t, the fractional change in time is given by $dt = \frac{1}{v}dz$. We define β as the fractional change

in the magnetic field B, and rewrite Equation A.4 as a ratio comparison of the rate of change of the magnetic field to the Larmor precession frequency.

$$r = \frac{(\frac{dB}{dz})v}{\gamma_n B} \tag{A.5}$$

Note that a field change in the beam direction will induce a transverse change in the magnetic field, producing a tip angle with respect to the xy-plane. In a source free region, $\vec{\nabla} \times \vec{B} = 0$, so that a change in the magnitude of the spin direction magnetic field along the beam direction ($\frac{dB_z}{dz}$) will create a nonzero component of B in the beam direction ($\frac{dB_z}{dx}$). This is the case for the decreasing field in the $\hat{y}$ direction and the increasing field in the $\hat{x}$ direction in the output coil. The transverse field must change slowly in the beam direction to minimize the created tip field.

The beam depolarization factor, D, is determined from the angle that the spin lags the field which is given by the ratio, r, in Equation A.5. For small angles, we have

$$D = 1 - \cos r = \frac{r^2}{2} \qquad \text{where} \qquad r = \frac{\omega}{\omega_L} = \frac{(\frac{dB}{dz})v}{\gamma_n B} \tag{A.6}$$

The output adiabatic coil was designed to maintain a depolarization condition of $D < 10^{-4}$. The field inhomogeneities in the input coil, especially in the transition from the guide coil to the input coil were also designed to satisfy this depolarization condition.

Appendix B

DATA

We present in Table B.1 the asymmetries from the two large uniform field systematic test runs, and in Table B.2, the asymmetries from the two gradient field test runs.

A ratio of the values in the plate differences column (P1-P4) in Table B.1 for the front and back rotations implies that the applied uniform magnetic field in the front was a factor of 0.45 smaller than the field in the back half of the apparatus. The same information from Table B.2 shows that the fields in the front and back were nearly the same (the back field was 80% smaller) and opposite in sign as expected. Note that the similar information from the plates 1 and 3 difference column are in agreement.

Using Equation 7.42 for two plate differences, we separated the magnetic field and the spin factor. Taking the ratio of the entries in the two plate difference columns of Tables B.1 and B.2 for the same region of the apparatus (front or back) provided information on the velocity distribution of the detector plates. We have

$$\frac{\gamma_1 - \gamma_4}{\gamma_1 - \gamma_3} \approx 1.7 \tag{B.1}$$

which agrees fairly well using the velocities (listed in Table 5.2) calculated from a fit of a Maxwell Boltzmann spectrum to the measured detector count-rates.

Table B.1: Uniform field systematic data. The plate asymmetries were calculated from the average over each quadrant asymmetry. The entries in the last two columns are the difference of the entries for Plates 1 and 3, and for Plates 1 and 4, respectively. All rotations are given in milliradians.

Positive Uniform Field Data (Run 597)						
Asymmetry	Plate 1	Plate 2	Plate 3	Plate 4	P1-P3	P1-P4
A_p	0.68	-0.53	-1.98	-3.24	2.66	3.92
A_0	3.63	1.05	-2.44	-6.37	6.07	10.01
A_m	-0.39	-1.64	-3.11	-4.35	2.72	3.96
ΣA	0.14	-1.08	2.55	-3.79	2.69	3.94
ΔA	0.54	0.55	0.56	0.56	-0.03	-0.02
$\frac{A_0-\Sigma A}{\mathcal{P}_0+\mathcal{P}_\pi}$	2.56	1.50	0.07	-1.68	2.49	4.24
$\frac{A_0(\frac{\mathcal{P}_\pi}{\mathcal{P}_0})+\Sigma A}{\mathcal{P}_0+\mathcal{P}_\pi}$	2.21	-0.16	-3.07	-5.97	5.27	8.18

Negative Uniform Field Data (Run 594)						
Asymmetry	Plate 1	Plate 2	Plate 3	Plate 4	P1-P3	P1-P4
A_p	-2.10	0.19	3.10	6.06	-5.19	-8.16
A_0	-6.19	-1.78	4.54	12.20	-10.73	-18.39
A_m	-3.27	-1.03	1.84	4.76	-5.11	-8.04
ΣA	-2.68	-0.42	2.47	5.41	-5.15	-8.10
ΔA	0.59	0.61	0.63	0.65	-0.04	-0.06
$\frac{A_0-\Sigma A}{\mathcal{P}_0+\mathcal{P}_\pi}$	-2.57	-0.95	1.39	4.42	-3.96	-6.99
$\frac{A_0(\frac{\mathcal{P}_\pi}{\mathcal{P}_0})+\Sigma A}{\mathcal{P}_0+\mathcal{P}_\pi}$	-5.55	-1.31	4.19	10.22	-9.74	-15.77

Table B.2: Gradient field systematic data. The plate asymmetries were calculated from the average over each quadrant asymmetry. The rotations are given in milliradians.

Positive Gradient Field Data (Run 603)						
Asymmetry	Plate 1	Plate 2	Plate 3	Plate 4	P1-P3	P1-P4
A_p	-0.65	-0.37	0.12	1.02	-0.77	-1.67
A_0	0.57	0.28	0.02	-0.12	0.55	0.67
A_m	-1.69	-1.47	-1.02	-0.20	-0.67	-1.49
ΣA	-1.17	-0.92	-0.45	0.41	-0.72	-1.58
ΔA	0.52	0.55	0.57	0.61	-0.05	-0.09
$\frac{A_0-\Sigma A}{\mathcal{P}_0+\mathcal{P}_\pi}$	1.28	0.84	0.31	-0.34	0.96	1.62
$\frac{A_0(\frac{\mathcal{P}_\pi}{\mathcal{P}_0})+\Sigma A}{\mathcal{P}_0+\mathcal{P}_\pi}$	-0.53	-0.48	-0.29	0.20	-0.24	-0.74

Negative Gradient Field Data (Run 600)						
Asymmetry	Plate 1	Plate 2	Plate 3	Plate 4	P1-P3	P1-P4
A_p	0.60	0.16	-0.55	-1.43	1.15	2.03
A_0	-0.66	-0.87	-1.05	-1.04	0.39	0.38
A_m	-0.46	-0.94	-1.64	-2.42	1.18	1.96
ΣA	0.07	-0.39	-1.10	-1.92	1.17	2.00
ΔA	0.53	0.55	0.54	0.50	-0.02	0.03
$\frac{A_0-\Sigma A}{\mathcal{P}_0+\mathcal{P}_\pi}$	-0.53	-0.34	0.03	0.58	-0.56	-1.11
$\frac{A_0(\frac{\mathcal{P}_\pi}{\mathcal{P}_0})+\Sigma A}{\mathcal{P}_0+\mathcal{P}_\pi}$	-0.33	-0.77	-1.32	-1.82	0.99	1.50

Table B.3: Asymmetries from normal data runs. The plate asymmetries were calculated from the average over each quadrant asymmetry. The rotations are given in milliradians.

Normal Data (22 Runs at 156 mA)						
Asymmetry	Plate 1	Plate 2	Plate 3	Plate 4	P1-P3	P1-P4
A_p	0.45	0.52	0.66	0.92	-0.21	-0.47
A_0	-0.82	-0.97	-1.04	-0.94	0.22	0.12
A_m	-0.64	-0.59	-0.48	-0.24	-0.16	-0.40
$\Sigma A_\pm$	-0.10	-0.04	0.09	0.34	-0.18	-0.44
$\Delta A_\pm$	0.54	0.56	0.57	0.58	-0.03	-0.03
$\frac{A_0-\Sigma A}{\mathcal{P}_0+\mathcal{P}_\pi}$	-0.53	-0.65	-0.75	-0.84	0.22	0.30
$\frac{A_0(\frac{\mathcal{P}_\pi}{\mathcal{P}_0})+\Sigma A}{\mathcal{P}_0+\mathcal{P}_\pi}$	-0.55	-0.58	-0.53	-0.29	-0.02	-0.25

Table B.4: Magnetic field systematic contributions to φ_{PCtarg}. The table gives the values calculated for φ_{PNC} in the specified systematic runs. These data were used to give the multiplicative entires in Table 7.9.

Run	φ_{PNC} All Channels ($\times 10^{-7}$)			
Data	π_p-state	π_m-state	$\pi_\pm$-state	π_0-state
597	-0.35 ± 55.74	16.37 ± 46.40	8.01 ± 38.38	-10.45 ± 41.80
594	65.35 ± 54.60	-24.21 ± 75.71	20.57 ± 44.90	2.16 ± 43.96
597-594	-65.70 ± 78.03	40.56 ± 88.80	-12.56 ± 59.07	12.61 ± 60.66
603	35.05 ± 96.04	18.23 ± 73.94	26.64 ± 54.89	79.12 ± 61.62
600	55.82 ± 87.15	119.2 ± 71.26	87.52 ± 62.87	61.54 ± 64.24
603-600	-20.77 ± 88.90	-101.0 ± 102.7	-60.88 ± 83.46	17.58 ± 61.62

VITA

Diane Melanie Markoff was born in 1962 to parents Albert and Irene Markoff in Los Angeles, California. She studied Nuclear Engineering, Physics and Mathematics at the University of California, Berkeley, where in 1983 earned a B.S. degree in Engineering Physics and a B.A. degree in Applied Mathematics. In 1986, she was awarded an M.S. degree in Nuclear Engineering for the completion of coursework and a masters thesis under the direction of Professor Stan Prussin and project supervisor Alex DeVolpi at the Argonne National Laboratory. She began the physics PhD. program in 1987 at the University of Washington, Seattle. In addition to physics, she enjoyed with friends the beautiful natural surroundings of the Pacific Northwest on whitewater rivers, hiking trails, alpine ski slopes, backcountry ski trails, mountain biking paths and ocean water of Puget Sound. She has accepted a post-doctoral position with the North Carolina State University Polarized Target Group at the Triangle Universities Nuclear Laboratory (TUNL) located on the Duke University campus in Durham, North Carolina.

IMAGE EVALUATION TEST TARGET (QA-3)

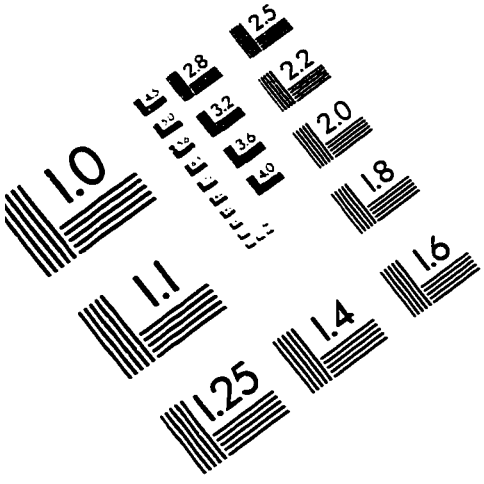

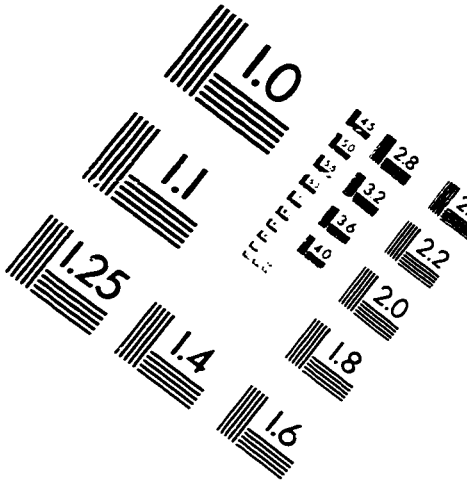

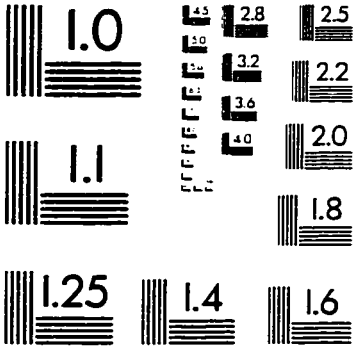

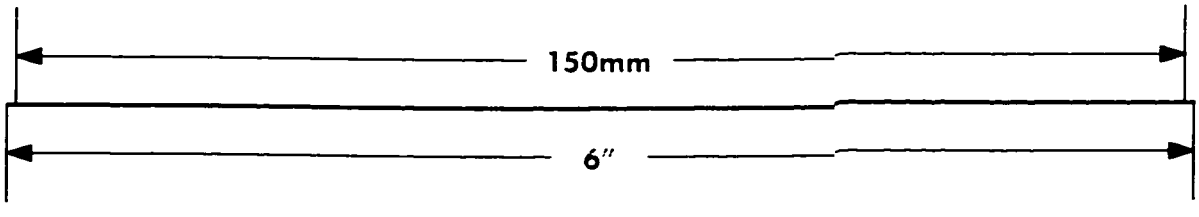

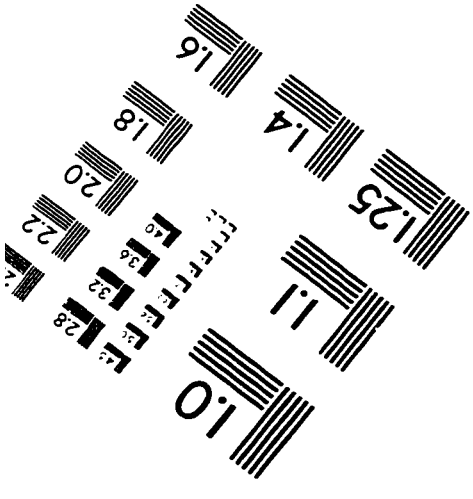

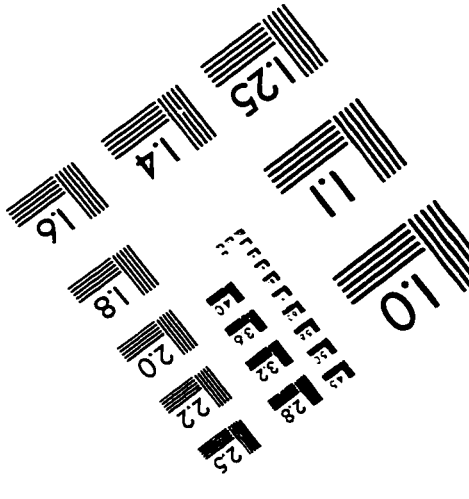

APPLIED IMAGE, Inc
1653 East Main Street
Rochester, NY 14609 USA
Phone: 716/482-0300
Fax: 716/288-5989